

**Chemical Functionalization and Electronic Passivation of  
Gallium Arsenide Surfaces**

Thesis by

Matthew C. Traub

In Partial Fulfillment of the Requirements

for the Degree of

Doctor of Philosophy

California Institute of Technology

Pasadena, California

2008

(Defended July 10, 2007)

© 2008

Matthew Traub

All Rights Reserved

## Acknowledgements

I am grateful for the time I have spent at Caltech. Trying to acknowledge all of the friends, colleagues and scholars who have made my time here so meaningful is probably a futile task, but I will do my best.

I feel privileged to have worked under the tutelage of Professor Nathan S. Lewis. Nate has allowed me to develop an independent approach to scientific inquiry, while at the same time imparting the rigorousness and attention to detail that he always brings to his work. Further, I appreciate learning not just science but policy, and how to engage with some of societal problems while still performing fundamental science. I am grateful for all of his support during the time I spent in Lewis group.

Similarly, I am constantly thankful for the opportunity to work with Dr. Bruce Brunschwig. Bruce's support was critical to virtually all of the work discussed in this dissertation. He was a constant source of advice on everything from vacuum-system repair to the arcane details of Marcus theory. Having him around was like having a second advisor, without any of the attendant addition paperwork. I would also like to thank the other members of my committee, Professors Harry Gray, Doug Rees, and Harry Atwater, for their invaluable advice.

Among my fellow grad students at Caltech, I want to begin by acknowledging Lauren Webb, David Michalak, and Julie Biteen. Despite the fact that none of them were working on GaAs, they all spent time at Brookhaven National Lab helping me make soft X-ray measurements. Additionally, Julie was a fantastic collaborator for the laser experiments on nanocrystals. I am also grateful for the time I was able to spend working with Florian Gstrein and Dr. Hidehiro Yoshida. The experiments I performed with them

were ultimately not included in this work, but they were enormously beneficial to my growth as a scientist. David Knapp and David Gleason-Rohrer have been great colleagues for XPS duties. More recently, I have had the opportunity to perform photoelectrochemistry experiments with Jim Maiolo. In addition to the people listed above, I have received advice on my science and my writings from Pat Hurley, Jae-Joon Lee, Stephen Maldonado, Kimberly Marshall Papadantonakis, and Kate Plass, and at some point or another, nearly everyone who has been a member of the Lewis group during my time here. Finally, the importance of the organization and support provided by Sherry Feick and Nannette Pettis during my time in the Lewis group cannot be overstated.

I am grateful for the support and love of my parents, Roger and Stephanie, and my brother Garrett, along with that of the O'Meara family. I only wish that Robert and Renee Traub were still here to see this work completed. I have been lucky to have friends at Caltech, across Los Angeles and elsewhere, who have made my life more interesting and exciting in a wide variety of ways. And finally, any remaining sanity that I have retained during grad school is directly attributable to my wife Caroline, with whom I am incredibly lucky to share my life. Thank you all.

## Abstract

Chemically controlled, low defect-density surfaces are essential for the incorporation of gallium arsenide into solar conversion and optoelectronic devices. Detailed X-ray photoelectron spectroscopic (XPS) studies have been conducted on chemically functionalized GaAs(111)A surfaces. Quantitative analysis of this surface after HCl(aq) etching reveals that it is completely free of observable oxide and As<sup>0</sup> contaminants, and is terminated with nearly a full monolayer of Cl. These surface Ga-Cl bonds have been reacted with the phosphine reagents PCl<sub>3</sub> and PEt<sub>3</sub>, both of which introduce P atoms onto the surface. Direct reaction of PCl<sub>3</sub> with the oxide-terminated surface leads to surfaces that are nearly oxide free but contain measurable amounts of As<sup>0</sup>. Steady-state photoluminescence (PL) intensity measurements were used to evaluate the effectiveness of these techniques at passivating surface carrier recombination. Consistent with the chemical observations, etched and functionalized surfaces showed enhanced PL, while surfaces functionalized directly with PCl<sub>3</sub> did not.

The effects of surface functionalization were explored on GaAs nanocrystals chemically synthesized with an oxide capping layer. Transmission electron microscopy and powder X-ray diffraction demonstrated that the particles were anisotropically etched by treatment with HCl(aq). XPS measurements showed that the Cl-terminated particles were almost entirely free of oxide but contained significant As<sup>0</sup> contamination. Further functionalization of the particles with N<sub>2</sub>H<sub>4</sub> or NaSH replaced surface Cl atoms with N or S moieties but did not remove this As<sup>0</sup>. The corresponding band gap PL of these particles was quite weak. Annealing the functionalized particles led to the disappearance of the As<sup>0</sup> and strong enhancement of the PL intensity. These results

imply that surface  $As^0$  is a dominant carrier trap on nanoscale GaAs surfaces and should be broadly applicable for improving the performance of GaAs nanocrystals and nanowires.

Finally, Fermi's golden rule has been used to develop relationships between rate constants for electron transfer in donor-bridge-acceptor and electrode-bridge-acceptor systems and resistances across metal-bridge-electrode and metal-bridge-tip junctions. This formulation was used to predict resistances for alkanethiolate, oligophenylene, and DNA bridges from reported donor-acceptor electron-transfer measurements in these systems. These predicted values were compared to reported resistances measured for these molecules.

# Contents

<b>Acknowledgements</b>	<b>iii</b>
<b>Abstract</b>	<b>v</b>
<b>List of Figures, Tables and Schemes</b>	<b>xi</b>
<b>Chapter 1: An Introduction to Gallium Arsenide Surface Chemistry</b>	<b>1</b>
1.1 Semiconductor Surface Chemistry and Charge Carrier Dynamics	1
1.2 Surface Passivation Techniques: Silicon vs. Gallium Arsenide	5
1.3 Chemical Passivation of GaAs Surfaces	7
1.4 New Strategies for GaAs Passivation	13
<b>References</b>	<b>17</b>
<b>Chapter 2: High-Resolution Photoelectron Spectroscopy of Chlorine-Terminated GaAs(111)A Surfaces</b>	<b>22</b>
2.1 Introduction—Analytical Chemistry of the GaAs Surface	22
2.2 Experimental	25
2.2.1 Materials and Methods	25
2.2.2 Instrumentation	25
2.2.2.1 XPS Measurements	25
2.2.2.2 SXPS Measurements	27
2.3 Results and Discussion	30

2.4 Conclusions	38
2.5 Acknowledgements	38
<b>References</b>	<b>40</b>
<b>Chapter 3: Phosphine Functionalization of GaAs(111)A</b>	<b>42</b>
3.1 Introduction	42
3.2 Experimental	46
3.2.1 Materials and Methods	46
3.2.2 Instrumentation	47
3.2.2.1 XPS Measurements	47
3.2.2.2 Photoluminescence Measurements	47
3.3 Results	47
3.3.1 Reactions of $\text{PEt}_3$ and $\text{PCl}_3$ on Cl-Terminated GaAs(111)A	47
3.3.2 Reactions of $\text{PCl}_3$ on Native Oxide-Terminated GaAs(111)A	59
3.3.3 Oxidation of Phosphine-Functionalized GaAs(111)A in Ambient Atmosphere	61
3.3.4 Steady-State Photoluminescence of Functionalized GaAs(111)A	64
3.4 Discussion	67
3.5 Conclusions	68
3.6 Acknowledgements	69

<b>References</b>	<b>70</b>
<b>Chapter 4: Chemical Functionalization and Passivation of Gallium Arsenide</b>	
<b>Nanocrystals</b>	<b>72</b>
4.1 Introduction—Surface Passivation and Semiconductor Nanocrystals	72
4.2 Experimental	74
4.2.1 Materials and Methods	74
4.2.2 Instrumentation	76
4.3 Results and Discussion	77
4.3.1 Characterization of Oxide-Coated GaAs Nanocrystals	77
4.3.1.1 X-ray Diffraction	77
4.3.1.2 X-ray Photoelectron Spectroscopy	78
4.3.1.3 Diffuse Reflectance IR Spectroscopy	80
4.3.2 Characterization of HCl(aq)-Etched GaAs Nanocrystals	80
4.3.2.1 X-ray Diffraction	80
4.3.2.2 Transmission Electron Microscopy	83
4.3.2.3 X-ray Photoelectron Spectroscopy	83
4.3.3 Chemical Functionalization of Cl-terminated GaAs Nanocrystals	89
4.3.3.1 Hydrazine-Treated Samples	89
4.3.3.2 NaSH-Treated Samples	92
4.3.3.3 Annealed Surfaces	95
4.3.4 Photoluminescence of Functionalized GaAs Nanocrystals	97
4.4 Conclusions	99
<b>References</b>	<b>101</b>

<b>Chapter 5: Relationships Between Nonadiabatic Bridged Intramolecular, Electrochemical, and Electrical Electron Transfer Processes</b>	<b>104</b>
5.1 Introduction	104
5.2 Theoretical Approach	105
5.2.1 General Rate Expressions	105
5.2.2 Intramolecular Donor-Bridge-Acceptor Electron Transfer	111
5.2.3 Metal Electrode-Bridge-Molecular Acceptor Electron Transfer	112
5.2.4 Metal Electrode-Bridge-Metal Electrode Electron Transfer	118
5.2.5 Electron Transfer Between a STM Tip and a Molecularly Coated Metal Electrode	120
5.2.6 Rate Relationships Derived from the Above Expressions	121
5.3 Application to Experimental Systems of Interest	124
5.3.1 Tunneling Through Alkane Linkers	124
5.3.2 Tunneling Through Oligonucleotides	125
5.3.3 Tunneling Through Conjugated Molecular Wires	127
5.4 Conclusions	129
5.5 Acknowledgements	129
<b>References</b>	<b>130</b>

## Figures, Tables and Schemes

### Chapter 1

Figure 1.1 Surface passivation by growth of lattice matched GaAs/Al <sub>0.5</sub> Ga <sub>0.5</sub> As interfaces.	8
Figure 1.2 Band bending at semiconductor/liquid junctions.	10
Figure 1.3 Structure of the GaAs(111) surfaces.	14

### Chapter 2

Figure 2.1 SXPS data for the native oxide on the GaAs(111)A surface.	31
Figure 2.2 Uncorrected SXPS data for the As 3d region after HCl(aq) etching for 5 minutes and 30 minutes.	32
Figure 2.3 SXPS fits of the As 3d region of the Cl-terminated GaAs(111)A surface.	34
Figure 2.4 Survey and detailed Cl 2p XPS data for the Cl-terminated GaAs(111)A surface.	35
Figure 2.5 SXPS data for the Ga 3d region of the Cl-terminated GaAs(111)A surface.	36

### Chapter 3

Figure 3.1 Steady-state band edge photoluminescence and quenching mechanisms.	45
Figure 3.2 Detailed area XPS data of the P 2p region of Cl-terminated GaAs(111)A after reaction with PEt <sub>3</sub> .	48

Figure 3.3 Detailed area XPS data for the As 3d and Ga 3d regions of Cl-terminated GaAs(111)A after reaction with $\text{PEt}_3$ .	50
Figure 3.4 SXPS data for the As 3d region of Cl-terminated GaAs(111)A after reaction with $\text{PEt}_3$ .	52
Figure 3.5 SXPS data for the Ga 3d region of Cl-terminated GaAs(111)A after reaction with $\text{PEt}_3$ .	53
Figure 3.6 Detailed area XPS data of the P 2p region of Cl-terminated GaAs(111)A after reaction with $\text{PCl}_3$ .	55
Figure 3.7 SXPS data for the As 3d region of Cl-terminated GaAs(111)A after reaction with $\text{PCl}_3$ .	57
Figure 3.8 SXPS data for the Ga 3d region of Cl-terminated GaAs(111)A after reaction with $\text{PEt}_3$ .	58
Figure 3.9 Detailed area XPS data of the P 2p and Cl 2p regions of native oxide-terminated GaAs(111)A after reaction with $\text{PCl}_3$ .	60
Figure 3.10 SXPS data for the As 3d region of native oxide-terminated GaAs(111)A after reaction with $\text{PCl}_3$ .	62
Figure 3.11 SXPS data for the Ga 3d region of native oxide-terminated GaAs(111)A after reaction with $\text{PCl}_3$ .	63
Figure 3.12 SXPS data for the As 3d region of chloride and phosphine functionalized surfaces after 12 hours of exposure to ambient air.	65
Figure 3.13 SXPS data for the Ga 3d region of chloride and phosphine functionalized surfaces after 12 hours of exposure to ambient air.	66

**Chapter 4**

Figure 4.1 Powder XRD patterns for oxide-terminated and HCl (aq) etched GaAs nanocrystals.	79
Figure 4.2 Detailed area XPS data for the As and Ga 3d regions of oxide-terminated GaAs nanocrystals.	81
Figure 4.3 Diffuse reflectance IR spectra of oxide-terminated GaAs nanocrystals.	82
Figure 4.4 TEM images of oxide-terminated GaAs nanocrystals.	84
Figure 4.5 TEM images of HCl(aq) etched GaAs nanocrystals.	85
Figure 4.6 Detailed area XPS data for the As and Ga 3d regions of Cl-terminated GaAs nanocrystals.	87
Figure 4.7 Detailed area XPS data for the As and Ga 3d regions of hydrazine functionalized GaAs nanocrystals.	90
Figure 4.8 Diffuse reflectance IR spectra of hydrazine functionalized GaAs nanocrystals before and after annealing.	91
Figure 4.9 Detailed area XPS data for the As and Ga 3d regions of hydrazine functionalized GaAs nanocrystals after annealing.	93
Figure 4.10 Detailed area XPS data for the N 1s region of hydrazine functionalized GaAs nanocrystals before and after annealing.	94
Figure 4.11 Steady-state PL spectra of hydrazine functionalized GaAs nanocrystals before and after annealing.	98

**Chapter 5**

Scheme 5.1 Intramolecular electron transfer from a collection of donor-bridge-acceptor units.	109
Table 5.1 Rate constants and electronic coupling matrix elements for systems considered.	123

Portions of the material presented here have appeared in the following references and are reproduced with permission:

Traub, M. C.; Biteen, J. S.; Michalak, D. J.; Webb, L. J.; Brunschwig, B. S.; Lewis, N. S. "High-Resolution X-ray Photoelectron Spectroscopy of Chlorine-Terminated GaAs(111)A Surfaces." *Journal of Physical Chemistry B*. **2006**, *110*, 15641.

Traub, M. C.; Brunschwig, B. S.; Lewis, N. S. "Relationships Between Nonadiabatic Bridged Intramolecular, Electrochemical, and Electrical Electron-Transfer Processes." *Journal of Physical Chemistry C*. 2007, *111*, 6676

Traub, M. C.; Biteen, J. S.; Michalak, D. J.; Webb, L. J.; Brunschwig, B. S.; Lewis, N. S. "Phosphine Functionalization of GaAs(111)A Surfaces." *To Be Submitted*.

Traub, M. C.; Biteen, J. S.; Brunschwig, B. S.; Lewis, N. S. "Passivation of GaAs Nanocrystals By Chemical Functionalization." *To Be Submitted*.

# Chapter 1

## An Introduction to Gallium Arsenide Surface Chemistry

### 1.1 Semiconductor Surface Chemistry and Charge Carrier Dynamics

Since the construction of the first transistor in 1947, semiconductors have provided the foundation for much of the electronic revolution of the second half of the 20th century. The interaction of semiconductors with light and their ability to convert absorbed photons into separated charges make them powerful tools for converting sunlight into sustainable power. With the need to develop carbon-free energy sources and avoid global warming catastrophe, they seem poised to play a similar role in emergent solar energy technologies of the 21st century as well. However, significant scientific barriers need to be overcome before these materials can meet their full potential. In particular, effective methods for controlling carrier traps are essential for effective utilization of semiconductors.

The electronic structure of semiconductors consists of a series of bands, formed from the molecular orbitals of its constituent atoms. Each of these bands contains a continuum of allowed electronic states. The most important of these bands, known as the

valence band and conduction band, are directly below and above the Fermi level,  $E_f$ , respectively. In the ground state of a completely pure semiconductor at 0 K, the valence band consists entirely of filled electronic states, while the conduction band consists entirely of empty states. The energy of the forbidden gap between these bands is known as the band-gap,  $E_G$ . Illumination of the semiconductor with light of energy greater than  $E_G$  leads to excitation of valence electrons into the conduction band, leaving behind holes in the valence band. In the presence of an electric field, these charges can be separated and harnessed to perform useful work. However, carrier recombination reactions compete with charge collection, and unless carefully controlled, can greatly impair the ability of devices to perform useful work.

The overall lifetime of excited carriers in a semiconductor is given by:

$$\frac{1}{\tau} = \sum \frac{1}{\tau_i} \quad (1.1)$$

in which  $\tau_i$  represents the lifetime for each individual recombination pathway. While a variety of recombination mechanisms are possible, in most cases only one or two dominate for a material under a given set of conditions. For indirect band-gap materials such as silicon, recombination in the bulk occurs primarily through trap states. Trap states are electronic states located within the band-gap, resulting from defects. The rate ( $U(E)$ ) of trap-mediated recombination through traps of energy  $E_T$  is given by the Shockley-Read-Hall (SRH) equation:<sup>1,2</sup>

$$U(E_T) = \frac{(pn - n_i^2)}{\{\tau_{p0}(E_T)[n + n_1(E_T)] + \tau_{n0}(E_T)[p + p_1(E_T)]\}} \quad (1.2)$$

where  $p$  and  $n$  are the concentration of holes and electrons respectively,  $n_i^2$  is the equilibrium charge carrier concentration of the intrinsic (undoped) semiconductor,  $\tau_{n0}$

and  $\tau_{p0}$  are the electron and hole lifetimes, and  $n_1$  and  $p_1$  are the concentrations of electrons and holes in traps at  $E_T$ . The lifetimes are given by:<sup>1</sup>

$$\tau_{n0} = \frac{1}{B_n N_T} \quad (1.3)$$

$$\tau_{p0} = \frac{1}{B_p N_T} \quad (1.4)$$

where  $B_n$  and  $B_p$  are the carrier capture coefficients of the traps, and  $N_T$  is the trap density.

The quantities  $n_1$  and  $p_1$  are given by:<sup>1</sup>

$$n_1 = n_i \exp[(E_T - E_i)/kT] \quad (1.5)$$

$$p_1 = n_i \exp[-(E_T - E_i)/kT] \quad (1.6)$$

where  $E_i$  is the Fermi level of the intrinsic semiconductor.

Integration of equation (1.2) over all trap energies yields the total bulk SRH recombination rate. However, it can be seen from equations (1.5) and (1.6) that traps near the valence band edge will efficiently trap holes (large  $p_1$ ) but not electrons (small  $n_1$ ) while traps near the conduction band edge will efficiently trap electrons but not holes. Thus, the maximum recombination rates will correspond to trap states with energies near the center of the band-gap, corresponding to atomic impurities or lattice defects. Modern semiconductor processing techniques allow purities better than 1 defect per  $10^{10}$  lattice atoms, leading to bulk trap-mediated lifetimes in the microsecond range. In contrast, the radiative lifetimes for conduction band to valence band recombination in direct band-gap semiconductors such as GaAs are significantly faster than this ( $<1 \mu\text{s}$ )<sup>3</sup> meaning that bulk trap-mediated recombination can be effectively ignored. This framework can be also used to understand recombination through surface traps.

By substitution of the surface trap densities and carrier concentrations ( $N_{TS}$ ,  $n_s$ , and  $p_s$ ) for bulk values, the SRH equation can be used to evaluate surface recombination rates. These surface recombination rates are often presented in the form:<sup>1,2</sup>

$$U = Sp_{n0}[\exp(-qV/kT) - 1] \quad (1.7)$$

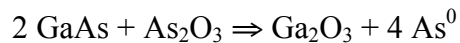
in which  $V$  is the applied voltage on the semiconductor and  $S$  is a pseudo-first order constant known as the surface recombination velocity (SRV) because it has units of  $\text{cm s}^{-1}$ . Under most conditions, the value of  $S$  is largely dependent on the density of trap states at the surface, although under conditions of very high band bending low SRVs may be observed on highly defective surfaces.<sup>4</sup>

Even for high-purity semiconductor single crystals in a completely inert environment, one would expect a higher defect density at surfaces than in the bulk due to dangling bonds at coordinatively unsaturated surface sites. These problems become even more severe for almost any real device or experimental system, in which exposure of the surface to atmosphere, solutions, or metals leads to chemical reactions and further trap state formation. Without some method to passivate these surface states, semiconductor devices display behavior dominated by interface effects even though only a small fraction of the atoms lie on the surface. Recent interest in nanoscale and quantum confined semiconductor systems, in which up to a quarter of the total atoms are surface sites, has highlighted the importance of finding new ways to control semiconductor surface chemistry.

## 1.2 Surface Passivation Techniques: Silicon vs. Gallium Arsenide

GaAs has many advantages over Si for device applications, in particular higher carrier mobilities<sup>5</sup> and a direct band-gap that allows complete absorption of all photons with energies above the band-gap for less than 1  $\mu\text{m}$  thickness. Since the 1950s, it has been hoped that GaAs would supplant Si as the material of choice for electronics applications.<sup>6</sup> Its failure to do so is in large part due to our inability to discover an inexpensive, stable method of surface passivation.

For most applications, Si surface passivation is achieved by the growth of a thermal oxide layer on the Si(100) surface (the so-called device face).<sup>5</sup> This oxide, grown by simply heating Si in the presence of dry  $\text{O}_2$ , forms a single phase that is chemically inert against further reaction and has a sufficiently low density of defects to achieve  $S = 330 \text{ cm s}^{-1}$  for electrons.<sup>7</sup> In contrast, oxidation of GaAs leads to formation of multiple oxide phases, including phases for multiple oxidation states for both Ga ( $\text{Ga}_2\text{O}$  and  $\text{Ga}_2\text{O}_3$ ) and As ( $\text{As}_2\text{O}_3$  and  $\text{As}_2\text{O}_5$ ) and mixed composition phases ( $\text{GaAsO}_4$ ).<sup>8</sup> Further, the oxide/GaAs interface is not thermodynamically stable and, particularly at higher temperatures, can lead to degradation by the reaction:<sup>8</sup>



Elemental As is known to introduce a carrier trap state in GaAs, and thermally oxidized surfaces with low SRVs were never achieved. The failure to capitalize on the superior properties of GaAs helped lead to the saying that “GaAs is the material of the future, and will always be the material of the future.”

More recently, there has been great interest in developing alternative methods of passivation for Si. Etching with aqueous hydrofluoric acid or buffered HF solutions leads to H-terminated surfaces with exceptionally low SRVs.<sup>9</sup> While these surfaces are reactive in air and quickly form high defect density native oxide interfaces, they can be used as starting points for the formation of more stable bonds. In particular, formation of surficial Si-C bonds has become a widely used passivation strategy for bulk and porous Si surfaces. These bonds can be formed directly from the H-terminated surfaces<sup>10,11</sup> or through a two-step halogenation/alkylation procedure.<sup>12-14</sup> These surfaces are resistant to chemical oxidation and display long lifetimes even after extended exposure to ambient air.<sup>15</sup> Additionally this chemistry can be used to introduce a diverse set of functional groups,<sup>16-19</sup> allowing a wide variety of potential applications.

Once again, GaAs presents a more challenging situation due to the presence of more than one atomic species on the surface and a corresponding increase in available surface-binding modes. The character of dangling bonds on these surfaces can be predicted from simple electron-counting arguments. Formation of charge-neutral surfaces means that Ga dangling bonds will tend to be empty orbitals, while As dangling bonds will tend to be filled. Thus, Ga surface sites are generally electrophilic, and As surface sites are generally nucleophilic. Effective passivation requires accommodating both types of sites. While this constraint has impeded research on GaAs surface passivation chemistry, some progress has been made on this problem.

### 1.3 Chemical Passivation of GaAs Surfaces

The most widely used method of GaAs passivation for device applications is the growth of an epitaxial capping layer of  $\text{Al}_{0.5}\text{Ga}_{0.5}\text{As}$ . At this level of Al content, the  $\text{Al}_x\text{Ga}_{1-x}\text{As}$  is lattice matched with GaAs and forms a low-defect interface. The band offsets of the  $\text{Al}_x\text{Ga}_{1-x}\text{As}$  cap at both the valence band and conduction band edges confine carriers within the GaAs layer and prevent them from recombining through states on the surface (figure 1.1). The SRV at a GaAs/ $\text{Al}_x\text{Ga}_{1-x}\text{As}$  interface has been measured as  $450 \pm 100 \text{ cm s}^{-1}$ .<sup>20,21</sup> This is in contrast to the SRV of  $\approx 5 \times 10^5 \text{ cm s}^{-1}$  measured for the GaAs/native oxide interface, a value sufficiently large to ensure that essentially every carrier that reaches the surface recombines. However, the requirement of costly, low-throughput epitaxial techniques to achieve this passivation has contributed to the limited use of GaAs.

GaAs passivation has also been explored in the context of liquid junctions. Semiconductor/liquid junctions are a critical component of photoelectrochemical (PEC) solar cells, and the nature of these junctions can determine the electrical properties of the entire device. Before considering the passivation of surface states in these systems, it is useful to define their behavior in the absence of such states. For an idealized junction at equilibrium, electron transfer at the interface makes the Fermi level of the semiconductor and the redox potential of the solution ( $E(A/A^-)$ ) equal. For an n-doped semiconductor, electron transfer from the semiconductor will occur from the donor dopant atoms rather than the semiconductor lattice itself. Even in relatively dilute solutions, the concentration of A in solution ( $10 \text{ mM} \approx 6 \times 10^{18} \text{ cm}^{-3}$ ) is much larger than the concentration of

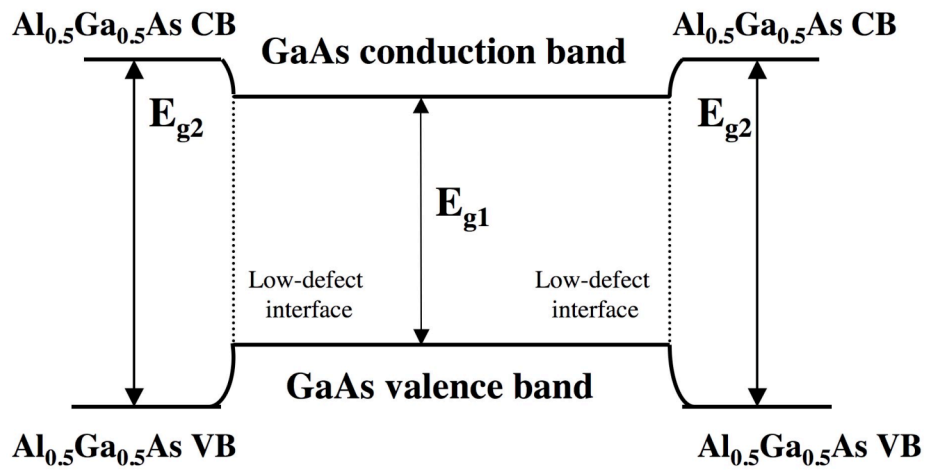


**Figure 1.1.** Passivation of GaAs with Al<sub>0.5</sub>Ga<sub>0.5</sub>As. The lattice-matched Al<sub>0.5</sub>Ga<sub>0.5</sub>As cap yields an interface with a low density of electrical traps, while carriers are contained within the GaAs layer by band offsets at the valence and conduction band edges.

ionizable dopant atoms in the semiconductor,<sup>22</sup> resulting in an equilibrated  $E_f$  essentially identical to that of the isolated solution (figure 1.2).

In this idealized model, essentially all dopants up to a depth  $W$  are considered to have donated their electrons to the solution, while carriers from dopants past this depth are still trapped in the lattice. This process leaves a negative charge in the solution at the interface, and an equally positively charged depletion region of width  $W$  within the semiconductor. The negative charge in solution is concentrated in the double layer immediately at the interface; while even at relatively high doping levels ( $10^{18} \text{ cm}^{-3}$ ) the depletion region extends  $>100 \text{ nm}$  into the semiconductor. The field from this depletion region bends the bands of the semiconductor, leading to a barrier height  $\Phi_b$  defined as:

$$\Phi_b = \frac{[E(A/A^-) - E_{CB}]}{q} \quad (1.8)$$

and a built-in voltage  $V_{bi}$ :

$$V_{bi} = \left( \frac{qN_d}{2\epsilon_s} \right) W^2 \quad (1.9)$$

where  $N_d$  and  $\epsilon_s$  are, respectively, the dopant density and the static dielectric constant of the semiconductor. Larger values for  $V_{bi}$  and  $\Phi_b$  typically produce higher open-circuit voltages ( $V_{oc}$ ) and efficiencies ( $\eta$ ) in solar conversion devices (figure 1.2).

In the presence of surface carrier traps, electron transfer can proceed from both bulk dopants and the surface trap states. The greater the extent to which charge equilibration occurs through these surface states, the less ionization of the bulk occurs, with a corresponding decrease in the depletion width and the corresponding band bending. In this case, the value of  $V_{bi}$  and  $\Phi_b$  is now dependent not only on the relative energetics of  $E_f$  and  $E(A/A^-)$ , but also on the energetics and density of surface states. This

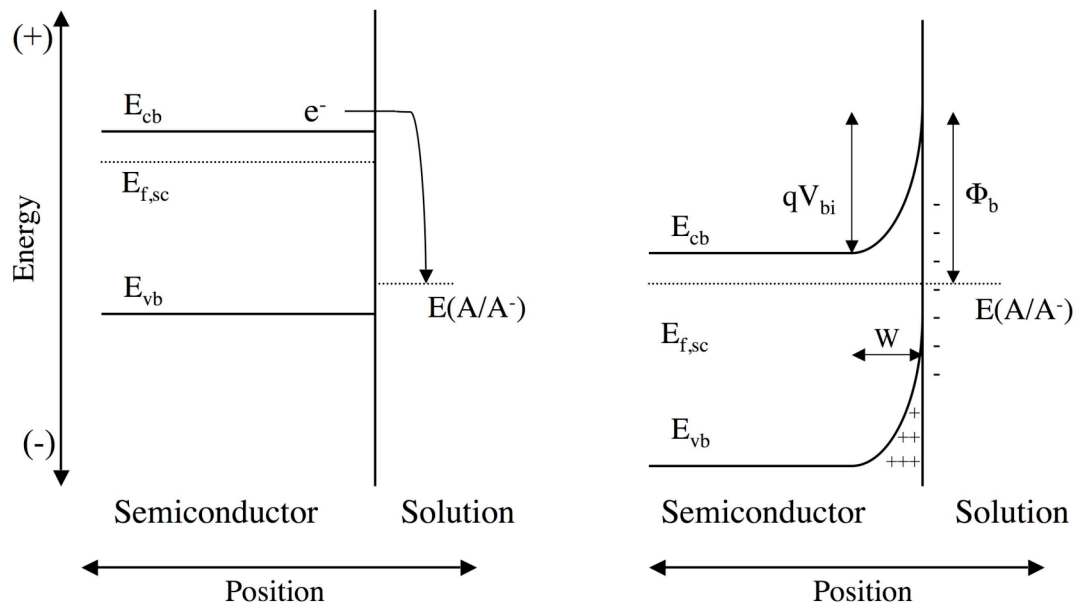


**Figure 1.2.** Left—The semiconductor/liquid junction before equilibrium. Right—The semiconductor/liquid junction at equilibrium. The labels  $V_{bi}$ ,  $\Phi_b$ , and  $W$  represent, respectively, the built-in voltage, barrier height and depletion region width.

decreased dependence of the barrier height is known as Fermi level pinning. The extent of Fermi level pinning can be obtained from a plot of  $V_{bi}$  or  $\Phi_b$  vs.  $E(A/A^{\cdot-})$  measured for a series of redox couples.<sup>22</sup> At an ideal junction, this plot will have a slope of 1, while for a completely pinned system the slope will be 0. Trap state densities of  $\approx 1\%$  of a surface monolayer are sufficient to result in complete Fermi level pinning.<sup>23</sup>

In contact with a ferrocene/ferrocenium redox couple in acetonitrile, n-GaAs has yielded solar conversion efficiencies as high as 11%.<sup>24</sup> However, variation of  $E(A/A^{\cdot-})$  over 1.2 V through a series of redox couples resulted in only 300 mV of variation in measured barrier heights.<sup>24</sup> Observation of photoeffects for redox couples outside of band-gap for both n-GaAs and p-GaAs in  $\text{CH}_3\text{CN}$ , along with very limited photovoltage response to the potential of the redox couple, were attributed to surface pinning effects.<sup>25</sup> Similar effects, although of lesser magnitude, were observed for GaAs photoelectrodes in tetrahydrofuran,<sup>26</sup> and GaAs photoanodes in methanol were subject to corrosion reactions.<sup>27</sup> There are no reports, to my knowledge, of GaAs displaying ideal junction behavior in nonaqueous electrolytes.

Beyond simple Fermi level pinning effects, unpassivated GaAs photoanodes in aqueous solutions actually undergo dissolution reactions in which holes at the surface form oxides, which subsequently dissolve in solution. An important breakthrough for the feasibility of these systems was the discovery that chalcogenide redox couples of the form  $\text{X}_2^{2-}/\text{X}^{2-}$  ( $\text{X} = \text{S}, \text{Se}, \text{Te}$ ) could stabilize small band-gap compound semiconductors against these reactions.<sup>28,29</sup> In particular, 9% efficient regenerative PEC solar cells based on GaAs and a  $\text{Se}_2^{2-}/\text{Se}^{2-}$  redox couple were found to be stable.<sup>29</sup> This stability is primarily due to hole collection by  $\text{Se}^{2-}$  efficiently competing kinetically with dissolution

reactions, although formation of a passivating  $\text{Ga}_2\text{Se}_3$  layer on the surface may play a role as well. High concentrations of  $\text{I}^-$  have been reported to stabilize GaAs in aqueous solutions by a similar mechanism.<sup>30,31</sup>

A further improvement in the efficiency of these cells was achieved by pre-exposing the surfaces to solutions of  $\text{RuCl}_3(\text{aq.})$ , increasing both their open-circuit voltage and fill factor.<sup>32</sup> Similar behavior was observed with other group VIII B metal ions ( $\text{Co}^{\text{III}}$ ,  $\text{Os}^{\text{III}}$ ,  $\text{Ir}^{\text{III}}$ ,  $\text{Rh}^{\text{III}}$ ).<sup>33,34</sup> Photoluminescence decay measurements of these metal-treated surfaces in air showed SRVs of  $3.5 \times 10^4 \text{ cm s}^{-1}$ , suggesting that these metal ions improved performance by reducing the density of surface states.<sup>35</sup> However, similar measurements on GaAs surfaces in contact with aqueous  $\text{Se}_2^{2-}/\text{Se}^{2-}$  solutions showed SRVs of  $5 \times 10^3 \text{ cm s}^{-1}$  without metal treatment, while surfaces that had been preexposed to solutions of  $\text{Co}(\text{NH}_3)^{3+}$  had SRVs of  $2 \times 10^5 \text{ cm s}^{-1}$ .<sup>36</sup> These results imply that the primary mechanism for the performance enhancement of metals in these PEC cells is to catalyze hole transfer to the redox couple, and that these treatments are not a general method for reducing surface traps.

These successes with chalcogenide passivation in PEC systems lead to the investigation of sulfur as a passivating agent for solid-state systems as well. Yablonoitch and co-workers demonstrated that treatment of GaAs(100) with  $\text{Na}_2\text{S}$  strongly increased its photoluminescence intensity.<sup>37</sup> Microwave conductivity measurements of these sulfide-passivated samples were used to quantify the effectiveness of this passivation and SRVs of  $\approx 10^3$  were reported.<sup>38</sup> This treatment was also shown to help unpin the Fermi level in the solid state and produce increased dependence of barrier heights on metal contacts in Schottky junctions.<sup>39</sup> Similar effects have also been

achieved with a variety of organic thiols,<sup>40</sup> allowing formation of self-assembled monolayers on GaAs.<sup>41,42</sup> Increased stability and improved electronic properties have also been reported after deposition of a selenide/selenate layer at the surface.<sup>43</sup> More recently, hydrazine has been used to passivate GaAs with surficial Ga-N bonds, with reported steady-state PL enhancements greater than those observed with sulfur-based treatments.<sup>44</sup>

#### **1.4 New Strategies for GaAs Passivation**

The vast majority of previous work on GaAs passivation has focused on the (100) crystal face. However, there are advantages to passivating the (111) crystal faces (figure 1.3). GaAs has two polar (111) faces, the Ga-rich (111)A face and the As-rich (111)B face, containing only Ga or As atoms respectively. For many applications, such as PEC cells, passivation is only required on one crystal face, while the back face is ohmically contacted to a metal. Selection of the (111) faces for these applications means that only As or Ga sites need to be passivated, not both simultaneously.

A second advantage of these systems is a reduction in steric constraints for chemical groups on the surface. Dangling bonds on the (100) surface face each other, limiting the number of sites at which binding of passivating groups can occur. In contrast, the (111) planes contain only dangling bonds normal to the surface (figure 1.3). where there is less steric constraint on the packing of surface groups. It has been demonstrated that on the Si(111) surface, methyl groups are small enough to fit atop every surface site in a close-packed array.<sup>45</sup> Given the interatomic spacing of 3.4 Å

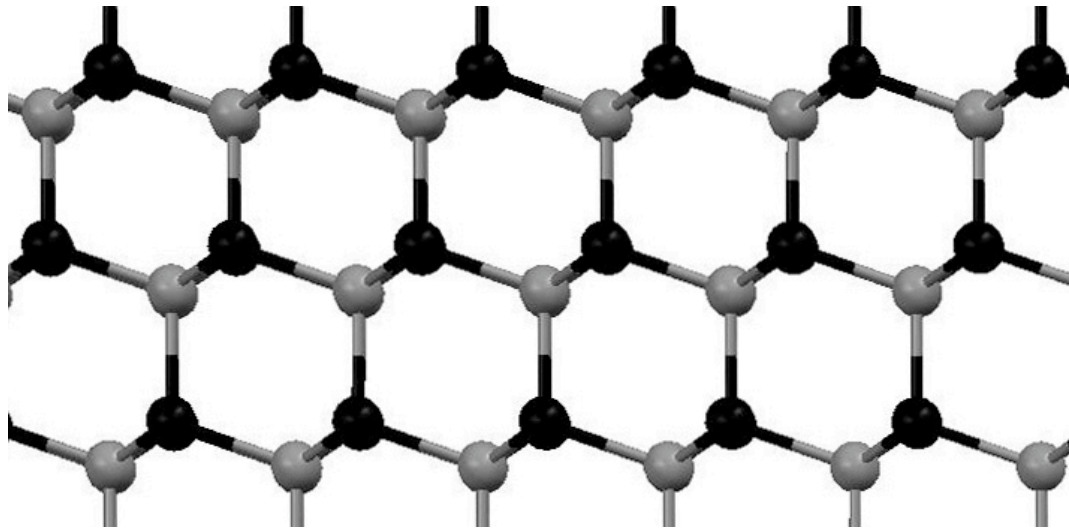


**Figure 1.3.** The cross-sectional structure of GaAs and its (111) surfaces. Dark atoms represent Ga and light atoms represent As. The (111)A face at the top of image has Ga dangling bonds normal to the surface plane, while (111)B face at the bottom of the image has As dangling bonds normal to the surface plane.

between Ga sites on the (111)A surface, small terminal groups such as Cl, CH<sub>3</sub> and NH<sub>2</sub> should be able to fit atop every surface Ga atom.

Of the polar GaAs(111) faces, the (111)A face is particularly promising for developing new methods of passivation chemistry. Measurement of etch rates and etch pit formation have shown that the (111)A surface is the most stable low-index GaAs crystal face under acidic conditions.<sup>6,46</sup> This result suggests that these surfaces should be least likely to form etch related defects during the process of oxide removal. More recently, it was observed that well-ordered surfaces could be formed on GaAs(111)A by etching in HCl (aq.) solutions.<sup>47,48</sup> These surfaces displayed (1 x 1) low-energy electron diffraction (LEED) patterns and X-ray absorption near-edge spectra (XANES) indicated the presence of Ga-Cl  $\sigma$  bonds. Together, these data suggest that the surfaces are well ordered over large areas and terminated with surface normal Ga-Cl bonds.

This surface provides a starting point for further functionalization chemistry. Terminal-Cl bonds on Ga should be reactive towards more strongly electron donating substituents. A detailed exploration of this chemistry is the primary subject of this work. Chapter 2 describes a high-resolution photoelectron exploration of the chemistry of this Cl-terminated surface. Chapter 3 discusses the reactivity of this surface toward phosphine reagents, a novel passivating reagent for GaAs. Chapter 4 expands these passivation techniques to surfaces on the nanoscale. Controlled chemical surface passivation produces a drastic increase in the photoluminescence of GaAs nanocrystals. This improvement in electronic properties is correlated with the removal of a specific trap (As<sup>0</sup>) on the nanocrystal surfaces. The final chapter of this thesis addresses a separate, although related, scientific problem. Many application of interest for nanoscale

electronics, including many utilizing GaAs nanocrystals and nanowires, require electron transfer through surface bound chemical moieties. Such groups are often known as “molecular wires,” emphasizing current flow rather than traditional electron transfer reactions. In this chapter, a theoretical approach, based on Marcus theory,<sup>49,50</sup> is used to develop a relationship between electron transfer in donor-acceptor systems and resistances in molecular wires. Resistances predicted by this formulation are compared to reported experimental values.

**References**

- (1) Lewis, N. S.; Rosenbluth, M. L. Theory of Semiconductor Materials. In *Photocatalysis: Fundamentals and Applications*; Serpone, N., Pelizzetti, E., Eds.; Wiley Interscience: New York, 1989.
- (2) Shockley, W.; Read, W. T. *Physical Review* **1952**, *87*, 835.
- (3) Nelson, R. J.; Sobers, R. G. *Journal of Applied Physics* **1978**, *49*, 6103.
- (4) Gstrein, F.; Michalak, D. J.; Royea, W. J.; Lewis, N. S. *Journal of Physical Chemistry B* **2002**, *106*, 2950.
- (5) Sze, S. M. *The Physics of Semiconductor Devices*, 2nd ed.; John Wiley & Sons: New York, 1981.
- (6) Gatos, H. C. *Surface Science* **1994**, *300*, 1.
- (7) Yablonovitch, E.; Swanson, R. M.; Eades, W. D.; Weinberger, B. R. *Applied Physics Letters* **1986**, *48*, 245.
- (8) Thurmond, C. D.; Schwartz, G. P.; Kammlott, G. W.; Schwartz, B. *Journal of the Electrochemical Society* **1980**, *127*, 1366.
- (9) Yablonovitch, E.; Allara, D. L.; Chang, C. C.; Gmitter, T.; Bright, T. B. *Physical Review Letters* **1986**, *57*, 249.
- (10) Linford, M. R.; Fenter, P.; Eisenberger, P. M.; Chidsey, C. E. D. *Journal of the American Chemical Society* **1995**, *117*, 3145.
- (11) Buriak, J. M.; Stewart, M. P.; Geders, T. W.; Allen, M. J.; Choi, H. C.; Smith, J.; Raftery, D.; Canham, L. T. *Journal of the American Chemical Society* **1999**, *121*, 11491.
- (12) Bansal, A.; Li, X. L.; Lauermann, I.; Lewis, N. S.; Yi, S. I.; Weinberg, W. H. *Journal of the American Chemical Society* **1996**, *118*, 7225.

- (13) Bansal, A.; Li, X. L.; Yi, S. I.; Weinberg, W. H.; Lewis, N. S. *Journal of Physical Chemistry B* **2001**, *105*, 10266.
- (14) Terry, J.; Linford, M. R.; Wigren, C.; Cao, R. Y.; Pianetta, P.; Chidsey, C. E. D. *Applied Physics Letters* **1997**, *71*, 1056.
- (15) Webb, L. J.; Lewis, N. S. *Journal of Physical Chemistry B* **2003**, *107*, 5404.
- (16) Juang, A.; Scherman, O. A.; Grubbs, R. H.; Lewis, N. S. *Langmuir* **2001**, *17*, 1321.
- (17) Hurley, P. T.; Nemanick, E. J.; Brunshwig, B. S.; Lewis, N. S. *Journal of the American Chemical Society* **2006**, *128*, 9990.
- (18) Bocking, T.; James, M.; Coster, H. G. L.; Chilcott, T. C.; Barrow, K. D. *Langmuir* **2004**, *20*, 9227.
- (19) Nemanick, E. J.; Hurley, P. T.; Brunshwig, B. S.; Lewis, N. S. *Journal of Physical Chemistry B* **2006**, *110*, 14800.
- (20) Nelson, R. J. *Journal of Vacuum Science & Technology* **1978**, *15*, 1475.
- (21) Nelson, R. J.; Sobers, R. G. *Applied Physics Letters* **1978**, *32*, 761.
- (22) Tan, M. X.; Laibinis, P. E.; Nguyen, S. T.; Kesselman, J. M.; Stanton, C. E.; Lewis, N. S. Principles and Applications of Semiconductor Photoelectrochemistry. In *Progress in Inorganic Chemistry*, vol 41, 1994; pp 21.
- (23) Bard, A. J.; Bocarsly, A. B.; Fan, F. R. F.; Walton, E. G.; Wrighton, M. S. *Journal of the American Chemical Society* **1980**, *102*, 3671.
- (24) Casagrande, L. G.; Juang, A.; Lewis, N. S. *Journal of Physical Chemistry B* **2000**, *104*, 5436.
- (25) Kohl, P. A.; Bard, A. J. *Journal of the Electrochemical Society* **1979**, *126*, 59.

- (26) Diquarto, F.; Bard, A. J. *Journal of Electroanalytical Chemistry* **1981**, *127*, 43.
- (27) Abshire, T. A.; Richmond, G. L. *Journal of Physical Chemistry B* **2000**, *104*, 1602.
- (28) Ellis, A. B.; Bolts, J. M.; Kaiser, S. W.; Wrighton, M. S. *Journal of the American Chemical Society* **1977**, *99*, 2848.
- (29) Chang, K. C.; Heller, A.; Schwartz, B.; Menezes, S.; Miller, B. *Science* **1977**, *196*, 1097.
- (30) Allongue, P.; Cachet, H.; Clechet, P.; Froment, M.; Martin, J. R.; Verney, E. *Journal of the Electrochemical Society* **1987**, *134*, 620.
- (31) Verney, E.; Martin, J. R.; Jaffrezicrenault, N.; Clechet, P. *Journal Of Electroanalytical Chemistry* **1986**, *209*, 219.
- (32) Parkinson, B. A.; Heller, A.; Miller, B. *Applied Physics Letters* **1978**, *33*, 521.
- (33) Tufts, B. J.; Abrahams, I. L.; Santangelo, P. G.; Ryba, G. N.; Casagrande, L. G.; Lewis, N. S. *Nature* **1987**, *326*, 861.
- (34) Lunt, S. R.; Casagrande, L. G.; Tufts, B. J.; Lewis, N. S. *Journal of Physical Chemistry* **1988**, *92*, 5766.
- (35) Nelson, R. J.; Williams, J. S.; Leamy, H. J.; Miller, B.; Casey, H. C.; Parkinson, B. A.; Heller, A. *Applied Physics Letters* **1980**, *36*, 76.
- (36) Ryba, G. N.; Kenyon, C. N.; Lewis, N. S. *Journal of Physical Chemistry* **1993**, *97*, 13814.
- (37) Skromme, B. J.; Sandroff, C. J.; Yablonovitch, E.; Gmitter, T. *Applied Physics Letters* **1987**, *51*, 2022.

- (38) Yablonovitch, E.; Sandroff, C. J.; Bhat, R.; Gmitter, T. *Applied Physics Letters* **1987**, *51*, 439.
- (39) Fan, J. F.; Oigawa, H.; Nannichi, Y. *Japanese Journal of Applied Physics Part 2—Letters* **1988**, *27*, L2125.
- (40) Lunt, S. R.; Santangelo, P. G.; Lewis, N. S. *Journal of Vacuum Science & Technology B* **1991**, *9*, 2333.
- (41) Adlkofer, K.; Eck, W.; Grunze, M.; Tanaka, M. *Journal of Physical Chemistry B* **2003**, *107*, 587.
- (42) Adlkofer, K.; Tanaka, M.; Hillebrandt, H.; Wiegand, G.; Sackmann, E.; Bolom, T.; Deutschmann, R.; Abstreiter, G. *Applied Physics Letters* **2000**, *76*, 3313.
- (43) Sandroff, C. J.; Hegde, M. S.; Farrow, L. A.; Bhat, R.; Harbison, J. P.; Chang, C. *Journal of Applied Physics* **1990**, *67*, 586.
- (44) Berkovits, V. L.; Ulin, V. P.; Losurdo, M.; Capezzuto, P.; Bruno, G.; Perna, G.; Capozzi, V. *Applied Physics Letters* **2002**, *80*, 3739.
- (45) Yu, H. B.; Webb, L. J.; Ries, R. S.; Solares, S. D.; Goddard, W. A.; Heath, J. R.; Lewis, N. S. *Journal of Physical Chemistry B* **2005**, *109*, 671.
- (46) Tarui, Y.; Komiya, Y.; Harada, Y. *Journal of the Electrochemical Society* **1971**, *118*, 118.
- (47) Lu, Z. H.; Chatenoud, F.; Dion, M. M.; Graham, M. J.; Ruda, H. E.; Koutzarov, I.; Liu, Q.; Mitchell, C. E. J.; Hill, I. G.; McLean, A. B. *Applied Physics Letters* **1995**, *67*, 670.
- (48) Lu, Z. H.; Tyliczszak, T.; Hitchcock, A. P. *Physical Review B* **1998**, *58*, 13820.
- (49) Marcus, R. A. *Annual Review of Physical Chemistry* **1964**, *15*, 155.

- (50) Marcus, R. A. *Journal of Chemical Physics* **1965**, *43*, 679.

## Chapter 2

# High-Resolution Photoelectron Spectroscopy of Chlorine-Terminated GaAs(111)A Surfaces

### 2.1 Introduction—Analytical Chemistry of the GaAs Surface

While a wide variety of analytic methods for identification of chemical species have been developed over the past century, most of these techniques are ill suited for studying the chemistry of macroscopic single crystal surfaces. This deficiency is primarily due to the vanishingly small number of detectable surface species, particularly relative to the amount of bulk material. However, while the thickness of a single layer of surface atoms is only  $\approx 3 \text{ \AA}$  and monolayer coverages are nominally only  $\approx 10^{-9} \text{ mol cm}^{-2}$ , the surface properties of a semiconductor material can dominate its electrical properties. The importance of these surface sites necessitates surface-sensitive analytical tools to develop a detailed understanding of their behavior.

One powerful tool for selectively probing these surface sites is X-ray photoelectron spectroscopy (XPS). In this technique, X-rays are used to photodissociate

core level electrons, whose kinetic energy,  $E_{KE}$ , is measured. This kinetic energy is related to a characteristic binding energy  $E_{BE}$  by:

$$E_{BE} = h\nu - E_{KE} - \phi \quad (2.1)$$

where  $h\nu$  is the energy of the X-rays and  $\phi$  is work function of the detector. While  $h\nu$  and  $\phi$  are instrument dependent parameters,  $E_{BE}$  is an instrument independent energy characteristic of the atomic orbital from which the photoelectron was ejected. The ability to selectively measure surfaces comes from the relatively short inelastic mean free path of photoelectrons in a solid material ( $\approx 2-20 \text{ \AA}$ ). This short mean free path means that photoelectrons generated deeper in the sample than the immediate surface region will be scattered by a bulk phonon before escaping.

Since XPS measures the energy of core level, rather than valence level, electrons, the observed binding energies are not as sensitive to the local bonding environment of the probed atoms as are traditional solution analytic techniques such as nuclear magnetic resonance spectroscopy. However, even the core electron levels will shift in response to changes in an atom's oxidation state, and these changes can be used to infer information about the chemistry of the surface. The magnitude of the change observed necessarily depends on the energy of the chemical state at the surface relative to the bulk. While the bonds in GaAs are quite covalent ( $X_{As} - X_{Ga} = 0.37$ ), the As atoms are formally  $As^{-3}$  and the Ga formally  $Ga^{+3}$ . Thus, formation of surface oxides corresponds to a larger shift in formal oxidation state for As than for Ga, and As oxide peaks are shifted further from the bulk GaAs values than are Ga oxide peaks.

In this work, characterization of GaAs surfaces has been accomplished by two complementary XPS techniques. In the first, experiments were performed at Caltech

using a fixed energy (1486.6 eV) Al K $\alpha$  X-ray source. The energy of these X-rays allowed investigation of binding energies over a range of more than 1200 eV, covering virtually all elements of interest, including Ga, As, Cl, O, C, N, S, and P. These fixed energy X-ray source experiments were used to determine the elemental composition of functionalized surfaces.

For the other set of XPS experiments, surfaces were illuminated with soft X-ray synchrotron radiation. While the energy used in these experiments (90 eV) was not sufficient to make measurements on atoms other than Ga and As, highly detailed information on these elements could be obtained. This technique, referred to herein as SXPS, provides even greater surface sensitivity than standard XPS, and more specific bonding information for the atop atoms. Further, because of the high intensity of the synchrotron radiation, experiments could be performed at higher resolution without prohibitively long collection times. Together, these techniques provide a detailed picture of the chemistry of functionalized surfaces.

Etching GaAs(111)A with a dilute solution of HCl(aq) has been shown to produce a well-ordered surface terminated with Ga-Cl  $\sigma$  bonds.<sup>1,2</sup> This Cl-terminated surface should provide an excellent platform for further chemical functionalization reactions. A complete picture of this starting surface is required to understand fully the subsequent functionalization chemistry of such systems. Before performing further reactions on this Cl-terminated surface, it was important to quantify its chemistry and the binding energy of species on this surface, as well as the native oxide. These measurements are necessary reference points, both for how cleanly reactions may proceed and what binding energies might be expected for other species on the surface.

## 2.2 Experimental

### 2.2.1 Materials and Methods

GaAs(111) wafers that had been polished on the (111)A face were obtained from AXT (Fremont, CA). The 325  $\mu\text{m}$  thick wafers were  $n^+$  doped with Si to a carrier concentration of  $1.7 \times 10^{18} \text{ cm}^{-3}$ . All solvents and chemicals for the surface functionalization reactions were used as received from Aldrich Chemical Corp.  $\text{H}_2\text{O}$  with a resistivity  $>17.8 \text{ M}\Omega \text{ cm}^{-1}$ , obtained from a Barnsted Nanopure system, was used at all times.

Prior to performing any surface chemistry, all samples were cleaned and degreased by successive rinses in  $\text{H}_2\text{O}$ ,  $\text{CH}_3\text{OH}$ , acetone, 1,1,1-trichloroethane (TCE), acetone,  $\text{CH}_3\text{OH}$ , and  $\text{H}_2\text{O}$ . To form the Cl-terminated GaAs(111)A surface, samples were etched at room temperature for 5–30 min in a 1:1 (by volume) ( $\approx 6 \text{ M}$ ) mixture of concentrated  $\text{HCl}(\text{aq})$ : $\text{H}_2\text{O}$ , and then were dried, without rinsing, under a stream of  $\text{N}_2(\text{g})$ .

### 2.2.2 Instrumentation

#### 2.2.2.1. XPS Measurements

Preliminary spectroscopic data on functionalized GaAs(111)A surfaces were collected using an M-Probe XPS system that has been described previously.<sup>3,4</sup> For these experiments, 1486.6 eV X-rays generated from an Al  $K\alpha$  source illuminated the sample from an incident angle of  $35^\circ$  off of the surface. Photoelectrons emitted along a trajectory  $35^\circ$  off of the surface were collected by a hemispherical analyzer. After chemical functionalization, samples were inserted via a quick-entry load lock into the ultra-high-vacuum (UHV) system and were kept at a base pressure of  $\leq 1 \times 10^{-9}$  Torr. All samples

were sufficiently electrically conductive at room temperature that no compensation for charging effects was required. On each sample, a “survey” scan of core photoelectron binding energies from 1 to 1200 binding eV was collected to identify the chemical species present on the surface. Higher resolution data were collected for atoms of interest, particularly those whose binding energy was too high to be examined with the synchrotron experiments, such as the Cl 2p and O 1s regions. Energies deduced from all of the XPS measurements are reported herein as binding energies.

A simple model previously applied to Si<sup>5</sup> was used to calculate the overlayer coverages based on the observed intensities of the peaks in the higher resolution scans. The coverage  $\Phi_{ov}$  in relation to the bulk Ga signal can be estimated from:

$$\Phi_{ov} = \left\{ \left( \frac{\lambda \sin \theta}{a_{ov}} \right) \left( \frac{SF_{Ga}}{SF_{ov}} \right) \left( \frac{\rho_{Ga}}{\rho_{ov}} \right) \left( \frac{I_{ov}}{I_{Ga}} \right) \right\} \quad (2.2)$$

where  $\lambda$  is the photoelectron sample depth of the experiment (estimated as 1.6 nm on this instrument),  $a_{ov}$  is the atomic diameter of the overlayer species,  $\theta$  is the take-off angle of photoelectrons from the substrate (35°), and  $SF$ ,  $\rho$ , and  $I$  are, respectively, the modified Scofield sensitivity factor,<sup>6</sup> solid-state volumetric density, and integrated peak intensity for the relevant species. For this work, solid-state densities of 2.0 and 2.66 g cm<sup>-3</sup> were used for Cl and Ga in GaAs, while modified sensitivity factors of 2.4 and 1.22 were used for these same atoms. The atomic diameter of the overlayer atoms was estimated using the equation:

$$a_{ov} = \left( \frac{A_{ov}}{\rho_{ov} N_A} \right)^{\frac{1}{3}} \quad (2.3)$$

where  $A_{ov}$  is the atomic weight of the overlayer atom,  $\rho_{ov}$  is the solid state density, and  $N_A$  is Avogadro's number. Integrated peak areas for  $I_{Ga}$  and  $I_{ov}$  were measured using the ESCA 2000 software package.

#### 2.2.2.2 SXPS Measurements

High-resolution soft X-ray photoelectron spectroscopy (SXPS) experiments were performed on beamline U4A at the National Synchrotron Light Source (NSLS) at Brookhaven National Laboratory.<sup>7</sup> The sample was introduced through a quick-entry load lock into a two-stage UHV system that was maintained at  $\leq 1 \times 10^{-9}$  torr. The beamline had a spherical grating monochromator that selected photon energies between 10 and 200 eV with a resolution of 0.3 eV. The selected excitation energy was not calibrated independently because this study was principally concerned with shifts in core orbital binding energies relative to the bulk signals, as opposed to determination of absolute binding energies. Samples were illuminated at an incident energy of 90 eV, and the emitted photoelectrons were collected at normal to the sample surface by a VSW 100 mm hemispherical analyzer that was fixed at 45° off of the axis of the photon source. The energy resolution of the hemispherical analyzer was 0.1 eV. The beam intensity from the synchrotron ring was measured independently, and the data in each scan were normalized to account for changes in photon flux during the scan. No charging or beam-induced damage was observed on the samples during data collection. The limited range of excitation energies available at this beamline, although ideal for high-resolution core level spectroscopy of surface species in both As 3d and Ga 3d regions, prevented the

recording of survey scans of the surface that would have identified other atomic species present.

The escape depths of As and Ga photoelectrons were estimated using an empirical relationship described by Seah.<sup>8</sup> For a photoelectron with kinetic energy  $E$  (in eV) escaping from a pure element, the electron mean free path,  $\lambda_{el}$ , can be calculated from:

$$\lambda_{el} = 0.41a_{el}^{1.5}E^{0.5} \quad (2.4)$$

where  $\lambda_{el}$  and the atomic size of the element,  $a_{el}$ , are both in nanometers. For GaAs, a compound semiconductor made up of two atoms of similar size, an average size  $a_{avg} = 0.283$  nm was calculated using, with  $A_{avg}$  as the average atomic weight of an atom in the GaAs lattice ( $72.322$  g mol<sup>-1</sup>),  $\rho_{GaAs}$  is the bulk density of the crystal ( $5.319$  g cm<sup>-3</sup>).<sup>9</sup> For a Ga 3d photoelectron with a kinetic energy of  $\approx 71$  eV, eq (2.4) yields an electron mean free path of  $\lambda_{Ga} = 0.52$  nm. For an As 3d photoelectron with kinetic energy of  $\approx 49$  eV,  $\lambda_{As} = 0.43$  nm. Because the distance between two (111)A planes is  $0.326$  nm, the majority of the Ga and As 3d signals should therefore arise from the top two atomic layers of Ga and As, respectively.

Before fitting the data, a Shirley background was calculated and subtracted from the original spectra.<sup>10,11,12</sup> A least-squares method was then used to fit the spectra to a series of Voigt functions. The Gaussian/Lorentzian ratio of the lineshape was allowed to float but was constrained to be the same for all peaks in a given spectrum. The experimental linewidth was not measured independently, but was estimated as  $\approx 0.32$  eV based on the photon resolution and detector resolution. States with short core-hole lifetimes will yield significantly broader, predominantly Lorentzian linewidths, whereas those with significantly narrower inherent linewidths will appear predominantly with a

Gaussian lineshape. The lineshapes of the As native-oxide peaks were ~90% Gaussian, while As lineshapes for the Cl-terminated (111)A surface were >99% Gaussian. These results are consistent with significant broadening of the inherent Lorentzian lineshape of the As oxide peaks.<sup>13</sup>

In accord with reported procedures, the As 3d spectra were fitted to a series of doublets to account for the 3d<sub>5/2</sub> and 3d<sub>3/2</sub> spin-orbit components of each peak. The peaks that comprised each doublet were mutually constrained to have the same peak width, to be separated by  $0.7 \pm 0.01$  eV, and to have an area ratio of  $(1:0.667) \pm 0.01$ .<sup>14</sup> A similar procedure was used for the Ga peaks, except that the energy separation between the 3d<sub>5/2</sub> and 3d<sub>3/2</sub> peaks was set to  $(0.44 \pm 0.01)$  eV.<sup>14</sup> Binding energies for all spectra were referenced to the As 3d<sub>5/2</sub> peak of GaAs, whose binding energy was taken to be 41.1 eV.

Equivalent monolayer coverages of surface species were calculated from a substrate-overlayer relation used previously for Si:<sup>15</sup>

$$\frac{I_{el,surf}}{I_{el,bulk}} = \frac{n_{el,surf}}{n_{el,bulk} l_{el} - n_{el,surf}} \quad (2.5)$$

where  $I_{el,surf}$  and  $I_{el,bulk}$  are the integrated intensity of the surface and bulk signals for a given element,  $n_{el,surf}$  and  $n_{el,bulk}$  are the number density of the surface and bulk species of that element. The penetration depth  $l_{el}$  is defined as:

$$l_{el} = \lambda_{el} \sin \theta \quad (2.6)$$

where  $\lambda$  is the mean free path from eq (2.4). The photoelectron take-off angle  $\theta$  for all results reported here was 90°, so  $l_{el} = \lambda_{el}$ . This measure of surface coverage is independent of instrument sensitivity factors. However, it includes the implicit assumption that there are only negligible difference between surface and bulk photoionization cross-sections, and does not allow comparison between Ga and As

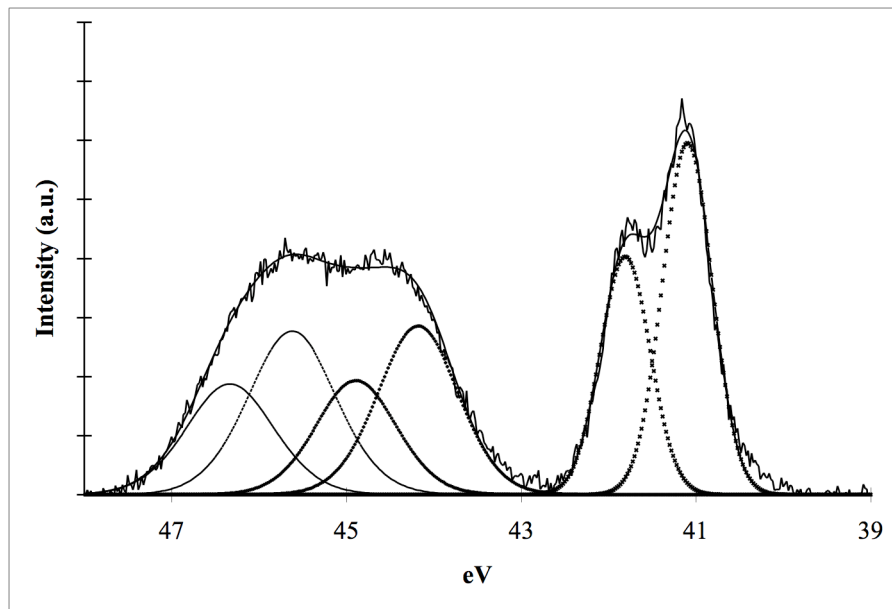
species. Further, experiments on the (111) faces of a III-V semiconductor will probe alternating layers of Ga and As (figure 1.3), while the bulk number density term assumes an even distribution of atoms in the sample depth. It is not known what distortions these effects will introduce in a experiment with such a small sample depth, and this model has not, to my knowledge, previously been applied to a compound semiconductor. However, it should yield consistent results between experiments, and allow comparison of coverages between the different surfaces in this study.

### 2.3 Results and Discussion

Figure 2.1a shows the SXPS data for the As 3d region prior to etching and Cl-termination of the GaAs surface. In addition to the energy-resolved spin-orbit doublet arising at 41.1 eV from the lattice As atoms of the bulk GaAs crystal, broader emissions were observed at 44.2 and 45.6 eV. These latter two peaks are assigned to  $\text{As}_2\text{O}_3$  and  $\text{As}_2\text{O}_5$ , respectively.<sup>16</sup> The SXPS spectrum of the Ga 3d region (Figure 2.1b) showed a broad oxide peak at 20.81 eV that can be assigned to  $\text{Ga}_2\text{O}_3$ .<sup>16</sup> The broader feature at lower binding energy was fitted by peaks at 19.38 eV and 20.24 eV, representing the bulk GaAs and  $\text{Ga}_2\text{O}$  signals, respectively. The coverage of the mixed oxide overlayer corresponded to  $1.63 \pm 0.25$  equivalent monolayers.

Treating such oxidized GaAs(111)A surfaces in 6 M HCl(aq) for times as short as 5 min has been reported to form Cl-terminated GaAs(111)A surfaces.<sup>1,2</sup> While etching for 5 min did remove all of the  $\text{As}_2\text{O}_3$  from the surface, a significant amount of arsenic oxide was still detectable using the very surface-sensitive SXPS method (Figure 2.2a), and an observable amount was still present after 15 min. Figure 2b depicts the As 3d

a



b

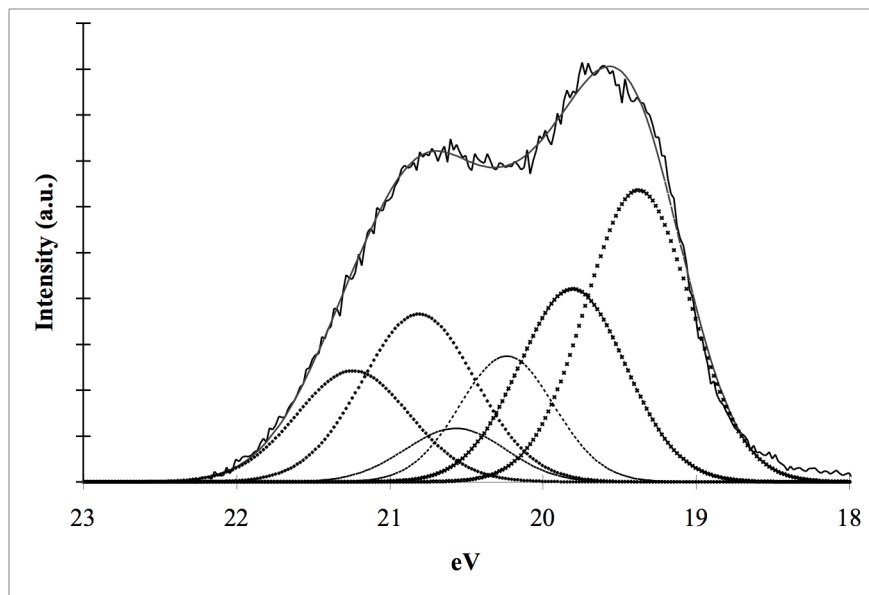
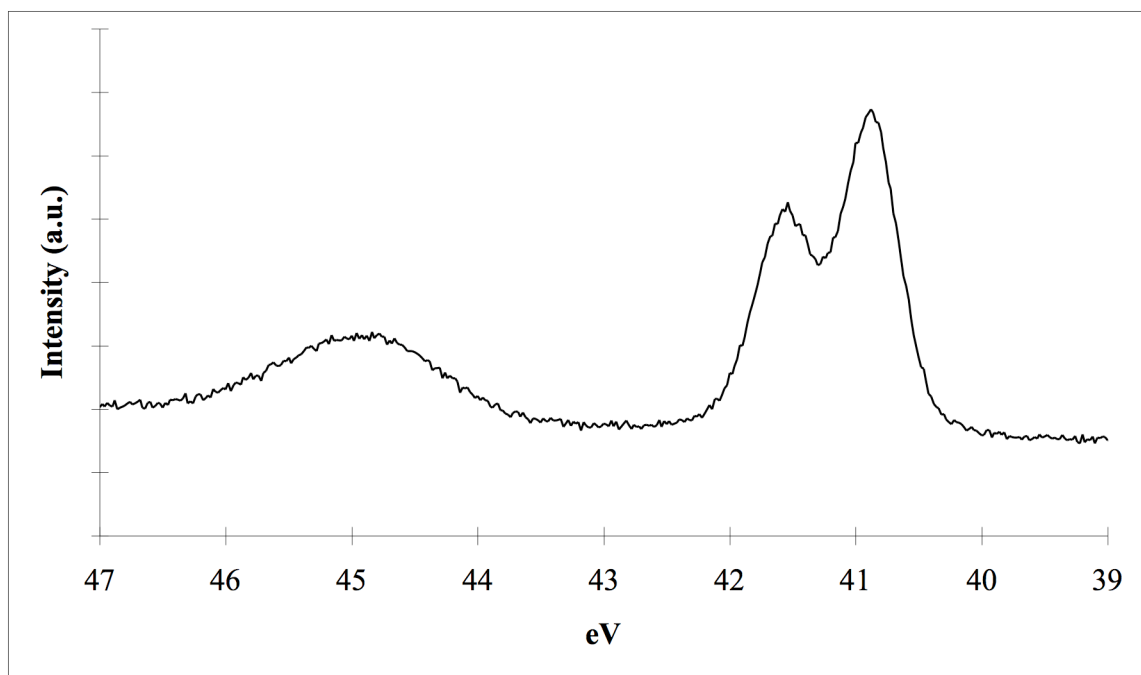


**Figure 2.1:** : SXPS spectra (solid line) and Voigt function fits of the native oxide for a—the As 3d region and b—the Ga 3d region. Each Voigt function fit includes both the  $d_{5/2}$  and  $d_{3/2}$  components. Reported binding energy values are for the  $d_{5/2}$  components of the fit.

a



b

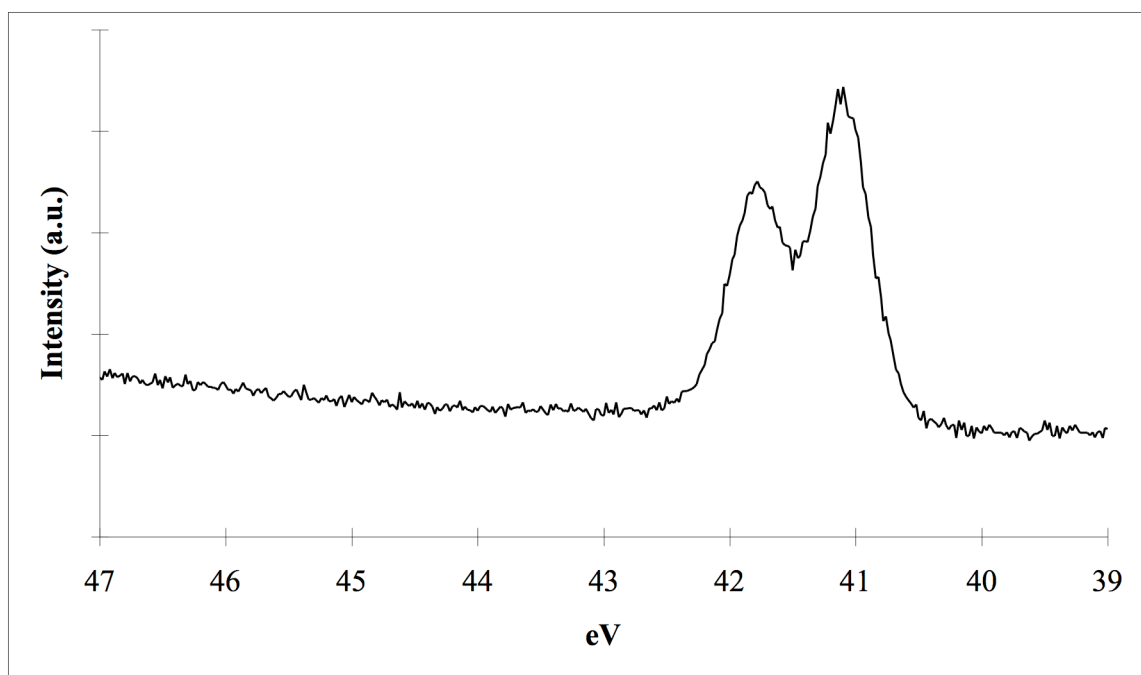


**Figure 2.2:** : SXPS data for the HCl(aq) treated surfaces. a—The As 3d region after 5 minutes in the HCl solution; b—The As 3d region after 30 min in the HCl solution.

SXPS data for the GaAs(111)A surface after a 30 min exposure to the HCl(aq) solution, with no detectable oxide signals to within the sensitivity of the SXPS instrumentation.

Because a better Shirley background was obtained by omitting large regions that did not have any peaks, for this surface only the region known to contain the bulk GaAs and As<sup>0</sup> (41.8 eV) peaks was fitted. After subtraction of the Shirley background from this spectrum, the doublet-peak was well fitted by a single Voigt function (figure 2.3). Within the detection limits of the experiment, no elemental As was observed. As As<sup>0</sup> is a potentially important trap state for carrier recombination, its absence is an important characteristic for the chemical preparation of surfaces having desirable electronic properties.

XPS survey scans of Cl-terminated GaAs(111)A surfaces showed the expected series of photoemission and Auger peaks arising from Ga and As (figure 2.4a). Small O 1s (531.2 eV) and C 1s (284.6 eV) peaks were also observed, indicating a small amount of physisorbed contamination. The Cl 2p (199.5 eV) peak was difficult to observe in the survey scan, due to its proximity to the As 3s (204.7 eV) signal,<sup>17</sup> but the Cl 2p peak could be readily seen in a higher resolution scan of the immediate area around 200 eV. (Figure 2.4b) The Cl 2p<sub>3/2</sub> and Cl 2p<sub>1/2</sub> signals were also resolved from each other in this higher resolution scan. Application of the substrate/overlayer model described in eq. 2.2 yielded a Cl coverage of  $0.85 \pm 0.07$  equivalent monolayers. No Ga or As oxides were present in detailed scans of their respective 3d regions, indicating that the O 1s signal is primarily due to the observed Ga(OH)<sub>3</sub> and physisorbed H<sub>2</sub>O.

Etching with 6 M HCl(aq) for 30 min also led to the complete disappearance of the Ga 3d oxide signal and the appearance of a small, broad signal at 21.68 eV, i.e.,

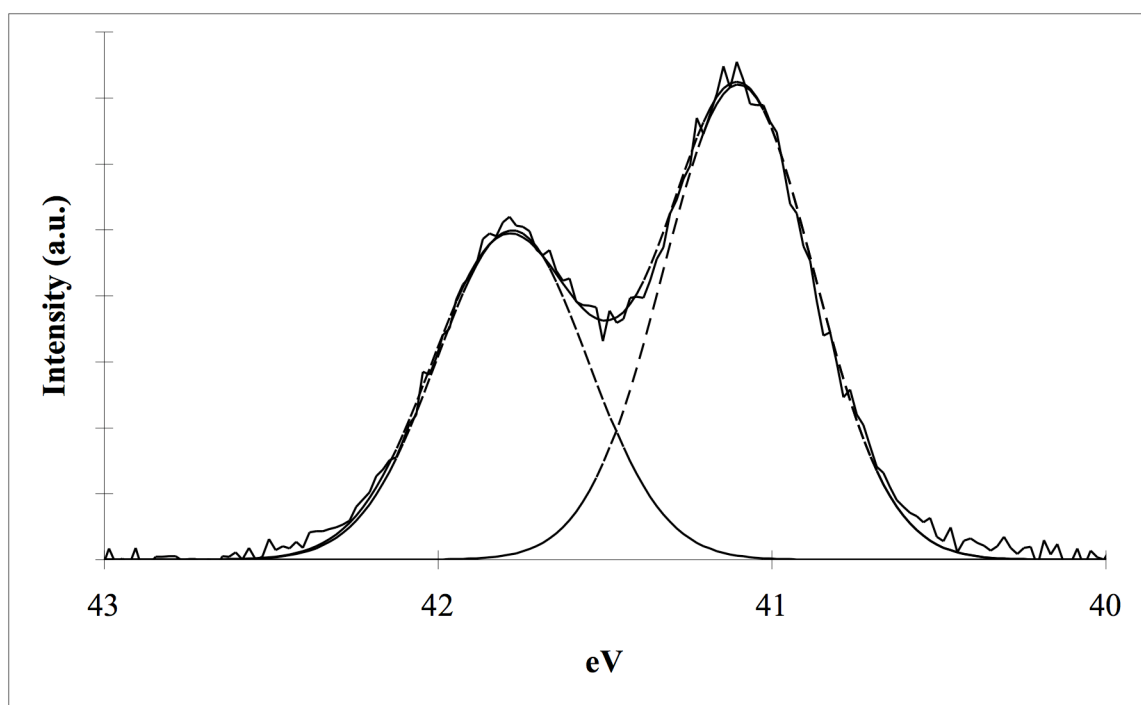
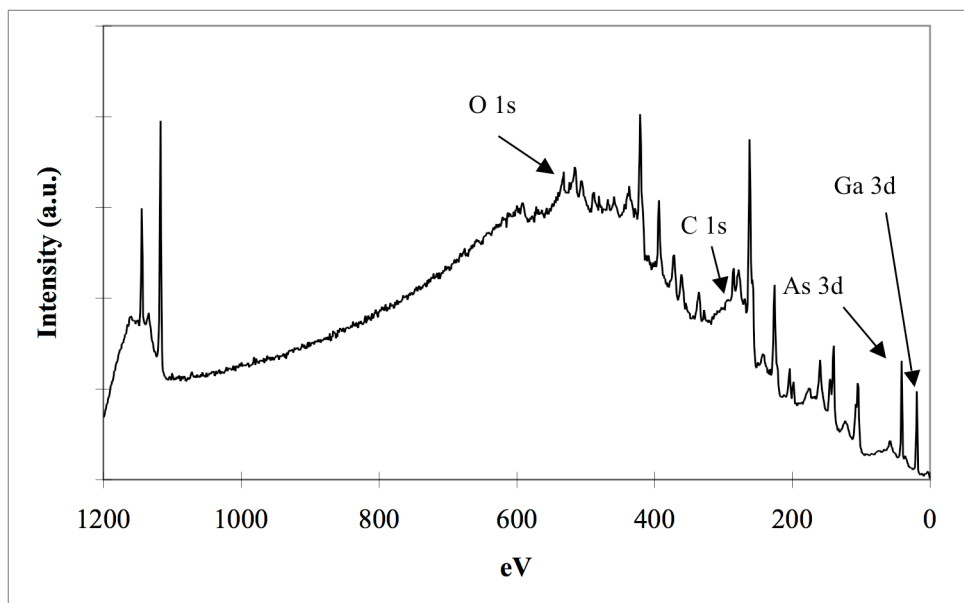


**Figure 2.3:** SXPS data (solid line) and calculated fits for the As 3d spectrum of the Cl-terminated surface. No components besides the bulk could be detected.

a



b

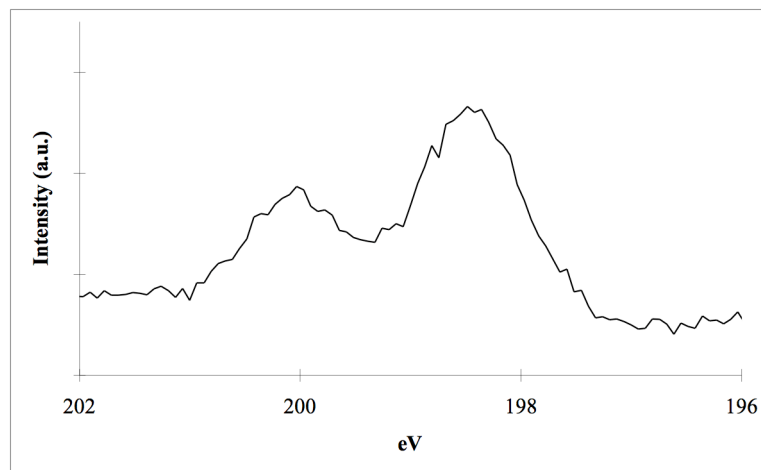


**Figure 2.4:** Al K $\alpha$  X-ray photoelectron spectra of the Cl-terminated GaAs(111)A

surface prepared by a 30 min treatment in HCl (aq). a—Survey scan from 1 to 1200 eV.

The Ga 3d, As 3d, C 1s and O 1s peaks are labeled. The Cl 2p peak is difficult to discern in the survey scan because of its close proximity to the As 3s peak at 204.7 eV. All other peaks are due to Ga and As photoelectron and Auger peaks.;

b—Detailed scan of the Cl 2p region, showing the Cl 2p<sub>3/2</sub> and 2p<sub>1/2</sub> peaks.

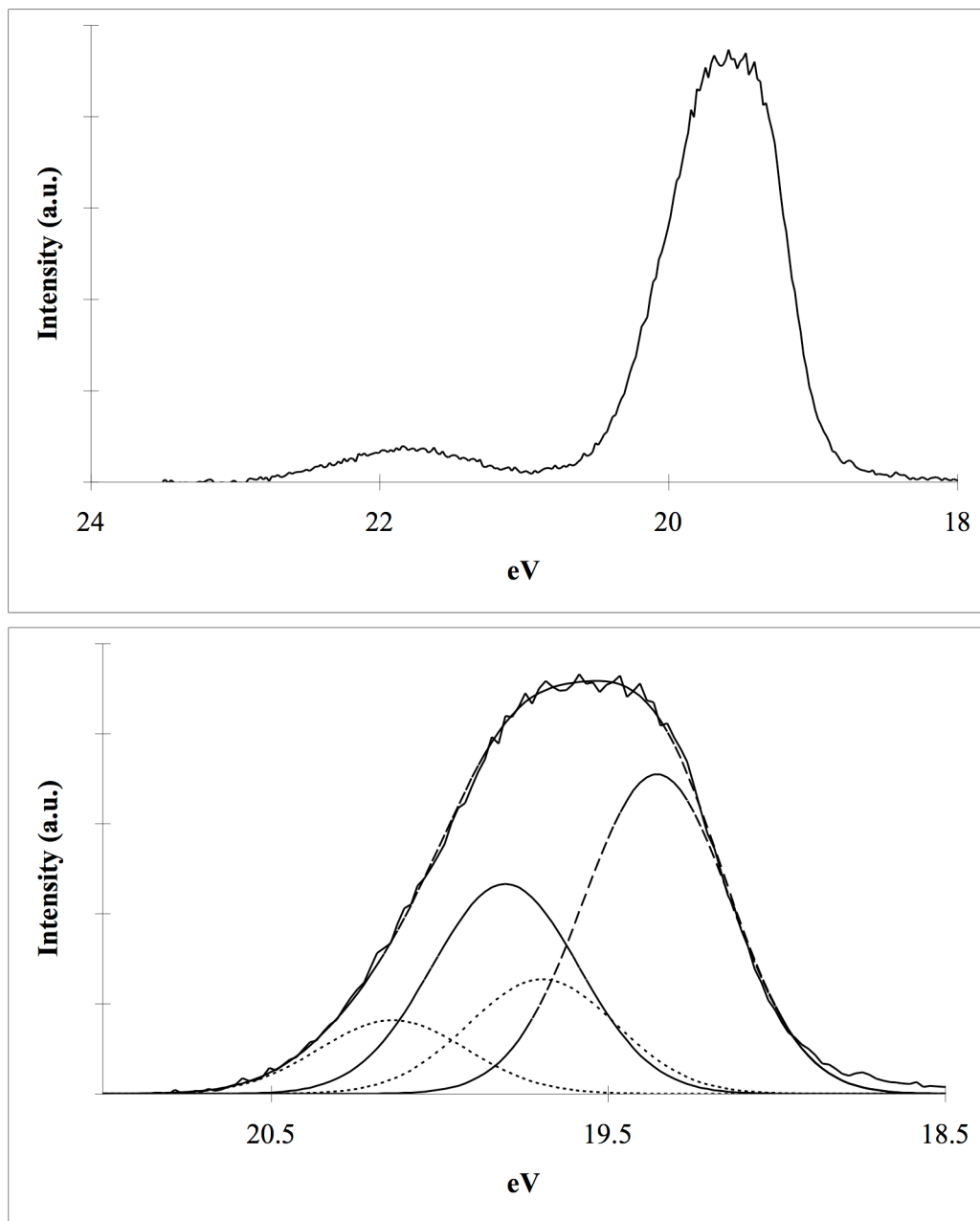


**Figure 2.5:** SXPS spectra of the Ga 3d region of the (111)A surface after 30 minutes in the HCl solution. a—Raw data after Shirley background subtraction. The aqueous treatment has introduced a new peak at higher binding energy than the native oxides. b—SXPS data (solid line) and Voigt function fits (dashed lines) of the bulk and Cl-bonded surface Ga species.

2.3 eV higher in binding energy than the Ga 3d signal in bulk GaAs (figure 2.5a). The peak is not due to GaAsO<sub>4</sub>, given the lack of a corresponding As signal 4.1 eV higher binding energy than the bulk (Ga)As peak (Figure 2.2b). The formation of Ga hydroxides has been observed during etching of GaAs in aqueous solutions.<sup>16</sup> Thus, this peak is assigned to Ga(OH)<sub>3</sub>.

The remainder of the Ga 3d region was well fitted using two peaks, one arising from the bulk signal at 19.36 eV, and the second emission at 19.70 eV (figure 2.4b). No Ga<sub>2</sub>O or Ga<sub>2</sub>O<sub>3</sub> signals were evident in the spectrum. The feature at 19.70 eV is assigned to Cl-bonded Ga on the GaAs(111)A surface. The lower binding energy of this peak relative to the binding energy of the Ga 3d emission from Ga<sub>2</sub>O, is consistent with expectations based on the smaller electronegativity of Cl relative to O. For comparison, the energy difference between the 2p photoelectron peaks of a Si<sup>+</sup> bonded to O vs. a Si<sup>+</sup> bonded to Cl is 0.2 eV.<sup>18</sup> Assuming that the photoemission cross sections from surface and bulk Ga atoms are the same, the ratios of the Ga peaks relative to the bulk Ga signal, in conjunction with the 0.52 nm escape depth of the Ga photoelectrons at ≈71 eV kinetic energy, yields a surface coverage of 0.37 monolayers for the Ga-Cl surface species and 0.12 monolayers for Ga(OH)<sub>3</sub>. This is a significant discrepancy from the overlayer coverage calculated with standard XPS measurements. Because the standard XPS probes further into the bulk sample, assumptions about averages through the bulk material should be more robust. Thus, these discrepancies suggest that the substrate-overlayer equations developed for elemental materials tend to underestimate surface coverages for compound semiconductors, at least for the case of polar (111) surfaces. Equivalent

monolayer coverages calculated by this method should therefore be taken only as lower bounds on actual surface coverage.

It is also possible that the  $\text{Ga}(\text{OH})_3$  peak is a contaminant on top of the Ga-Cl surface species, but definitive evaluations of the spatial distribution of these species cannot be made from the available SXPS data. Regardless, it is clear that the etching of GaAs(111)A for 30 min in 6 M HCl(aq) produces a well-defined Cl-terminated GaAs surface free of detectable elemental As and free of essentially all As and Ga oxides. Assignment of the peaks in this spectrum will aid in the characterization of surfaces formed by subsequent functionalization reactions.<sup>19</sup>

## 2.4 Conclusions

The photoelectron spectra of Cl-terminated GaAs(111)A have been measured using conventional and soft X-ray photoelectron spectroscopy. After treatment with 6 M HCl(aq) the presence of Cl atoms has been confirmed on the GaAs(111)A surface, and a binding energy of 19.70 eV, i.e., a shift of 0.34 eV from the bulk value, has been assigned to surface Ga atoms bonded to Cl. A 30 min treatment of the GaAs(111)A surface in 6 M HCl(aq) has been shown to yield a surface with a monolayer of Cl while surfaces treated for only 5 min showed a significant amount of  $\text{As}_2\text{O}_3$ . The spectra also indicated that the surfaces were free of  $\text{As}^0$ , to within the resolution of the SXPS experiment, suggesting that surfaces prepared by this method could provide an excellent platform for subsequent, well-defined, wet chemical functionalization reactions.

## 2.5 Acknowledgements

I acknowledge the Department of Energy, Office of Basic Energy Sciences, for support of this work. The research was carried out in part at the National Synchrotron Light Source, Brookhaven National Laboratory, which is supported by the U.S. Department of Energy, Division of Materials Sciences and Division of Chemical Sciences, under Contract No. DE-AC02-98CH10886. I thank Michael Sullivan for use of the N<sub>2</sub>(g)-purged glove box at the NSLS.

**References**

- (1) Lu, Z. H.; Chatenoud, F.; Dion, M. M.; Graham, M. J.; Ruda, H. E.; Koutzarov, I.; Liu, Q.; Mitchell, C. E. J.; Hill, I. G.; McLean, A. B. *Applied Physics Letters* **1995**, *67*, 670.
- (2) Lu, Z. H.; Tyliczszak, T.; Hitchcock, A. P. *Physical Review B* **1998**, *58*, 13820.
- (3) Bansal, A.; Li, X. L.; Yi, S. I.; Weinberg, W. H.; Lewis, N. S. *Journal of Physical Chemistry B* **2001**, *105*, 10266.
- (4) Webb, L. J.; Lewis, N. S. *Journal of Physical Chemistry B* **2003**, *107*, 5404.
- (5) Haber, J. A.; Lewis, N. S. *Journal of Physical Chemistry B* **2002**, *106*, 3639.
- (6) Scofield, J. H. *Journal of Electron Spectroscopy and Related Phenomena* **1976**, *8*, 129.
- (7) Keister, J. W.; Rowe, J. E.; Kolodziej, J. J.; Niimi, H.; Tao, H. S.; Madey, T. E.; Lucovsky, G. *Journal of Vacuum Science & Technology A—Vacuum Surfaces and Films* **1999**, *17*, 1250.
- (8) Seah, M. P. Quantification of AES and XPS. In *Practical Surface Analysis*; 2nd ed.; Briggs, D., Seah, M. P., eds.; John Wiley & Sons: Chichester, 1990; vol. 1; pp 201.
- (9) Sze, S. M. *The Physics of Semiconductor Devices*, 2nd. ed. ed.; John Wiley & Sons: New York, 1981.
- (10) Proctor, A.; Sherwood, P. M. A. *Analytical Chemistry* **1982**, *54*, 13.

- (11) Shirley, D. A. *Physical Review B* **1972**, *5*, 4709.
- (12) Contini, G.; Turchini, S. *Computer Physics Communications* **1996**, *94*, 49.
- (13) Liu, Z. F.; Bancroft, G. M.; Cutler, J. N.; Sutherland, D. G.; Tan, K. H.; Tse, J. S.; Cavell, R. G. *Physical Review A* **1992**, *46*, 1688.
- (14) Eastman, D. E.; Chiang, T. C.; Heimann, P.; Himpsel, F. J. *Physical Review Letters* **1980**, *45*, 656.
- (15) Himpsel, F. J.; McFeely, F. R.; Talebibrabimi, A.; Yarmoff, J. A.; Hollinger, G. *Physical Review B* **1988**, *38*, 6084.
- (16) Surdu-Bob, C. C.; Saied, S. O.; Sullivan, J. L. *Applied Surface Science* **2001**, *183*, 126.
- (17) Shalvoy, R. B.; Fisher, G. B.; Stiles, P. J. *Physical Review B* **1977**, *15*, 1680.
- (18) Webb, L. J.; Nemanick, E. J.; Biteen, J. S.; Knapp, D. W.; Michalak, D. J.; Traub, M. C.; Chan, A. S. Y.; Brunschwig, B. S.; Lewis, N. S. *Journal of Physical Chemistry B* **2005**, *109*, 3930.
- (19) Traub, M. C.; Biteen, J. S.; Michalak, D. J.; Webb, L. J.; Lewis, N. S. *Journal of Physical Chemistry C*, **2007**, To be submitted

## Chapter 3

# Phosphine Functionalization of GaAs(111)A

### 3.1 Introduction

Chemical functionalization of semiconductor surfaces has many important potential applications, including protecting surfaces from oxidation and degradation<sup>1</sup> or wiring the semiconductors to molecular electronic components.<sup>2</sup> The formation of the Cl-terminated GaAs(111)A surface by wet chemical means was first described by Lu and co-workers.<sup>3,4</sup> The chemical composition of this surface has been described in the previous chapter. Due to its ease of preparation and high purity, this surface presents a potentially valuable platform for further functionalization reactions. In this chapter, the reactivity of this surface towards phosphines and the chemical and electronic behavior of phosphine functionalized surfaces is described.

Phosphines present a promising candidate for novel GaAs passivation chemistry for several reasons. Phosphines contain a reactive electron lone pair on their central phosphorus atom, making them good donors for bonding atop Ga sites on the GaAs(111)A surface. GaP is a wider band-gap (2.26 eV) semiconductor than GaAs, suggesting greater stability for Ga-P  $\sigma$  bonds. Trioctylphosphine has been used

as a passivating agent for the surfaces of II-VI nanocrystals with relatively high photoluminescence yields compared to other organic capping groups,<sup>5</sup> and phosphine plasma has been explored as passivating agent for InGaAs.<sup>6</sup> This suggests an ability to effectively donate electron density to nucleophilic Ga surface sites. Given the success of passivation based on electron-rich sulfur<sup>7</sup> and nitrogen<sup>8</sup> moieties, phosphines seemed a natural complement to known GaAs surface chemistry.

Two phosphines were chosen for reactions with the Cl-terminated surface, triethylphosphine (PEt<sub>3</sub>) and trichlorophosphine (PCl<sub>3</sub>). Both of these compounds are liquids at room temperature and are well suited to solution functionalization reactions. While these groups are too large for packing atop every Ga site on the (111)A surface, they are significantly smaller than more sterically constrained groups such as trioctylphosphine, and a higher percentage of surface sites should be capped. These two surface groups provide an interesting contrast in reactivity, as the Cl groups on PCl<sub>3</sub> are relatively labile and easy to displace, allowing a variety of reactions and binding modes. The ethyl groups on PEt<sub>3</sub> are relatively unreactive, and only reactions through the P lone pair should be possible. Finally, because PCl<sub>3</sub> is highly reactive, it may remove surface contaminants introduced after etching, and allow direct reactions between PCl<sub>3</sub> and oxide-terminated GaAs without an etching step.

The results of surface functionalization reactions have been evaluated primarily by XPS. Both standard Al K $\alpha$  and soft X-ray synchrotron sources were used to provide a complete picture of both phosphorus on the surface and the oxidation states of Ga and As surface sites, as described in the previous chapter. In addition to this chemical data, steady-state photoluminescence (PL) intensity measurements were used to evaluate the

effect of surface passivation on surface state density. These experiments do not provide values for the surface recombination velocity ( $S$ ) or surface trap density ( $N_{TS}$ ), but do provide qualitative information on the electronic effects of the surface chemistry.

A quantitative value for the surface recombination velocity ( $S$ ) in an undoped sample can be obtained from the decay in excess carriers by the equation:<sup>9</sup>

$$\frac{dn}{dt} = - \left[ \frac{1}{\tau_b} + \frac{S_1 + S_2}{L} \right] n \quad (3.1)$$

where  $\tau_b$  is the bulk lifetime,  $L$  is the thickness of the sample,  $n$  is the excess carrier concentration, and  $S_1$  and  $S_2$  are the surface recombination velocities at the front and rear face of the sample. In order to maximize the surface contribution to this decay, measurements are typically made on thin epitaxial layers of GaAs capped on both sides with  $\text{Al}_{0.5}\text{Ga}_{0.5}\text{As}$ . The front face is then selectively etched away with aqueous fluoride ion solutions and treated to yield the interface of interest. For these samples,  $L \approx 1 \mu\text{m}$  and  $S_2 = 450 \text{ cm s}^{-1}$ , so that the primary contribution to carrier decay is recombination at the front face.<sup>10</sup>

Because such epitaxially layered samples are extremely expensive and difficult to obtain, a simpler steady-state methodology is widely used to evaluate single crystal surfaces.<sup>8,11</sup> Just as recombination through surface states will decrease the overall lifetime of a sample, both radiative and non-radiative steady-state quenching through surface traps will decrease the intensity of band-gap PL (figure 3.1). In particular, Cl-termination of the GaAs(111)A face has been reported to yield a factor of 2 increase in the PL intensity relative to the native oxide,<sup>3</sup> while passivation of the (100) surface with  $\text{N}_2\text{H}_4$  followed by annealing yielded a factor of 8 increase.<sup>8</sup> These improvements are not

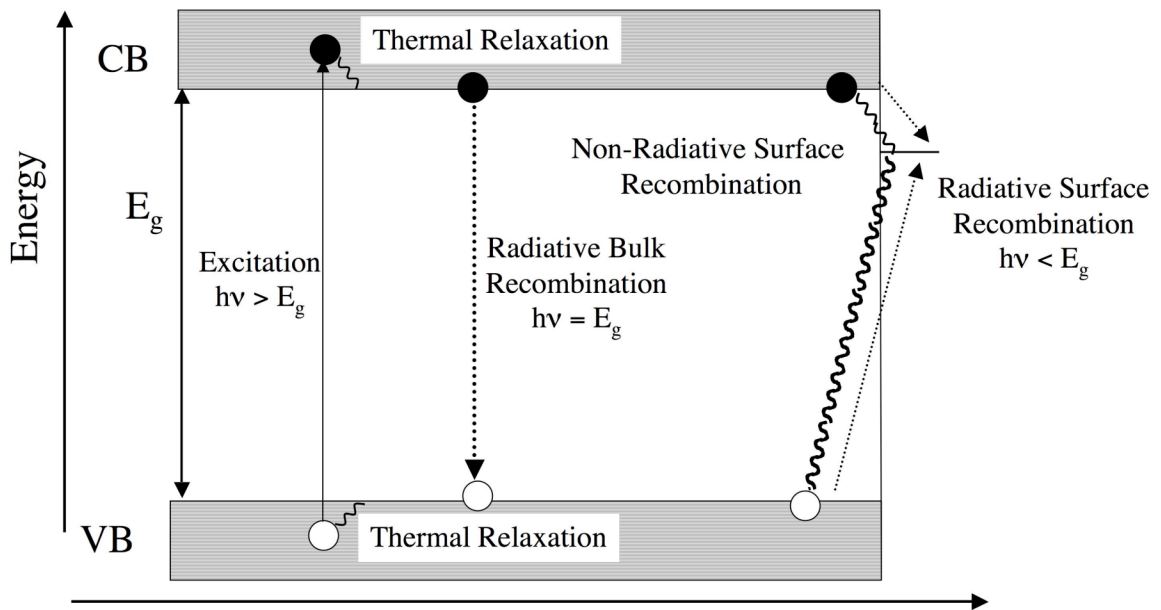


**Figure 3.1.** Recombination mechanisms in bulk GaAs. Recombination through surface traps competes with bulk recombination and quenches the intensity of emission photons with energy  $E_g$ .

as dramatic as the order of magnitude changes that surface passivation induces in  $S$ , but are easily measurable with standard single crystal wafers.

## 3.2 Experimental Procedures

### 3.2.1 Materials and Methods

For XPS experiments, n-GaAs(111) wafers polished on the (111)A face to 325  $\mu\text{m}$  were acquired from AXT (Fremont, CA). They were doped with Si to a carrier concentration of  $1.7 \times 10^{18} \text{ cm}^{-3}$ . Photoluminescence experiments were performed on undoped GaAs(111) wafers acquired from Atomergic (Farmingdale, NY). All solvents and chemicals for the surface functionalization reactions were used as received from Aldrich Chemical Corporation. Nanopure  $\text{H}_2\text{O}$  with a resistivity  $>17.8 \text{ M}\Omega \text{ cm}$  was used at all times.

Prior to performing any surface chemistry, all samples were cleaned and degreased by successive rinses in  $\text{H}_2\text{O}$ ,  $\text{CH}_3\text{OH}$ , acetone, 1,1,1-trichloroethane (TCE), acetone,  $\text{CH}_3\text{OH}$ , and  $\text{H}_2\text{O}$ . Samples were then etched in 1:1 mixture of concentrated  $\text{HCl}:\text{H}_2\text{O}$  at room temperature for 30 minutes, dried under a stream of  $\text{N}_2$  without a water rinse and placed into the antechamber of a  $\text{N}_2(\text{g})$ -purged glove box for further chemical functionalization. Functionalization reactions were performed by immersing the samples in neat  $\text{PCl}_3$  (Aldrich) or a 1.0 M solution of  $\text{PEt}_3$  in THF (Aldrich). For selected experiments, samples were introduced into the glovebox antechamber without etching in  $\text{HCl}$ . All reactions were conducted for 3 hours at ambient temperature. Samples were then removed from solution, rinsed with anhydrous THF (Aldrich), and dried under a stream of  $\text{N}_2$ .

### 3.2.2 Instrumentation

#### 3.2.2.1 XPS Measurements

Photoelectron spectra were collected and analyzed using the procedures described in section 2.2.2. Phosphine functionalized samples at Caltech were introduced to the antechamber of the XPS directly from the inert atmosphere glove box without any exposure to ambient air. Samples for SXPS measurements were functionalized in a glove box, then transported in vials sealed under inert atmosphere to beamline U4A and loaded into the SXPS antechamber, leaving them exposed to ambient air for several minutes after functionalization.

#### 3.2.2.2 Photoluminescence Measurements

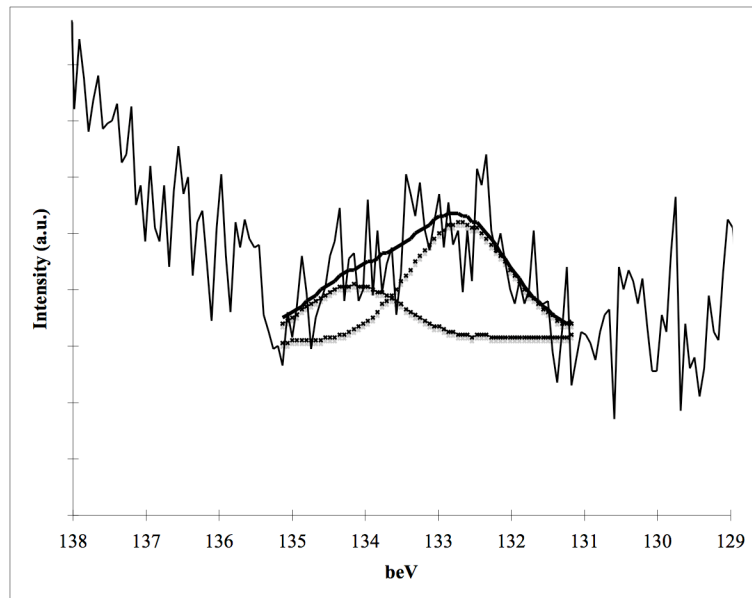
Samples were mounted vertically and illuminated on the front face with the 442 nm line of a continuous wavelength HeCd laser, operating at 30 mW. Photoluminescence was collected from the front face and focused through a monochromator into a dry-ice-cooled photomultiplier tube detector (Hamamatsu R632-01), which was connected to a chart recorder. Scattered laser light was filtered out using a long-pass filter with a cutoff wavelength of 845 nm. Peak intensities were evaluated based on the signal at 874 nm.

## 3.3 Results

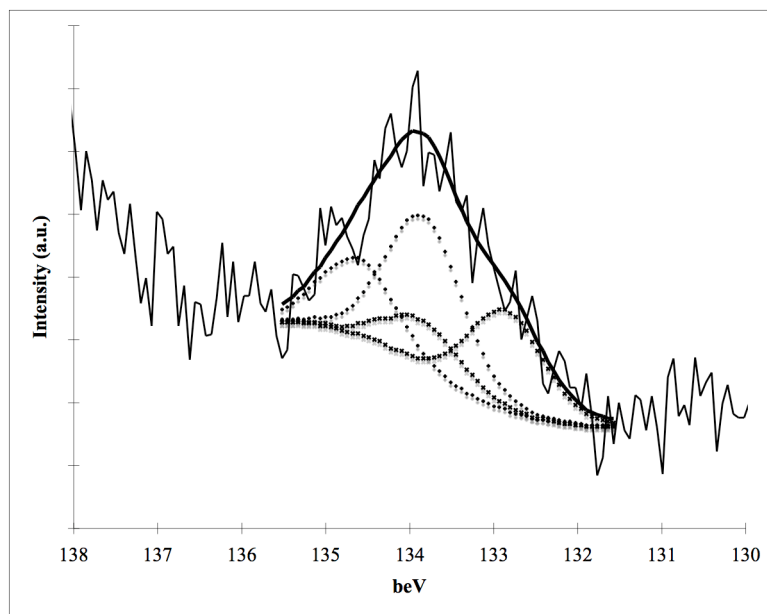
### 3.3.1 Reactions of $\text{PEt}_3$ and $\text{PCl}_3$ on Cl-Terminated GaAs(111)A

Figure 3.2a shows the P 2p region of a typical XPS spectrum of Cl-terminated surface immediately following treatment with  $\text{PEt}_3$ . The binding energy of the P 2p<sub>3/2</sub> component of this doublet was  $132.8 \pm 0.06$  eV. Equivalent monolayer (ML) coverages

a



b



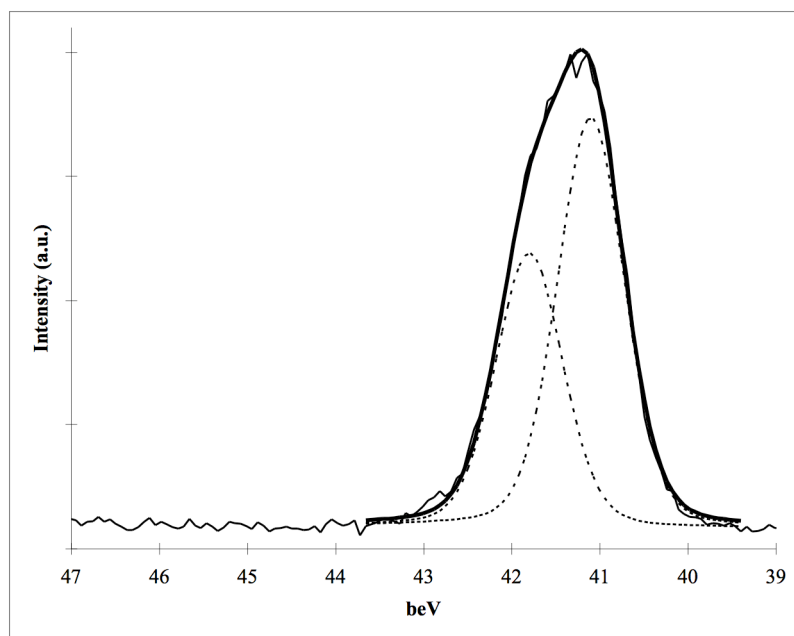
**Figure 3.2.** a—XPS data for the  $\text{PET}_3$  functionalized surfaces containing only one P species; b—XPS data for the  $\text{PET}_3$  functionalized surfaces containing two separate P species, one with the same binding energy as in a (x symbols) and one shifted higher binding energy (+ symbols)

were calculated based on the P 2p and Ga 3d photoelectron peaks, both measured on the Caltech XPS. Using eq 2.3, the atomic size of P was calculated as 0.304 nm. By using this value and the bulk density of P ( $1.823 \text{ g cm}^{-3}$ ), the surface coverage of these two treatments can be quantitatively determined using eq 2.2. For  $\text{PEt}_3$  treated surfaces, the P coverage was  $0.38 \pm 0.11 \text{ ML}$ , a value consistent with measurements of sterically constrained groups on the Si(111) surface.<sup>12</sup> Additionally, measurements were made on the Cl 2p peak, which was still present on the surface after treatment of  $\text{PEt}_3$ . Integrating the areas of the P  $2p_{3/2}$  and Cl 2p peaks and correcting for their relative sensitivity factors (0.789 and 2.285) yields a P:Cl ratio of 0.38. Together, these data suggest that  $\text{PEt}_3$  occupies  $\approx 30\text{--}50\%$  of Ga surface sites, with the remaining sites terminated by Cl atoms.

It should be noted that on some samples, the P 2p peak was best fit by 2 spin-orbit doublets, representing distinct chemical species on the surface (figure 3.2b). In these instances, the lower binding energy peak displayed binding energies, P:Cl ratios and surface coverages consistent with those described above. The  $2p_{3/2}$  component of the second peak was centered at 133.8 eV, and was typically more intense, sometimes exhibiting surface coverages greater than 1 equivalent monolayer. This higher binding energy implies that oxidation of the P atom can be attributed to physisorption of an insoluble, oxidized phosphine species.

Measurements of Ga and As 3d photoelectron peaks on the Caltech XPS appeared identical to those on the Cl-terminated surface (figure 3.3). The Ga 3d region was fit to a single peak representing bulk Ga(As), while the As 3d region was fit to a single spin-orbit doublet representing bulk (Ga)As. Both regions were completely free of oxides and other contaminants to within the resolution of this experiment. To obtain data on these peaks

a



b

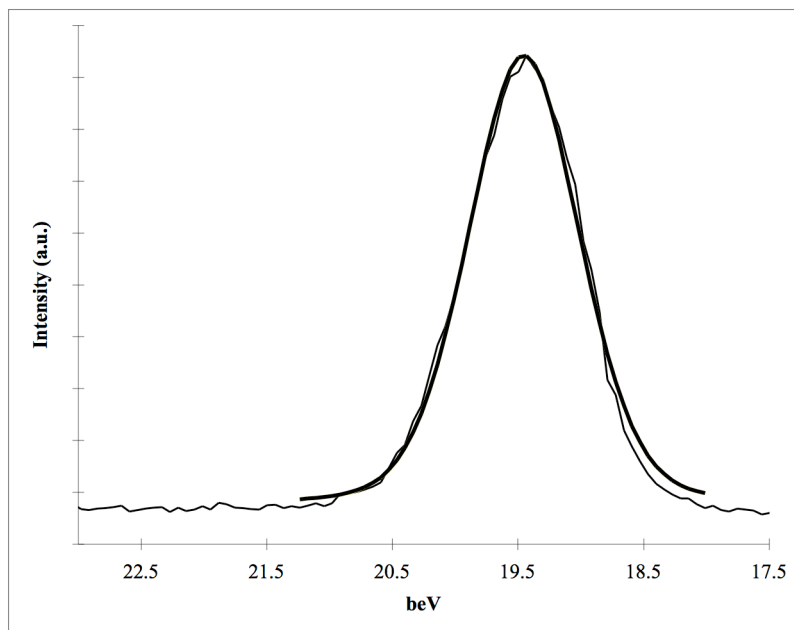


**Figure 3.3.** The XPS spectra of As 3d (a) and Ga 3d (b) on  $\text{PET}_3$  functionalized GaAs(111)A. The Ga 3d peak is fit to a single peak, while the As 3d peak is fit to a single spin-orbit doublet with  $3d_{5/2}$  and  $3d_{3/2}$  components.

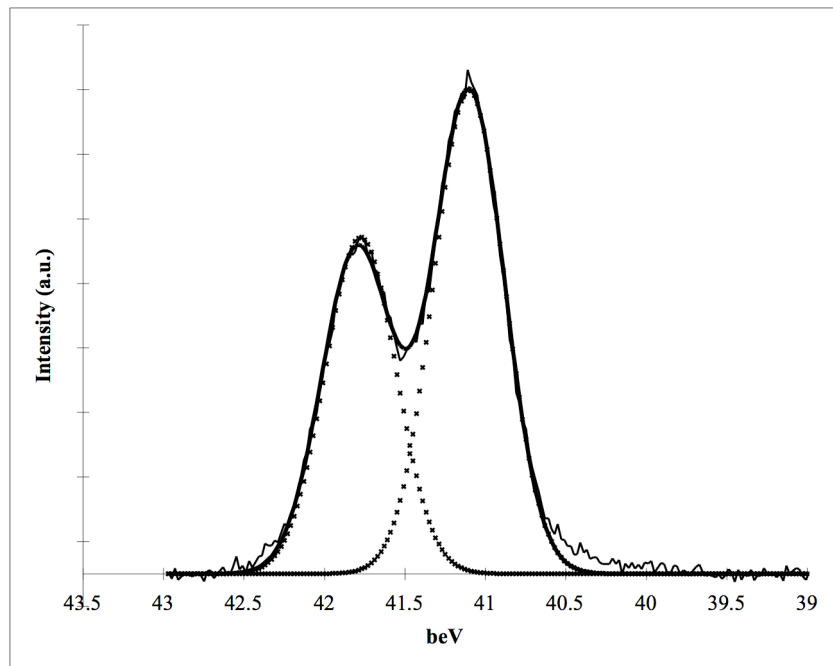
with greater surface sensitivity and resolution, soft X-ray photoelectron spectra of these surfaces were collected at Brookhaven National Laboratory.

The high-resolution As 3d spectrum of  $\text{PEt}_3$  functionalized surfaces was well fit by a single spin-orbit doublet (figure 3.4a). A small amount of  $\text{As}_2\text{O}_3$  was observed in the spectrum of the  $\text{PEt}_3$  treated surfaces (figure 3.4b). This peak was too small and broad to obtain a reliable Shirley background or make a quantitative evaluation of surface coverage.

In contrast to this relatively simple As spectrum, the high-resolution Ga 3d spectrum of these surfaces appeared to consist of multiple peaks. Because the binding energies of the relevant chemical species are more closely spaced for Ga 3d than for As 3d,<sup>13</sup> and the spacing between the spin-orbit doublet peaks is significantly smaller (0.44 eV vs. 0.70 eV),<sup>14</sup> it is difficult to resolve more than two chemical species in these peaks. To simplify the fitting procedure, the Ga  $3d_{3/2}$  peaks were deconvoluted from these spectra. For the purposes of this deconvolution, the height ratio and binding energy difference of the  $\text{Ga}_{5/2}$  and  $\text{Ga}_{3/2}$  peaks were fixed at the 0.667 and 0.44 eV respectively. Further, the fits obtained for these spectra depended strongly on the peak width constraints. Peak widths were therefore constrained to  $\pm 10\%$  of the value observed for the bulk Ga(As)  $3d_{5/2}$  peak on the Cl-terminated surface.

The deconvoluted Ga 3d spectra of the  $\text{PEt}_3$  functionalized surface was well fit by 4 Voigt function peaks (figure 3.5). The second peak in the spectrum is shifted 0.35 eV to higher binding energy relative to the lowest energy bulk peak, consistent with the shift observed for Cl-bonded Ga surface sites. The next peak in the spectrum was shifted to 0.92 eV to higher binding energy than the bulk peak, consistent with the 0.86 eV shift

a



b

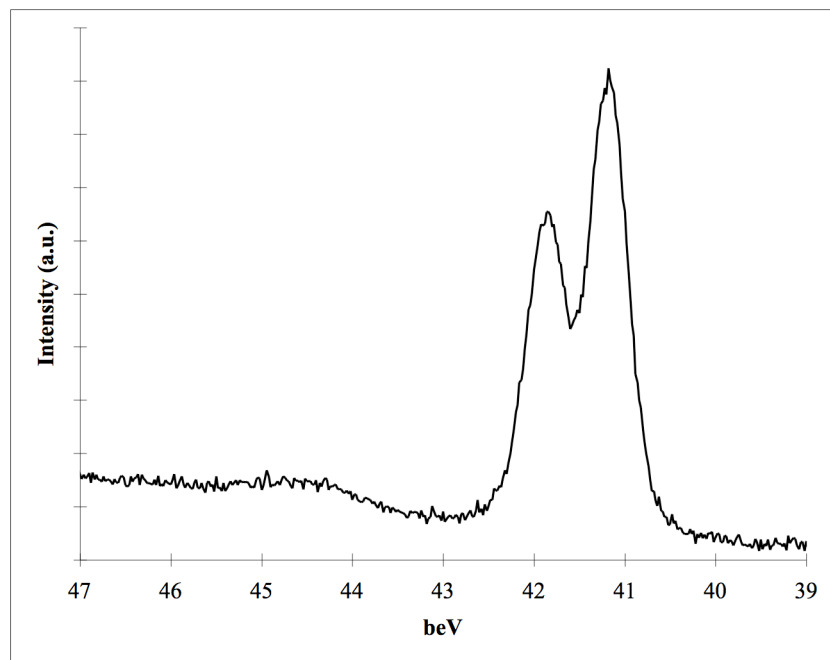


**Figure 3.4.** a—The high-resolution SXPS As 3d spectra of PET<sub>3</sub> functionalized GaAs(111)A, fit to a single spin-orbit doublet; b—the uncorrected SXPS As 3d spectrum, showing a small amount of As<sub>2</sub>O<sub>3</sub> contamination between 44 and 45 eV.

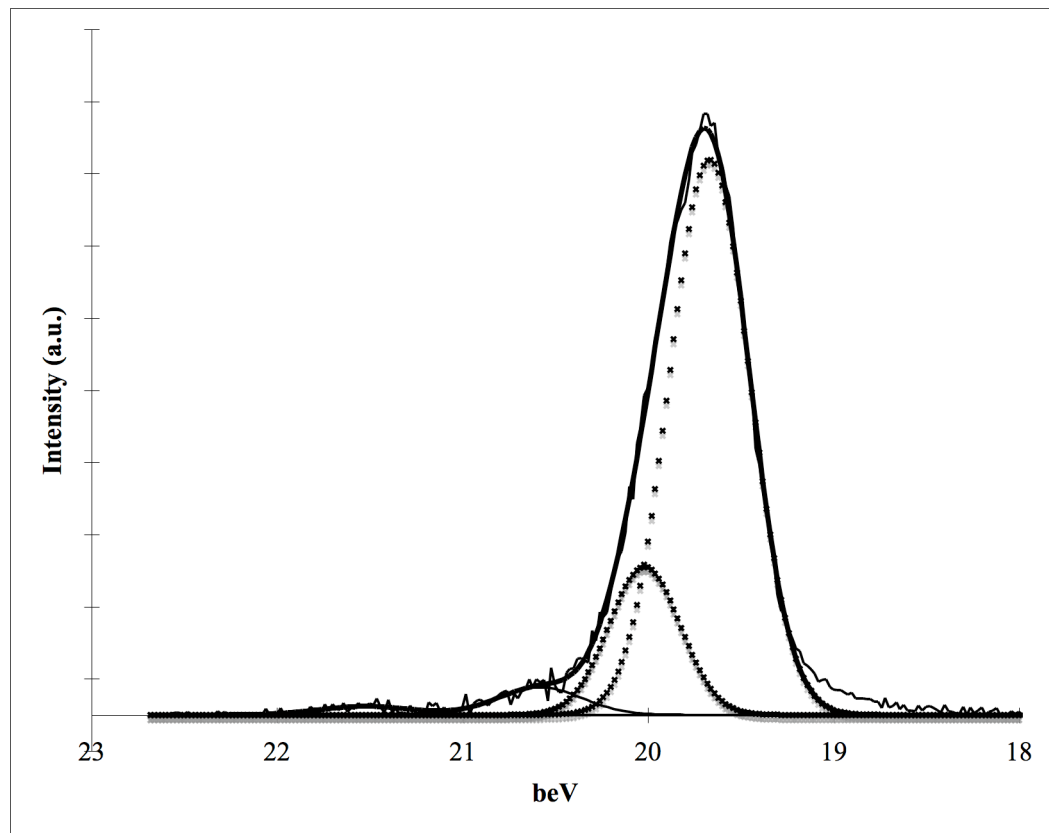


**Figure 3.5.** The high-resolution SXPS Ga 3d spectrum of PEt<sub>3</sub> functionalized GaAs(111)A. The Ga 3d<sub>3/2</sub> components of each peak have been deconvoluted from the spectrum and the data fit to a bulk Ga(As) peak, and peaks shifted 0.35, 0.92, and 1.86 eV to higher binding energy. These peaks correspond to Ga-Cl, Ga<sub>2</sub>O, and Ga<sub>2</sub>O<sub>3</sub>, respectively.

observed for Ga<sub>2</sub>O on the native oxide-capped surface. The binding energy of the last peak on the surface was 1.86 eV higher than the bulk, a substantially larger shift than 1.43 eV difference between the bulk and Ga<sub>2</sub>O<sub>3</sub> peaks on the native oxide-capped surface. This discrepancy is likely due to the difficulty in fitting such a low intensity peak.

It should be noted that the absolute values of the corrected binding energies of these peaks were substantially (0.3 eV) higher than those observed on both the oxide and Cl-terminated surfaces. However, in the absence of an absolute charge reference, the binding energy shifts of surface species are more significant than their absolute values. While these experiments were not of sufficient resolution to discern bulk Ga(As) from P-bonded Ga species, they are consistent with the chemical model described above. However, absent the ability to resolve these peaks, equivalent monolayer coverage calculations are inherently unphysical, and are not included.

The reaction chemistry of PCl<sub>3</sub> on Cl-terminated GaAs(111)A is considerably more complex. After treatment with PCl<sub>3</sub>, a P 2p peak is clearly observed in the photoelectron spectrum (figure 3.6). Fitting this signal to a single doublet yielded peak widths larger than those observed for PEt<sub>3</sub>, while fitting it to two peaks yielded more consistent results. The P 2p<sub>3/2</sub> component of the lower binding doublet was observed at  $133.9 \pm 0.04$ . This 1.1 eV shift to higher binding energy is consistent with the greater electronegativity of the Cl groups on PCl<sub>3</sub> relative to the ethyl groups on PEt<sub>3</sub>. However, a roughly 1.5:1 ratio between this P peak and the Cl peak was observed, not the excess of Cl expected for simple binding of PCl<sub>3</sub> atop Ga surface sites. Further, the equivalent monolayer coverage of this peak relative to Ga 3d is  $0.87 \pm 0.29$  ML. This large excess

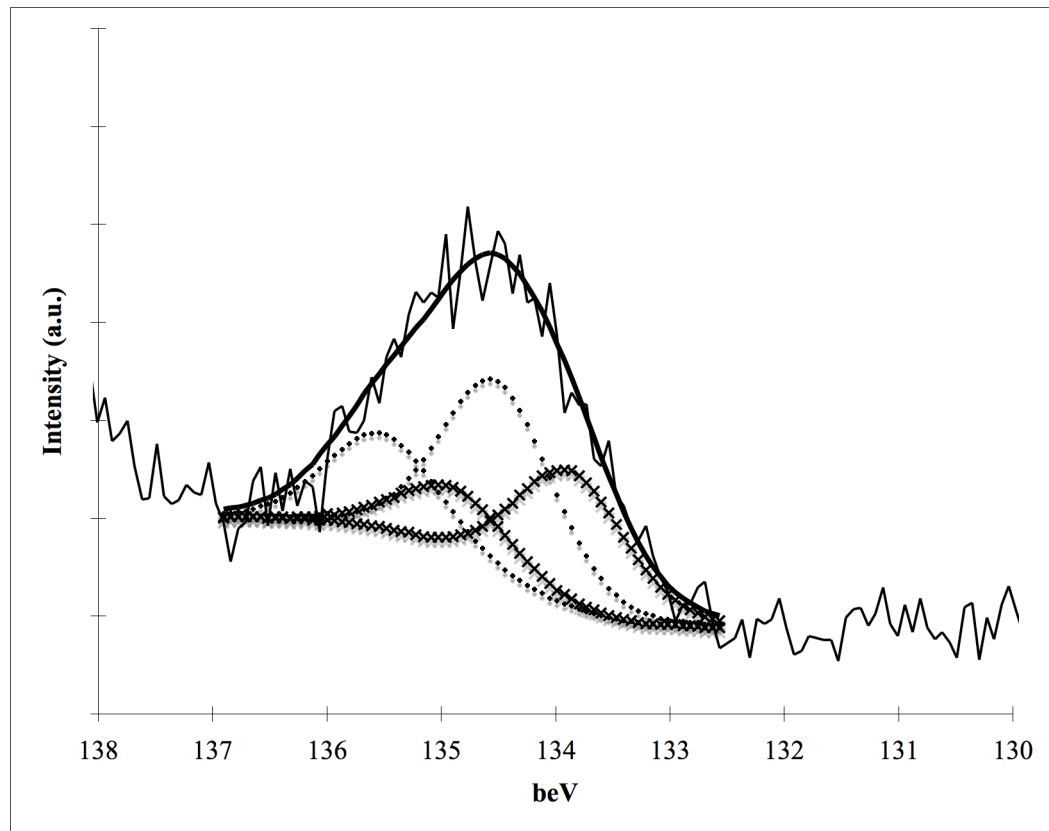


**Figure 3.6.** The P 2p XPS spectrum of Cl-terminated GaAs(111)A after reaction with  $\text{PCl}_3$ . The peak has been fit to two spin-orbit doublets, whose characteristics are described in the text.

of P suggests that the Cl groups are quite labile during surface reactions, and a significant amount of P is bound in other configurations. The higher binding energy P 2p<sub>3/2</sub> component was observed at  $134.6 \pm 0.04$ , with a coverage of  $1.14 \pm 0.45$  ML.

The Ga and As peaks appeared completely free of contaminants on the Caltech XPS. The high-resolution SXPS spectra of the As 3d region of these surface confirmed that no As oxides or As<sup>0</sup> were present on the surface at a detectable concentration, and the observed signal was fit to single doublet (figure 3.7). The Ga 3d<sub>3/2</sub> peaks of the Ga 3d spectrum of these samples were deconvoluted using the procedure described above, and the spectrum fit to 4 peaks (figure 3.8). These fits were quite sensitive to initial conditions. To avoid selection bias in selecting a fit, the binding energies reported here are averaged over multiple fits performed with different initial conditions. Thus, the standard deviations reported for these binding energy shifts reflect uncertainties in the fits rather than averages over multiple spectra.

The binding energy shift of  $0.92 \pm 0.03$  between the bulk peak and the third peak is consistent with the value expected for Ga<sub>2</sub>O, while the  $2.04 \pm 0.02$  eV shift to the highest binding energy peak is similar to the value of 1.86 eV observed for higher-order oxide contamination on the PEt<sub>3</sub> treated surface. The identity of the second peak in the spectrum is more difficult to ascertain. It is shifted to  $0.29 \pm 0.05$  eV higher binding energy than the bulk peak. The upper range of this limit includes the shift of 0.34 eV observed for Ga-Cl bonds. However, as the loss of some Cl groups on P has been observed, this peak may also represent different P bonding geometries, such as Ga-P multiple bonds, and no assignment can be conclusively made. Qualitatively though, it can be seen that these surfaces are prepared with extremely minimal oxide contamination.

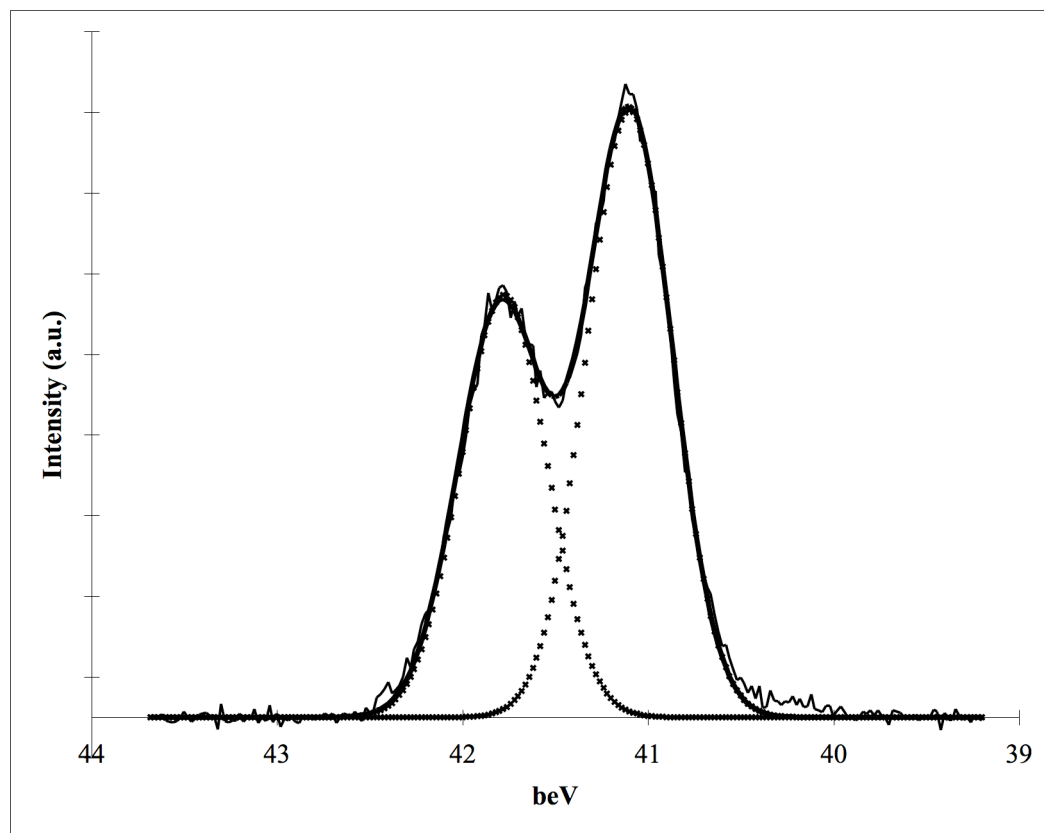


**Figure 3.7.** The high-resolution SXPS As 3d spectra of Cl-terminated GaAs(111)A after functionalization with  $\text{PCl}_3$ , fit to a single spin-orbit doublet.

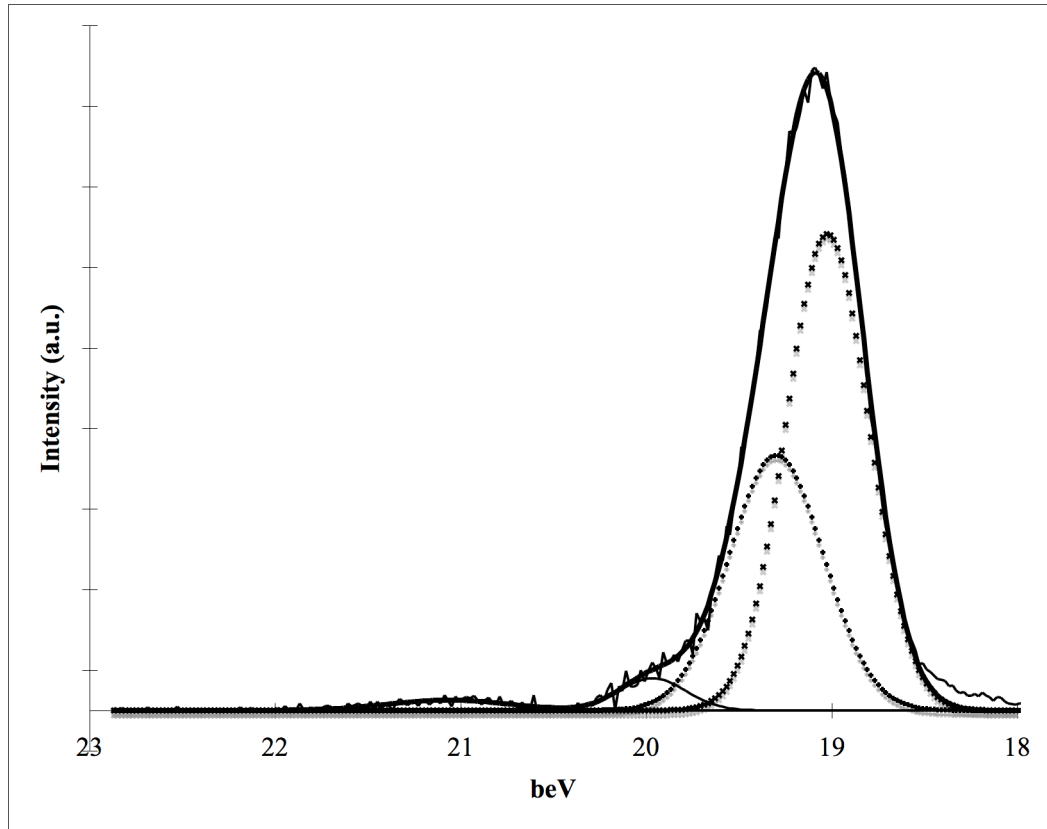


**Figure 3.8.** The high-resolution SXPS Ga 3d spectrum of Cl-terminated GaAs(111)A after functionalization with  $\text{PCl}_3$ . The Ga  $3d_{3/2}$  components of each peak have been deconvoluted from the spectrum and the data fit to a bulk Ga(As) peak, and peaks shifted 0.29, 0.92, and 2.04 eV to higher binding energy. The latter two peaks correspond to  $\text{Ga}_2\text{O}$  and  $\text{Ga}_2\text{O}_3$  respectively, while the peak shifted by 0.29 eV has not been assigned.

### 3.3.2 Reactions of $\text{PCl}_3$ on Native Oxide-Terminated GaAs(111)A

The reaction of  $\text{PCl}_3$  with the native oxide-capped GaAs(111)A surface results in the appearance of both P and Cl 2p doublets on the surface (figure 3.9). The relative surface abundance of P:Cl based on these peaks is  $0.14 \pm 0.03$ , less than the value of 0.33 expected for simple atop  $\text{PCl}_3$  binding. The equivalent monolayer coverage of P is  $0.13 \pm 0.03$ , lower than that observed for  $\text{PEt}_3$ . The binding energy of the  $2p_{3/2}$  component of the doublet occurred at 133.4 eV, slightly lower than the 133.9 eV for  $\text{PCl}_3$  on etched surfaces.

Like the  $\text{PEt}_3$  treated surfaces, some of the  $\text{PCl}_3$  treated surfaces showed broader, more intense P 2p peaks, which were fit to 2 doublets with P  $2p_{3/2}$  components at 133.6 and 134.2 eV (figure 3.9). In contrast to experiments with  $\text{PEt}_3$ , the intensity of both doublets was enhanced, the lower binding energy component now appeared significantly more abundant than Cl on the surface, and coverages in excess of 1 equivalent ML were observed. Additionally, when the samples described above were annealed to 350 °C under Schlenk line vacuum, the surface Cl disappeared and the relative intensity of the P peak increased to 0.55 ML. The binding energy of this peak was unchanged. Together, these observations suggest that the  $\text{PCl}_3$  groups are extremely sensitive to even trace contaminants, and that loss of the Cl groups leads to drastic changes in the P 2p spectrum.

No oxide contaminants were observed in the As and Ga 3d photoelectron spectra at Caltech, suggesting that  $\text{PCl}_3$  might be an effective agent for passivating GaAs without requiring an etching step. A control experiment with  $\text{PEt}_3$  led to the appearance of some P on the surface, but no removal of As and Ga oxides was observed. SXPS spectra of the As 3d region showed that  $\text{PCl}_3$  was as effective at removing As oxide species as aqueous

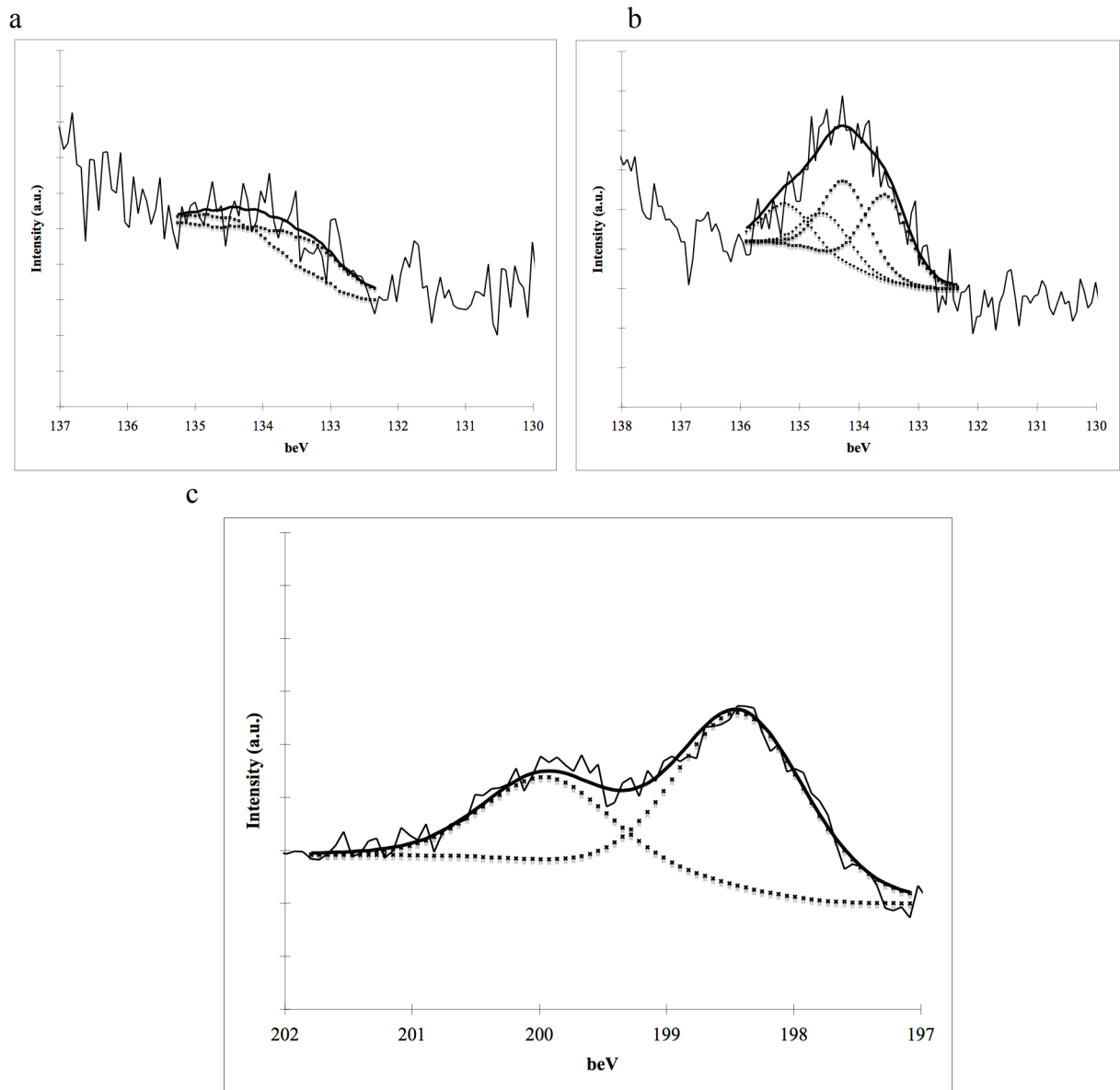


**Figure 3.9.** a—The P 2p XPS peak of native oxide-capped GaAs(111)A surfaces after reaction with PCl<sub>3</sub>, fit to a single spin-orbit doublet; b—The same surface after annealing to 350 °C on a Schlenk line, now fit to 2 doublets with significantly greater intensity; c—The Cl 2p XPS spectra of this surface, as freshly prepared.

HCl etching. However, a detailed fit of the spectrum revealed an important difference with surfaces which had been etched in aqueous solution (figure 3.10). This spectrum was best fit with 2 doublets, a bulk component and smaller doublet shifted to 0.69 eV higher binding energy. This shift is consistent with contamination of elemental As on the surface. Using the same model that was applied to oxide overlayers, the integrated area ratios yield a surface coverage of 0.05 equivalent monolayers. For a well-ordered (111)A surface, the bulk As signal will be attenuated by a layer of Ga bulk atoms, while surface As contaminants will not. However, this model seemed to underestimate the coverage of Ga surface species, so this coverage can only be taken as a rough estimate of the amount of surface As<sup>0</sup>.

Like the Ga 3d spectra described above, deconvolution of the Ga 3d<sub>3/2</sub> peak components was required to obtain reasonable fits, and final values were sensitive to initial conditions. Although there was a small (0.2 eV) shift in the absolute binding energies observed, the Ga 3d spectrum was nearly identical to that observed for etched, PCl<sub>3</sub>-treated surfaces (figure 3.11). The spectrum was fit to 4 peaks, corresponding to the bulk, Ga<sub>2</sub>O, Ga<sub>2</sub>O<sub>3</sub> and an unknown species shifted 0.30 eV to higher binding energy than the bulk.

### **3.3.3 Oxidation of Phosphine-Functionalized GaAs(111)A in Ambient Atmosphere**

To help understand the stability of these passivation chemistries, SXPS spectra were also collected after exposure of the surfaces to ambient air and light for 12 hours. Accurate background subtractions could not be performed on the full As 3d spectra for most samples, so quantitative evaluations of As oxide coverage could not be obtained.

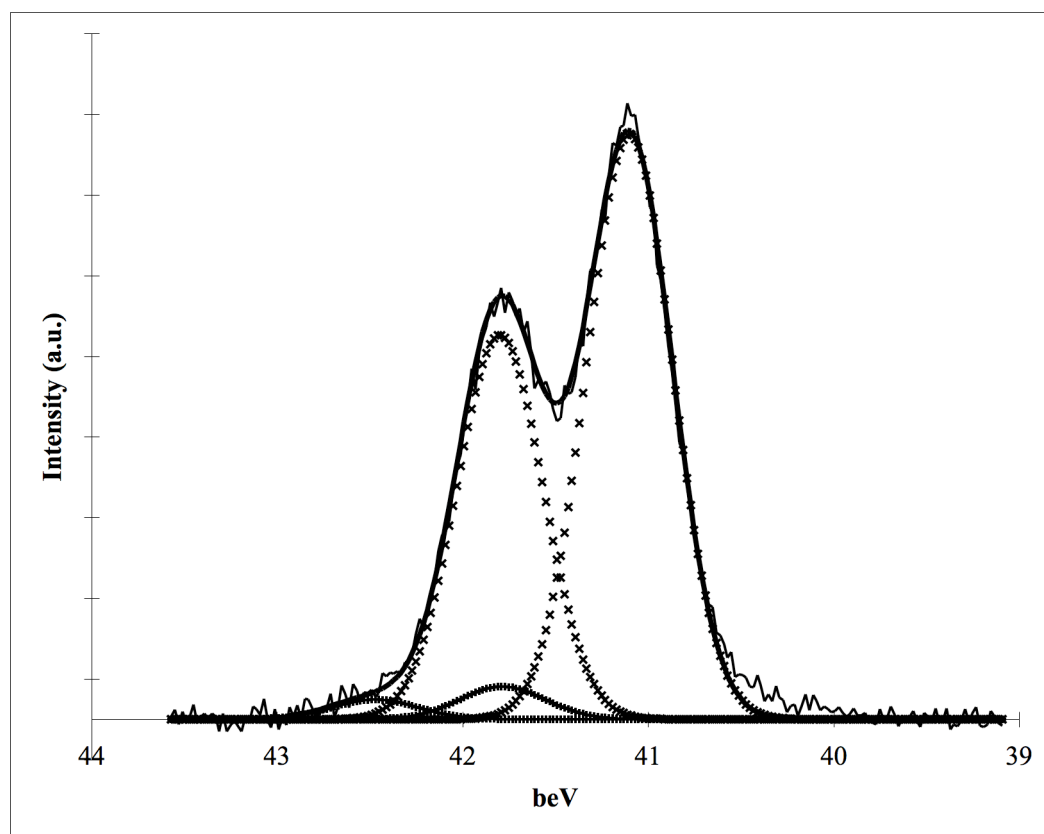


**Figure 3.10.** The high-resolution SXPS As 3d spectrum of native oxide-capped GaAs(111)A after functionalization with  $\text{PCl}_3$ . The spectrum is well fit by two spin-orbit doublets, representing bulk (Ga)As and, shifted to 0.69 eV higher binding energy,  $\text{As}^0$ .

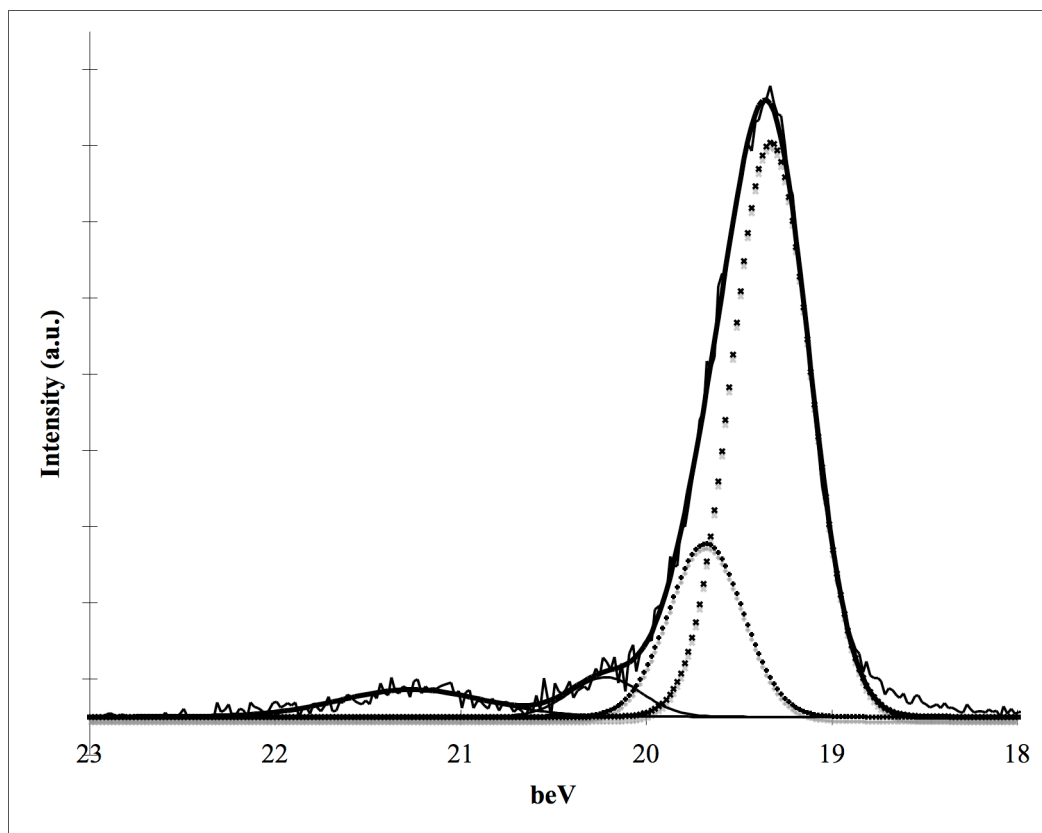


**Figure 3.11.** The high-resolution SXPS Ga 3d spectrum of Cl-terminated GaAs(111)A after functionalization with  $\text{PCl}_3$ . The Ga  $3d_{3/2}$  components of each peak have been deconvoluted from the spectrum and the data fit to a bulk Ga(As) peak, and peaks shifted 0.30, 0.90, and 1.97 eV to higher binding energy. The latter two peaks correspond to  $\text{Ga}_2\text{O}$  and  $\text{Ga}_2\text{O}_3$  respectively, while the peak shifted by 0.30 eV has not been assigned.

However, qualitative trends in surface oxidation could be observed, and  $\text{PCl}_3$  treated surfaces showed more oxide contamination than Cl-terminated or  $\text{PEt}_3$ -treated ones (figure 3.12). More quantitative fits could be obtained for the Ga 3d region, with Cl-terminated surfaces showing better stability than the  $\text{PCl}_3$  treated surfaces to Ga oxidation as well (figure 3.13). The greatest stabilization against oxidation was observed on  $\text{PEt}_3$ -functionalized surfaces.

### **3.3.4 Steady-State Photoluminescence of Functionalized GaAs(111)A**

Steady-state PL intensities were made on undoped samples to maximize the bulk emission efficiency.<sup>15</sup> Native oxide-capped samples were used as the standard of reference for PL enhancements. Measurement of the PL from samples with a freshly etched (111)A surface yielded a factor of 2 increase over the native oxide-terminated surface, consistent with previous reports.<sup>3</sup> After treatment with  $\text{PCl}_3$ , the PL was somewhat reduced relative to the Cl-terminated samples, with an intensity 1.7 times greater than the reference. In contrast to these improvements, no enhancement of PL intensity was observed for oxide-terminated surface treated directly with  $\text{PCl}_3$ , consistent with the observation of  $\text{As}^0$  contaminants. Further, the PL of the improved samples gradually decayed after exposure to air, and after 36 hours had reached the level of the native oxide-capped samples. Measurements have not yet been made on  $\text{PEt}_3$  treated samples.

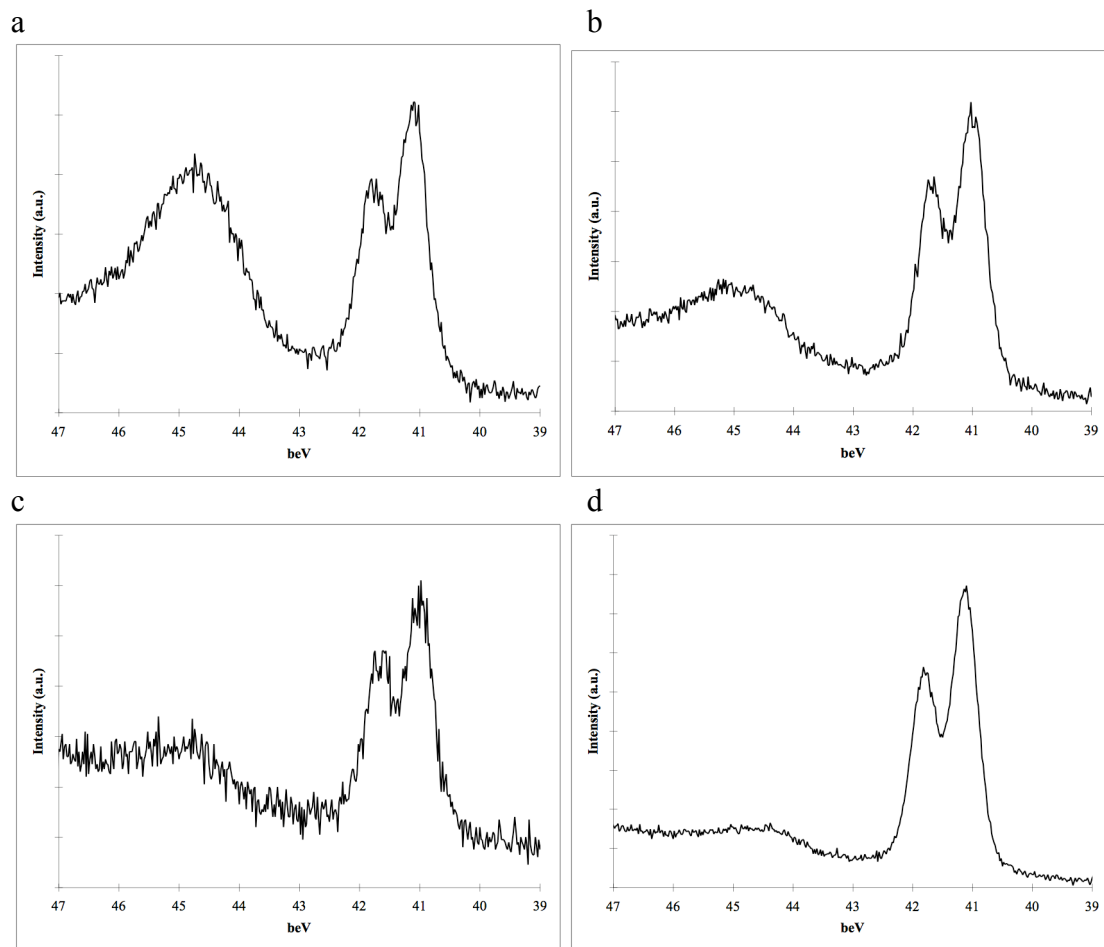


**Figure 3.12.** SXPS As 3d spectra after 12 hours in ambient air. a— $\text{PCl}_3$  on unetched GaAs(111)A; b— $\text{PCl}_3$  on Cl-terminated GaAs(111)A; c—Cl-terminated GaAs(111)A; d— $\text{PEt}_3$  on Cl-terminated GaAs(111)A

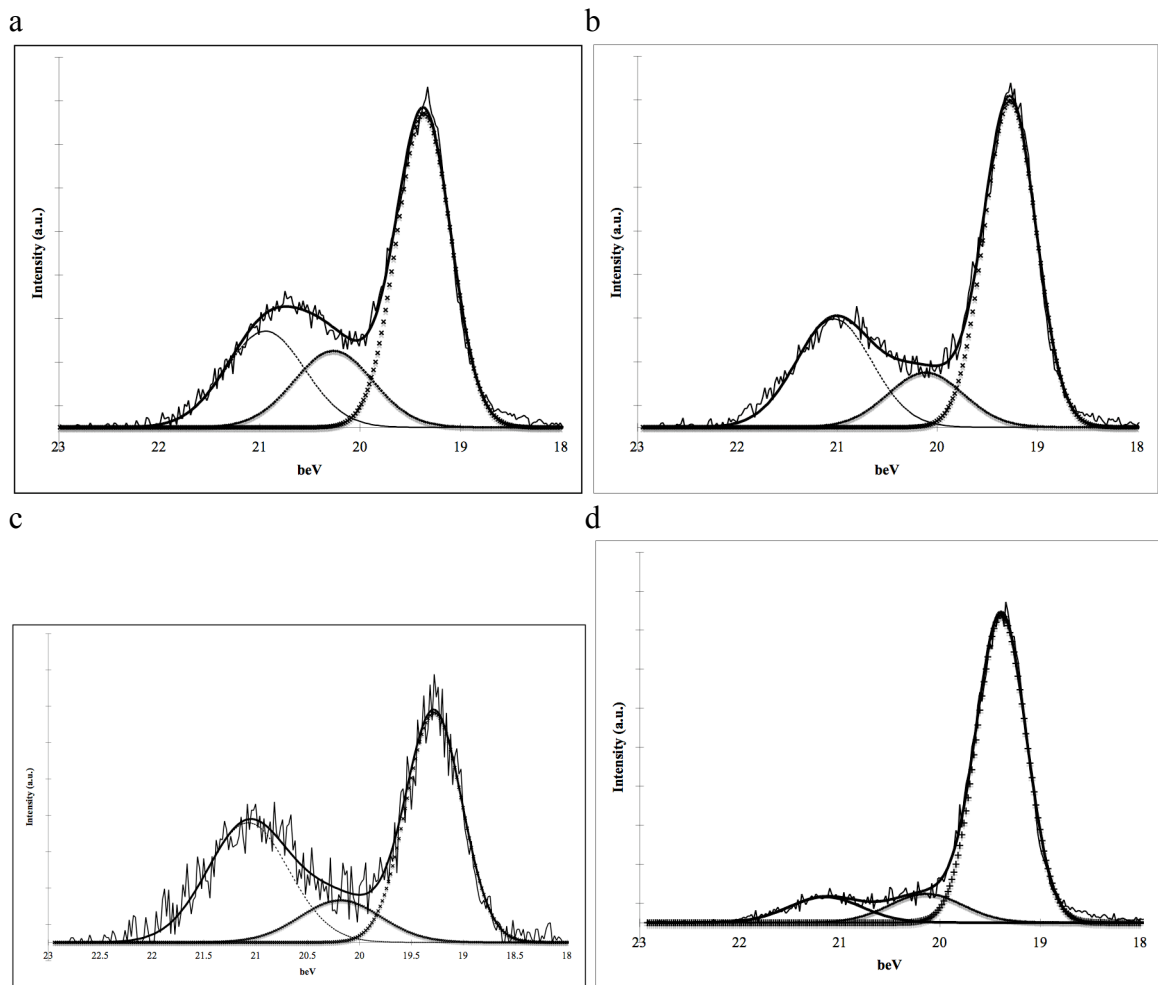


**Figure 3.13.** SXPS Ga 3d spectra after 12 hours in ambient air. a— $\text{PCl}_3$  on unetched GaAs(111)A; b— $\text{PCl}_3$  on Cl-terminated GaAs(111)A; c—Cl-terminated GaAs(111)A; d— $\text{PET}_3$  on Cl-terminated GaAs(111)A. The Ga  $3d_{5/2}$  components have been deconvoluted from all spectra, and the data fit to 3 peaks, representing bulk Ga(As),  $\text{Ga}_2\text{O}$ , and  $\text{Ga}_2\text{O}_3$ .

### 3.4 Discussion

An important question unresolved question from these experiments is the binding mode of the  $\text{PCl}_3$  on the Cl-terminated GaAs surface. The large excess of P relative to Cl on these surfaces, as well as the overall P coverage in excess of a monolayer for the etched surfaces, imply that simple atop binding of  $\text{PCl}_3$  on Ga surface sites is not occurring. One possible mechanism is reaction of  $\text{PCl}_3$  with surface bound water or hydroxides, forming surface bound phosphates. Alternatively, P may be incorporated into subsurface As sites, leaving a mixed GaAsP surface. Such a mechanism has been postulated as occurring for sulfide passivation of As sites on mixed surfaces, leaving a surface which is primarily  $\text{Ga}_2\text{S}_3$  passivated. While the Ga 3d binding energies for Ga(P) and Ga(As) are essentially identical, the binding energy of the P  $2p_{3/2}$  peak of GaP is known to occur at  $\approx 129$  eV,<sup>16,17</sup> while the value for  $\text{PCl}_3$  is has been reported to occur at 133.3 eV.<sup>18</sup> The observed shift to higher binding energies for  $\text{PCl}_3$  on the Cl-terminated surface is more consistent with the formation of oxygen containing phosphorus species than the more reduced phosphides. In this model, a small fraction of the observed P is due to Ga-bonded P species, while a much greater fraction is due to these surface phosphates or phosphine oxides. This model is also consistent with the much lower phosphorus coverages observed for the reaction of  $\text{PEt}_3$  with Cl-terminated surfaces, where the ethyl groups cannot be displaced to form phosphates.

Some correlations can be drawn between the observed chemical and photoluminescence properties. As oxides regrow on the surfaces of the etched and functionalized materials, the photoluminescence intensity decreases. Freshly prepared  $\text{PCl}_3$  functionalized surface formed without etching contain only trace As and Ga oxides,

significantly less than is observed on Cl-terminated surfaces after 12 hours in air.

Despite this greater oxidation, these Cl-terminated samples still show stronger PL than the freshly prepared  $\text{PCl}_3$ /oxide samples. These effects are ascribed to the presence of  $\text{As}^0$  on these  $\text{PCl}_3$  treated surface. Annealing of these surfaces above  $350\text{ }^\circ\text{C}$  in high vacuum should remove this contamination, and may make this technique an effective method of passivation.

### **3.5 Conclusions**

The reaction chemistry of  $\text{PEt}_3$  and  $\text{PCl}_3$  with the GaAs(111)A surface has been characterized with X-ray photoelectron and soft X-ray photoelectron spectroscopy. Using the Cl-terminated GaAs(111)A surface as a starting point,  $\text{PEt}_3$  has been found to react with 3050% of surface sites, leaving Cl atoms bound to the remaining surface Ga atoms. This surface has a small amount of contamination from both Ga and As oxides, but is free of elemental As. The reaction of  $\text{PCl}_3$  with the Cl-terminated surface leads to lower surface P coverages, closer to 20%. The surface-bound  $\text{PCl}_3$  is more reactive than  $\text{PEt}_3$ , and significant displacement of the Cl ligands occurs. This surface is also nearly oxide free. The reaction of  $\text{PCl}_3$  with the native oxide-terminated surface is similar, with nearly oxide-free surfaces observed. However, these surfaces contained small but observable concentrations of  $\text{As}^0$  and did not exhibit the steady-state photoluminescence enhancements observed on aqueously etched surfaces.

### 3.5 Acknowledgements

I acknowledge the Department of Energy, Office of Basic Energy Sciences, for support of this work. The research was carried out in part at the National Synchrotron Light Source, Brookhaven National Laboratory, which is supported by the U.S. Department of Energy, Division of Materials Sciences and Division of Chemical Sciences, under Contract No. DE-AC02-98CH10886. I thank Michael Sullivan for use of the N<sub>2</sub>(g)-purged glove box at the NSLS.

**References**

- (1) Aberle, A. G. *Progress in Photovoltaics* **2000**, *8*, 473.
- (2) Adams, D. M.; Brus, L.; Chidsey, C. E. D.; Creager, S.; Creutz, C.; Kagan, C. R.; Kamat, P. V.; Lieberman, M.; Lindsay, S.; Marcus, R. A.; Metzger, R. M.; Michel-Beyerle, M. E.; Miller, J. R.; Newton, M. D.; Rolison, D. R.; Sankey, O.; Schanze, K. S.; Yardley, J.; Zhu, X. Y. *Journal of Physical Chemistry B* **2003**, *107*, 6668.
- (3) Lu, Z. H.; Chatenoud, F.; Dion, M. M.; Graham, M. J.; Ruda, H. E.; Koutzarov, I.; Liu, Q.; Mitchell, C. E. J.; Hill, I. G.; McLean, A. B. *Applied Physics Letters* **1995**, *67*, 670.
- (4) Lu, Z. H.; Tyliczszak, T.; Hitchcock, A. P. *Physical Review B* **1998**, *58*, 13820.
- (5) Kalyuzhny, G.; Murray, R. W. *Journal of Physical Chemistry B* **2005**, *109*, 7012.
- (6) Sugino, T.; Sakamoto, Y.; Shirafuji, J. *Japanese Journal of Applied Physics Part 2-Letters* **1993**, *32*, L239.
- (7) Yablonovitch, E.; Sandroff, C. J.; Bhat, R.; Gmitter, T. *Applied Physics Letters* **1987**, *51*, 439.
- (8) Berkovits, V. L.; Ulin, V. P.; Losurdo, M.; Capezzuto, P.; Bruno, G.; Perna, G.; Capozzi, V. *Applied Physics Letters* **2002**, *80*, 3739.
- (9) Gmitter, T. J.; Yablonovitch, E.; Heller, A. *Journal of the Electrochemical Society* **1988**, *135*, 2391.
- (10) Nelson, R. J.; Williams, J. S.; Leamy, H. J.; Miller, B.; Casey, H. C.; Parkinson, B. A.; Heller, A. *Applied Physics Letters* **1980**, *36*, 76.

- (11) Skromme, B. J.; Sandroff, C. J.; Yablonovitch, E.; Gmitter, T. *Applied Physics Letters* **1987**, *51*, 2022.
- (12) Nemanick, E. J.; Hurley, P. T.; Brunshwig, B. S.; Lewis, N. S. *Journal of Physical Chemistry B* **2006**, *110*, 14800.
- (13) Traub, M. C.; Biteen, J. S.; Michalak, D. J.; Webb, L. J.; Brunshwig, B. S.; Lewis, N. S. *J. Phys. Chem. B* **2006**, *110*, 15641.
- (14) Eastman, D. E.; Chiang, T. C.; Heimann, P.; Himpfel, F. J. *Physical Review Letters* **1980**, *45*, 656.
- (15) Nelson, R. J. *Journal of Vacuum Science & Technology* **1978**, *15*, 1475.
- (16) Iwasaki, H.; Mizokawa, Y.; Nishitani, R.; Nakamura, S. *Surface Science* **1979**, *86*, 811.
- (17) Franke, R.; Chasse, T.; Streubel, P.; Meisel, A. *Journal of Electron Spectroscopy and Related Phenomena* **1991**, *56*, 381.
- (18) Fluck, E.; Weber, D. *Zeitschrift Fur Naturforschung Section B—A Journal of Chemical Sciences* **1974**, *B 29*, 603.

## Chapter 4

# Chemical Functionalization and Passivation of Gallium Arsenide Nanocrystals

### 4.1 Introduction—Surface Passivation and Semiconductor Nanocrystals

Semiconductor nanocrystals are one of the more promising electronic materials of recent years. Moderately efficient solar cells based on these nanocrystals have been fabricated,<sup>1</sup> and the use of chemically synthesized semiconductor nanocrystals may provide significant cost savings relative to traditional, high-purity semiconductors. More fundamentally, the size-dependent electronic properties of quantum dots can be used to selectively tune their optical absorption and emission properties.<sup>2</sup> These properties have already been exploited to make efficient light-emitting diodes, and could potentially allow a solar conversion device based on a single semiconductor material to exceed the Shockley-Queisser limit.<sup>3</sup>

Taking advantage of these properties requires effective surface passivation. This problem at the nanoscale than on bulk surface, both because of the much greater surface area and the requirement of simultaneously passivating several different crystal faces. Effective passivation of II-VI systems such as CdSe has been achieved both through

careful selection of organic ligands or growth of inorganic shells of ZnS.<sup>4,5</sup> GaAs nanocrystals are much less thoroughly studied than their various II-VI counterparts. Several procedures have been reported for the synthesis of GaAs nanocrystals,<sup>6,7</sup> many of which involve the reaction of an As precursor with GaCl<sub>3</sub>. The reaction is performed in a coordinating solvent that caps the nanocrystals and controls their growth.<sup>8,9</sup> However unlike II-VI nanocrystals, where both organic and inorganic surface passivation techniques greatly reduce the density of interface states and yield intense band-gap photoluminescence (PL), no such method has been reported to date for GaAs.

In this chapter, the passivation chemistry of the bulk surface is applied to GaAs nanocrystals to yield strongly enhanced band-gap PL emission. As described in chapter 2, etching native oxide-terminated single-crystal GaAs(111)A surfaces with a 6 M HCl(aq) solution produces highly ordered,<sup>10,11</sup> oxide-free<sup>12</sup> Cl-terminated surfaces. Furthermore, of all low-index GaAs surfaces, the (111)A face is known to have the slowest etch rate in contact with oxidizing etches.<sup>13</sup> Thus, it seemed reasonable that treating as synthesized, oxide-capped GaAs nanocrystals<sup>14</sup> with 6 M HCl(aq) would cleanly remove the oxide layer and anisotropically etch the nanocrystals, predominantly producing surfaces terminated by Ga-Cl bonds. X-ray photoelectron spectroscopy, powder X-ray diffraction, and transmission electron microscopy experiments demonstrate that this procedure indeed is applicable to GaAs nanocrystal surfaces. Furthermore, these surface-bound Cl groups can be displaced by wet chemical reactions to introduce other functional groups onto the GaAs surface. This two-step functionalization procedure is not restricted to bulky groups chosen to limit the growth of the nanocrystals, and allows for a significant degree of control over the chemistry of the resulting capped GaAs

nanocrystal surfaces. Importantly, such functionalized GaAs nanocrystals show intense band-gap PL, indicating that the electrical trap density has been significantly reduced on such surfaces and presumably enabling the use of GaAs nanocrystals for spectroscopic investigations and electronic device applications similar to those that have been developed to date for core-shell capped II-IV nanoparticles.<sup>1,15,16</sup>

## 4.2 Experimental

### 4.2.1 Materials and Methods

Arsenic powder (ESPI, 99.9999%), ultradry GaCl<sub>3</sub> (Alfa, 99.9999%), and 44:56 Na:K alloy (Strem) were used as received. Toluene (Aldrich) and bis(2-methoxy ethyl) ether (diglyme) (Alfa) were distilled over Na and degassed before use. Concentrated (12 M) HCl(aq) (Baker), concentrated N<sub>2</sub>H<sub>4</sub>(aq) (Aldrich, 35% wt), and sodium hydrosulfide hydrate (NaSH·xH<sub>2</sub>O) were used as received. Hydrazine-d<sub>4</sub> monohydrate-d<sub>2</sub> (Aldrich) was diluted with D<sub>2</sub>O (Aldrich) to give a 35% by weight solution. H<sub>2</sub>O with a resistivity of >17.8 MΩ cm<sup>-1</sup>, obtained from a Barnsted Nanopure system, was used at all times.

GaAs nanocrystals were synthesized according to the method of Kher and Wells.<sup>14</sup> First, 0.56 g of NaK alloy and 0.51 g of As (9% excess) were suspended in toluene and refluxed under flowing ultra-high purity Ar for 2 days, to yield (Na/K)<sub>3</sub>As. This black suspension was cooled to 0 °C, and 1.17 g of GaCl<sub>3</sub> dissolved in either toluene or bis(2-methoxy ethyl) ether was then added. This mixture was refluxed for an additional 2 days under Ar. The solution was then cooled to room temperature and ~70 mL of H<sub>2</sub>O was added. After 30 min of stirring under Ar, the black suspension was

opened to air, filtered, and rinsed with water. The collected dark grey solids were heated to 350 °C under vacuum to remove excess As. Alternatively, when the reaction was complete, ~70 mL of CH<sub>3</sub>OH was added. After 30 min of stirring, the suspension was then allowed to settle for 24 h. The supernatant solution was removed, ~300 mL of CH<sub>3</sub>OH added, and the solution was allowed to settle for another 24 h. The supernatant was then removed and the black solids were collected by centrifugation. These solids were rinsed with CH<sub>3</sub>OH, dried *in vacuo*, and heated to 350 °C under vacuum to remove excess As.

To Cl terminate the surfaces, the synthesized GaAs nanoparticles were sonicated in a 6 M HCl(aq) solution for 40 min and the suspension was then centrifuged. The etching solution was removed with a pipette, and the collected particles were rinsed with fresh etching solution. The particles were sonicated in a fresh etching solution for another 5 min, and then centrifuged again. The 6 M HCl(aq) solution was removed and the particles were then collected.

Hydrazine functionalization reactions were performed by sonicating the etched GaAs nanocrystals for 30 min in concentrated ( $\approx 17$  M) hydrazine solution (aq) and allowing the particles to settle at ambient temperature for an additional 2 h. The particles were then centrifuged and the supernatant was removed, followed by rinsing and centrifugation with water or acetone. Once dispersed in acetone, the solids could not all be collected by centrifugation, and the acetone rinses retained a reddish-brown color, suggesting a significantly higher solubility for the functionalized particles. This solution displayed an absorption onset at  $\approx 480$  nm, but was not subjected to further analysis.

Functionalization with NaSH was performed by the same method as for hydrazine except that a ~1 M NaSH(aq) solution was used instead of the hydrazine solution. As with the hydrazine-treated particles, some fraction of the NaSH-treated GaAs nanoparticles could not be collected by centrifugation, leaving a reddish-brown supernatant.

#### 4.2.2 Instrumentation

TEM images were obtained on a Philips EM430 300 kV microscope. Powder X-ray diffraction (XRD) data were collected using a Philips X'Pert Pro diffractometer with a Cu anode X-ray source. Samples for XRD were dispersed onto a “zero-background” Si substrate.

X-ray photoelectron spectroscopy (XPS) was performed using a Surface Science M-Probe system.<sup>17,18</sup> Samples were dispersed on degreased, conductive Si substrates, inserted via a quick-entry load lock into the ultra-high vacuum (UHV) chamber, and kept at a base pressure of  $\leq 1 \times 10^{-9}$  Torr. Data collection and analysis were performed as described in section 2.2.2.

Diffuse reflectance infrared (IR) spectra were collected with a Vertex 70 Fourier transform IR (Bruker Optics) using a Seagull variable-angle reflectance (Harrick Scientific) attachment. The sample chamber was continually purged with  $N_2(g)$  during data collection. Samples were dispersed on degreased stainless steel plates. Data were collected from  $4000 \text{ cm}^{-1}$  to  $500 \text{ cm}^{-1}$  at  $2 \text{ cm}^{-1}$  resolution for angles between 15 and 60 degrees. For each sample 256 scans were taken, with background scans of the sample plate subtracted from each spectrum. Reflectance spectra were Kubelka-Munk

transformed ( $KM = (1-R)^2/2R$ ), and for samples with stronger light scattering, a scattering background was subtracted.

Photoluminescence (PL) measurements were made on particles that were dispersed in optical grade  $\text{CH}_3\text{OH}$  (EMD Chemicals). The particles were then either loaded into quartz cuvettes or were deposited as films on Si substrates. The particles were excited with an Ar ion laser operating at 488 or 514 nm at an output power density of  $300 \text{ mW mm}^{-2}$ . No differences in PL behavior were observed between spectra collected at these different excitation wavelengths. The PL signals were collected from the front face of the Si substrate or the cuvette with a Princeton Instruments Spec-10 Si charge-coupled device (CCD) detector (sensitivity range 200 – 1100 nm) cooled with liquid  $\text{N}_2$  to  $-132^\circ\text{C}$ , in conjunction with a 27.5 cm focal length Oriel MS257 grating spectrograph. A 550 nm long-pass filter in front of the entrance slit was used to cut off scattered laser illumination.

## 4.3 Results and Discussion

### 4.3.1 Characterization of Oxide-Coated GaAs Nanocrystals

#### 4.3.1.1 *X-ray Diffraction*

Figure 4.1 shows the powder X-ray diffraction pattern for the toluene synthesized, oxide-capped GaAs nanocrystals. The most prominent peaks were ascribable to reflections from the GaAs lattice planes. Two broad peaks were also clearly observed, indicative of the presence of some amorphous  $\text{Ga}_2\text{O}_3$ .

The average diameter,  $L$ , of these crystallites was determined through use of the Scherrer equation:<sup>19</sup>

$$L = \frac{K\lambda}{B\cos\vartheta} \quad (4.1)$$

In this relationship,  $K$  is a structure constant of 0.94,  $\lambda$  is the wavelength of the X-rays,  $B$  is the full width at half maximum of the diffraction peak, and  $\theta$  has its usual meaning. Based on the reflection of the GaAs (111) plane, the crystals had an average diameter of 39 nm, close to the reported value of 36 nm,<sup>14</sup> and well above the calculated quantum confinement limit for GaAs of ~19 nm.<sup>2</sup>

Somewhat smaller (~30 nm) diameter GaAs nanocrystals were produced when the GaCl<sub>3</sub> precursor was dissolved in diglyme, rather than toluene. Such nanocrystals were however significantly larger than those obtained previously using nominally the same preparation method.<sup>14,20</sup> GaAs nanoparticles synthesized with diglyme and worked up in CH<sub>3</sub>OH were approximately the same size, but exhibited significantly less Ga<sub>2</sub>O<sub>3</sub> in the XRD data than those synthesized in diglyme and worked up in H<sub>2</sub>O.

#### 4.3.1.2 *X-ray Photoelectron Spectroscopy*

Due to substantial charging effects, the XPS data on the oxide-capped particles were difficult to interpret quantitatively. The use of an electron gun for charge compensation greatly decreased the signal-to-noise ratio relative to that obtained on more conductive samples. To within the sample depth of the experiment, the data were completely dominated by signals arising from Ga and As oxides (figure 4.2). The surface was significantly enriched in gallium oxides, presumably due to sublimation of As<sub>2</sub>O<sub>3</sub> during the purification step.

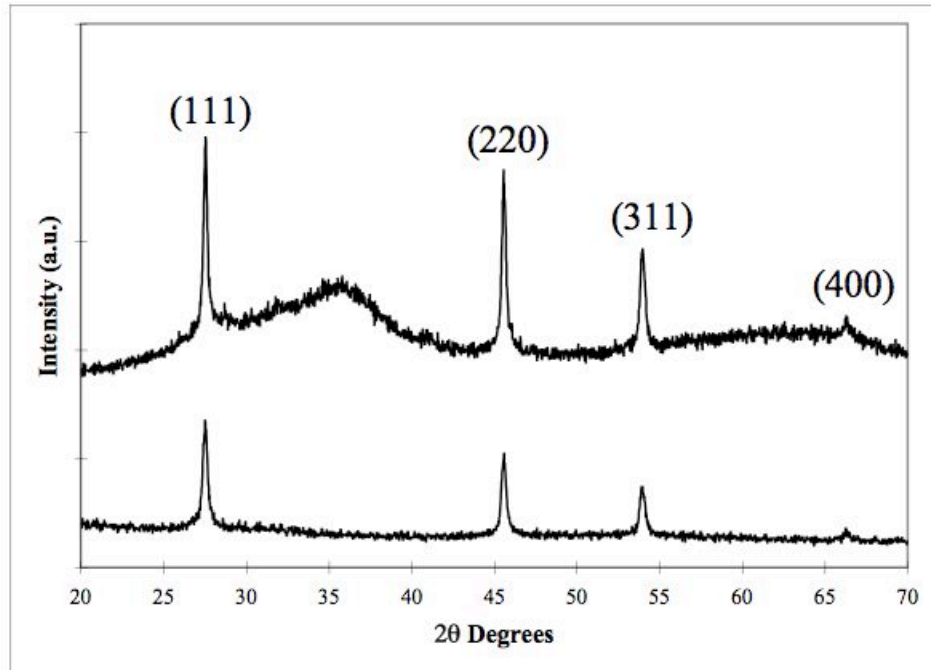


**Figure 4.1.** The powder X-ray diffraction pattern of GaAs nanocrystals, synthesized from toluene. The upper diffraction pattern is for the as-synthesized material, while the lower one was measured after HCl(aq.) etching. Index labels refer to GaAs lattice reflections, while the broad peaks centered at approximately 35° and 65° in the as-synthesized diffraction pattern correspond to Ga<sub>2</sub>O<sub>3</sub>.

#### 4.3.1.3 *Diffuse Reflectance IR Spectroscopy*

The diffuse reflectance IR spectra of neat powders of oxide-terminated GaAs nanoparticles worked up in MeOH exhibited broad peaks observed at 1225  $\text{cm}^{-1}$ , 1040  $\text{cm}^{-1}$ , and 825  $\text{cm}^{-1}$ , and 630  $\text{cm}^{-1}$  (figure 4.3), respectively. For the nanocrystals worked up in  $\text{H}_2\text{O}$ , the band at 825  $\text{cm}^{-1}$  was significantly more intense. In accord with previous IR studies of GaAs and its oxides,<sup>21</sup> the bands at 1040 and 825  $\text{cm}^{-1}$  can be ascribed to  $\text{As}_2\text{O}_3$ . The band at 1040  $\text{cm}^{-1}$  has been observed for the cubic Arsenolite phase of  $\text{As}_2\text{O}_3$ ,<sup>22</sup> while the band at 825  $\text{cm}^{-1}$  has been observed for the monoclinic Claudetite phase of  $\text{As}_2\text{O}_3$ .<sup>23</sup> A strong band at 625  $\text{cm}^{-1}$  has been observed for amorphous  $\text{As}_2\text{O}_3$ .<sup>22</sup> The GaAs nanocrystal IR data also contained a broad peak at  $\sim 3600$   $\text{cm}^{-1}$  and a weaker peak at  $\sim 1600$   $\text{cm}^{-1}$ , both of which were assigned to surface-bound water.

The XPS results (figure 4.2) indicated the presence of significantly more gallium oxides than arsenic oxides, so the IR data would be expected to also exhibit signals ascribable to Ga(III) oxides. No IR signals were observed at the energies reported for powdered<sup>21</sup> or cubic  $\beta$ - $\text{Ga}_2\text{O}_3$ .<sup>22</sup> The observed peaks for amorphous  $\text{Ga}_2\text{O}_3$ <sup>22</sup> are however at 305 and 550  $\text{cm}^{-1}$ , which is outside of the experimentally observable energy range. Consistently, the XRD data (figure 4.1) suggest that the native oxide is highly amorphous. The peak at 1225  $\text{cm}^{-1}$  is tentatively assigned to  $\text{Ga}_2\text{O}$ , a known component of native oxides on GaAs.

### 4.3.2 Characterization of HCl(aq)-Etched GaAs Nanocrystals

#### 4.3.2.1 *X-ray Diffraction*

After etching with HCl(aq), only GaAs-based plane reflections, and no signals

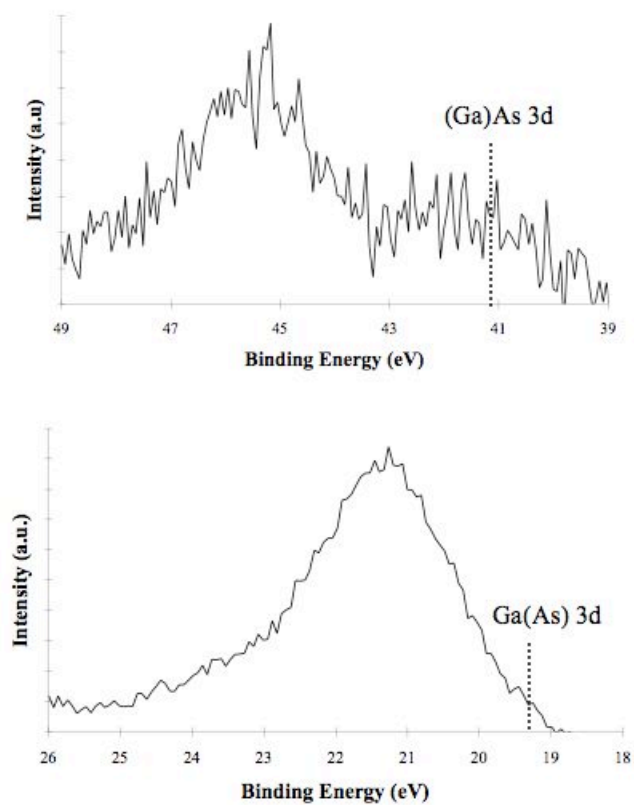


**Figure 4.2.** XPS spectra of as-synthesized GaAs nanocrystals from toluene, showing the As 3d (above) and Ga 3d (below) regions. Dotted lines show the expected binding energy of the bulk GaAs peaks.

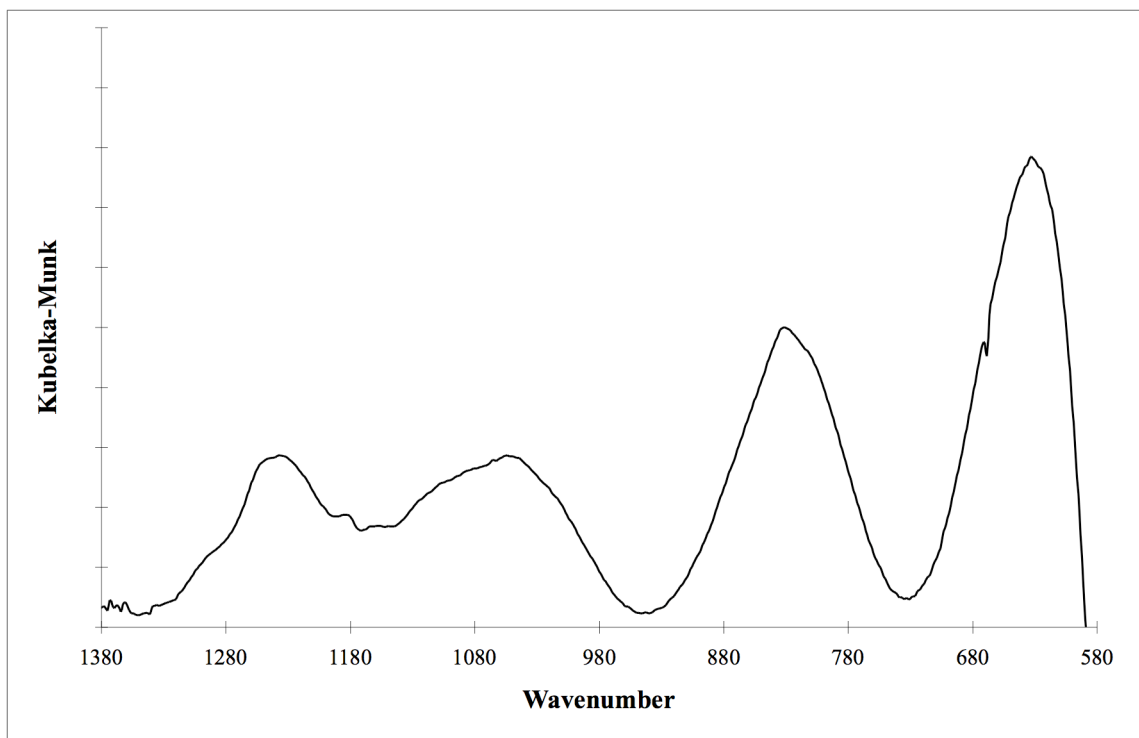


**Figure 4.3.** The diffuse reflectance infrared spectrum of as-synthesized GaAs nanocrystals. Peaks at 1040, and 825, and 630  $\text{cm}^{-1}$  are correspond to  $\text{As}_2\text{O}_3$ , while the peak at 1225  $\text{cm}^{-1}$  is assigned to  $\text{Ga}_2\text{O}$ .

ascribable to amorphous  $\text{Ga}_2\text{O}_3$ , were present in the XRD pattern (figure 4.1) of the GaAs nanoparticles. Line broadening measurements of the etched particles indicated their average diameter had been reduced to  $\sim 22$  nm. This behavior implies that the crystalline core, as well as the surface oxides, had been etched.

#### 4.3.2.2 *Transmission Electron Microscopy*

TEM images revealed the effects of this etching on the morphology of the nanocrystals. The oxide-capped nanocrystals were observed to be roughly spherical (figure 4.4). In contrast, the etching process was anisotropic, and crystal facets were revealed (figure 4.5). The obtained TEM images were not of sufficient resolution to determine which faces had been revealed. However, studies on single crystals have shown that the (111)A, Ga-rich surface is the face that is most slowly etched under oxidizing conditions,<sup>13</sup> hence it is likely that this face was the one that was preferentially revealed by the 6 M HCl(aq) etch.

#### 4.3.2.3 *X-ray Photoelectron Spectroscopy*

##### a) Cl 2p Signals

As expected, Cl signals were observed in survey scans of the HCl(aq)-etched GaAs nanocrystals. A detailed scan of the Cl 2p region revealed a doublet, with the Cl  $2p_{3/2}$  peak centered at 198.5 eV. The relative intensity of this doublet, compared to the neighboring As 3s peak (205 eV), was much greater than that observed on the Cl-terminated GaAs(111)A surface,<sup>12</sup> as expected for a surface-bound species on a higher surface area sample. When the HCl(aq)-etched GaAs particles were rinsed with water, methanol, or acetone, the Cl signal was not observed, suggesting that the surface Cl-

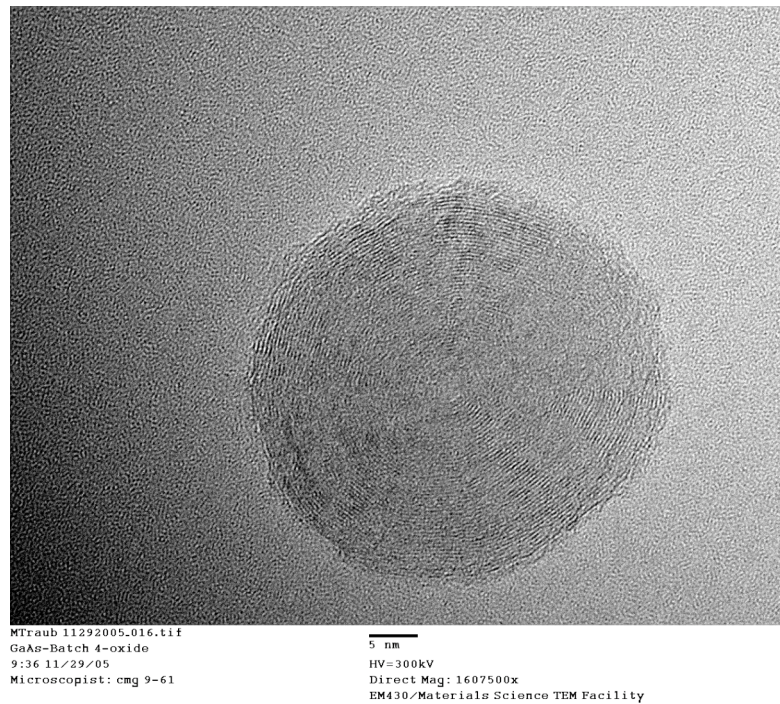
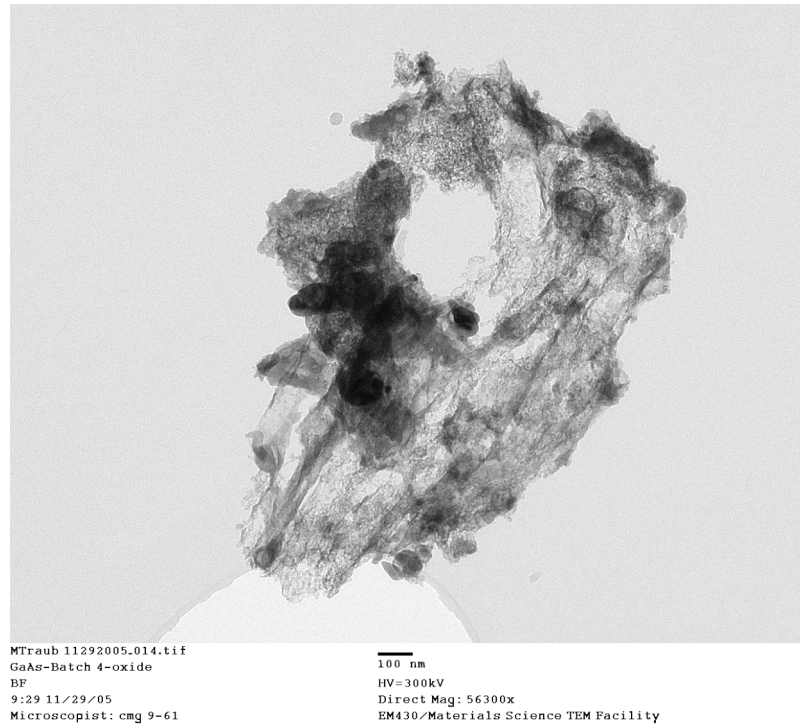


**Figure 4.4.** Transmission electron micrographs of oxide-terminated GaAs nanocrystals. above—A collection of agglomerated particles; below—A single oxide-terminated particle.

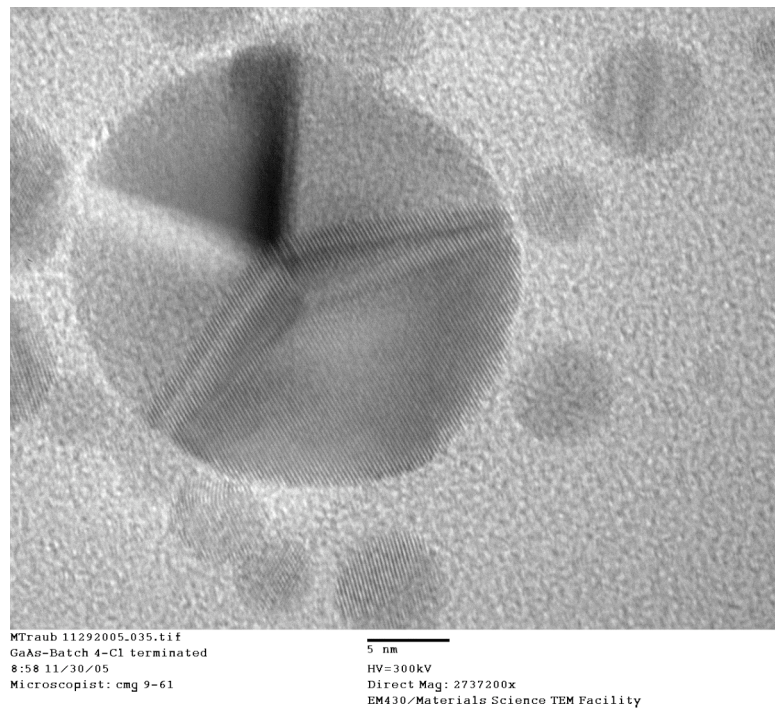
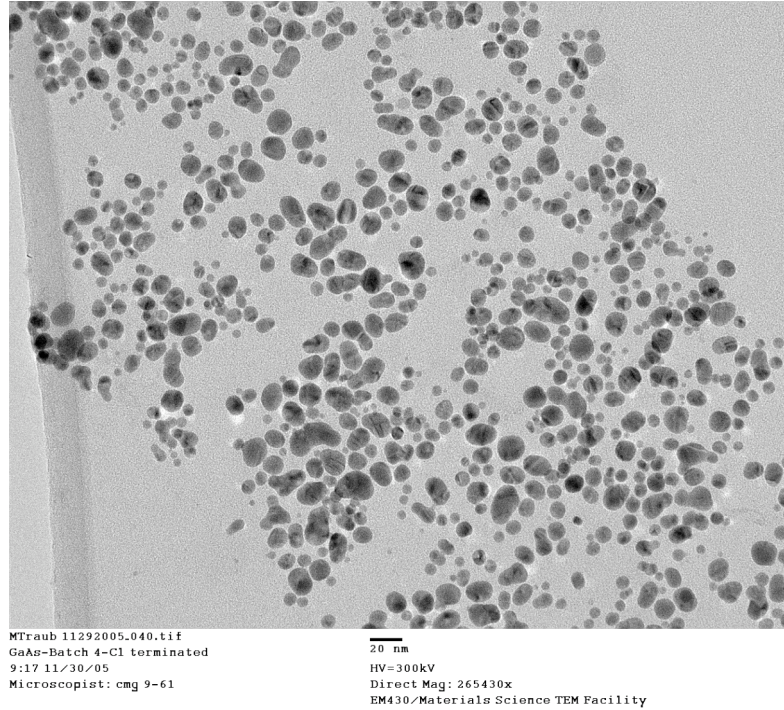


**Figure 4.5.** TEM images of Cl-terminated GaAs nanocrystals. In contrast to the oxide-terminated nanocrystals, the Cl-terminated particles are well separated, and the beginnings of facet formation can be seen.

bonds are relatively reactive.

#### b) As 3d signals

XPS data for the As 3d region of the HCl(aq)-etched GaAs particles showed the complete removal of As oxides (figure 4.6). The remaining As signal was resolved into two spin-orbit doublets, representing two As chemical species on the surface. The lower energy As 3d<sub>5/2</sub> peak at 41.1 eV is consistent with expectations for bulk GaAs. The As 3d<sub>5/2</sub> peak at 0.6 eV higher binding energy is assigned to elemental As, consistent with previous reports for the binding energy of As<sup>0</sup>.<sup>24</sup> A Cl-bonded As species would be expected to appear at higher binding energy than the position of the observed signal.

#### c) Ga 3d signals

The Ga 3d region showed the removal of most surface oxides as a result of the 6 M HCl(aq) etching procedure. The Ga 3d signal was well-fitted by two peaks representing separate Ga species (figure 4.6). The larger peak, centered at 19.3 eV, is consistent with expectations for bulk Ga(As), while the smaller peak, at 20.7 eV is ascribable to Ga<sub>2</sub>O<sub>3</sub>.<sup>24</sup>

The binding energy of Cl-bonded surface Ga atoms is known to be shifted only 0.35 eV from the bulk Ga 3d peak,<sup>12</sup> a shift significantly less than the energy resolution of the available laboratory XPS instrumentation. Any Ga-Cl surface species are thus expected to appear as part of the bulk peak at 19.3 eV.

Because the particles were deposited on the XPS substrate directly from the aqueous etching solution and dried for several minutes in air, the Ga<sub>2</sub>O<sub>3</sub> was presumably formed by reaction with the residual water present during the preparation of the samples for the XPS experiments. However, it is possible that a small amount of oxide was not

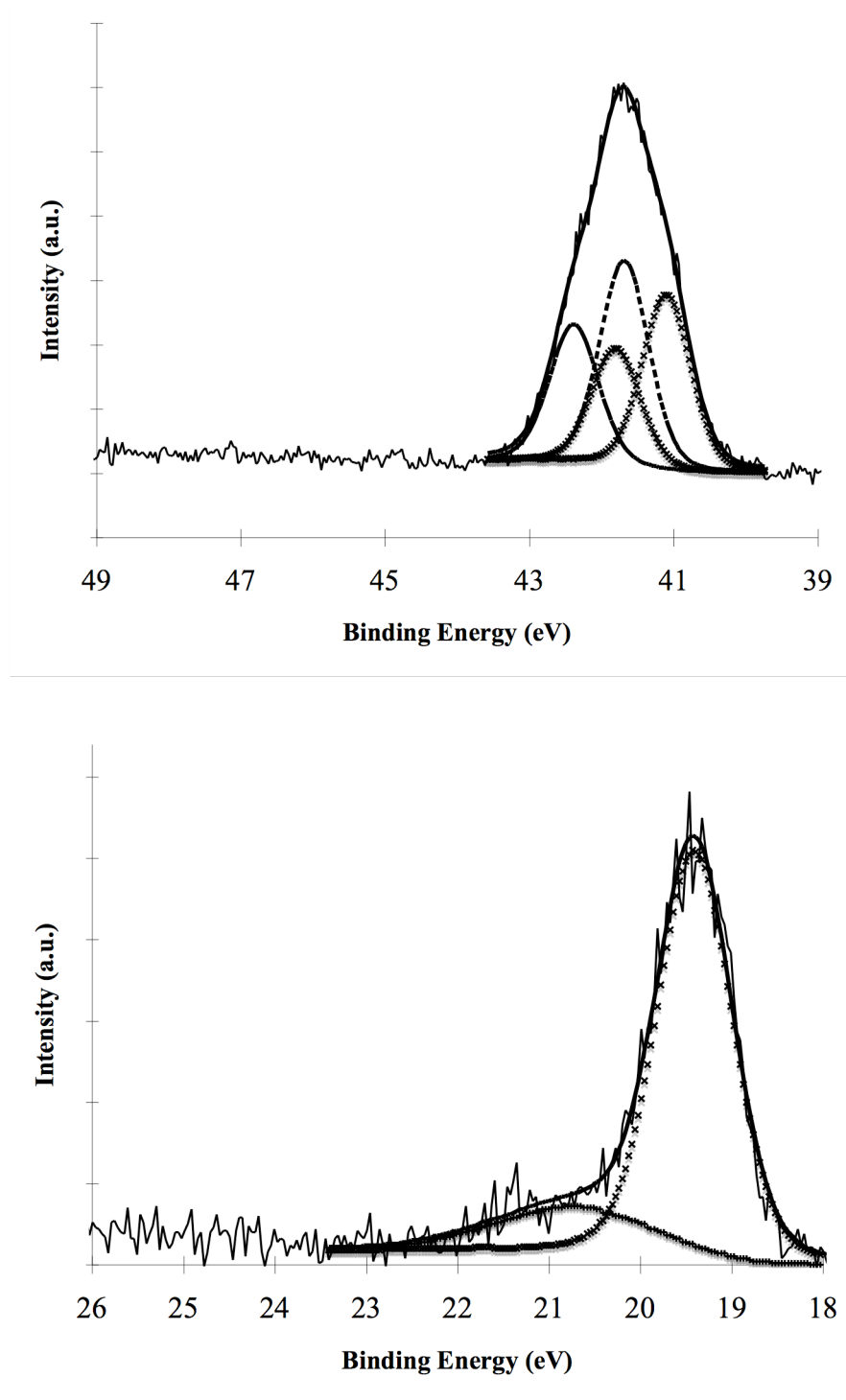


**Figure 4.6.** XPS spectra for Cl-terminated GaAs nanocrystals. Above—As 3d region, fit to doublets representing bulk (Ga)As and  $\text{As}^0$ ; Below—Ga 3d region, fit to peaks representing bulk Ga(As) and  $\text{Ga}_2\text{O}_3$ .

removed during the etching process.

Rinsing the Cl-terminated GaAs particles with a fresh etching solution was necessary before collecting XPS data or performing further functionalization. If the particles were deposited on the Si substrate directly from the original etching solution, another strong peak, centered  $\sim 21.1$  eV, was observed in the Ga 3d region of the XPS data. This peak corresponded to  $\text{Ga}(\text{OH})_3$ ,<sup>12,24</sup> and presumably represented contamination due to Ga hydroxides that were formed during the aqueous etching process.

#### d) Surface Stoichiometry

While equations developed for the determination of overlayer thicknesses on flat surfaces<sup>25</sup> cannot be applied to the nanoparticles, due to surface roughness and shadowing effects,<sup>26,27</sup> the integrated peak areas, corrected for the relevant sensitivity factors  $\sigma$ , can be used to determine relative elemental abundances within the sample depth probed by XPS at the incident photon energy used in data collection. For particles synthesized using an aqueous workup, the ratio of the  $\text{As}^0$  3d<sub>5/2</sub> ( $\sigma = 1.213$ ) peak area to the bulk Ga 3d ( $\sigma = 1.085$ ) peak area was 2.4:1, suggesting a significant excess of elemental arsenic on the nanocrystal surfaces.

There are several possible sources of excess  $\text{As}^0$  in this material. It may be formed during the wet-etching process. Etching of the native oxides on the GaAs(111)A face with the same HCl(aq) solution has been observed to produce  $\text{As}^0$ -free surfaces,<sup>12</sup> but this reaction probably does not proceed as cleanly on other GaAs faces or at step edges. Unreacted As starting material may get trapped in the oxide layer during the aqueous workup step, although no  $\text{As}^0$  lines were observed in the X-ray diffraction

pattern of the oxide-capped particles. Finally, elemental As may be formed at the oxide-GaAs interface during the 350 °C vacuum annealing step of particle purification, by the reaction of GaAs in contact with  $\text{As}_2\text{O}_3$  to form  $\text{Ga}_2\text{O}_3$  and  $\text{As}^0$ .<sup>28</sup>

Use of a methanolic workup in synthesis of the nanoparticles should result in a much thinner oxide layer during the annealing step, and thus produce less  $\text{As}^0$ . Consistently, a bulk Ga to bulk As ratio of 1.3:1 was observed for such particles in the XPS data. This excess of bulk Ga signal is consistent with an etching mechanism that preferentially reveals Ga-rich faces.  $\text{As}^0$  was still observable on this surface, with a  $\text{As}^0$  to (Ga)As ratio of 1.2:1. While this represents a substantial reduction in the amount of elemental As present, such levels of  $\text{As}^0$  are still sufficient to produce a high density of electrical trap sites, if such are associated with the presence of surficial elemental As.

### 4.3.3 Chemical Functionalization of Cl-terminated GaAs Nanocrystals

#### 4.3.3.1 *Hydrazine-Treated Samples*

##### a) X-ray Photoelectron Spectroscopy

After treatment with hydrazine, the Cl 2p peak at 198.7 eV was no longer detectable in the X-ray photoelectron spectrum of the nanocrystals, while a N 1s peak appeared at ~401.5 eV. This N 1s binding energy is consistent with values previously observed for hydrazines on GaAs<sup>29</sup> and Ru<sup>30</sup> surfaces.

No As oxide contaminants were observed even though the samples had been treated with water and acetone after exposure to the hydrazine. The observed As photoemission peak was resolved into two spin-orbit doublets, with the  $3d_{5/2}$  components centered at 41.1 and 41.7 eV, respectively, having an area ratio of 1:2. Hence the surface

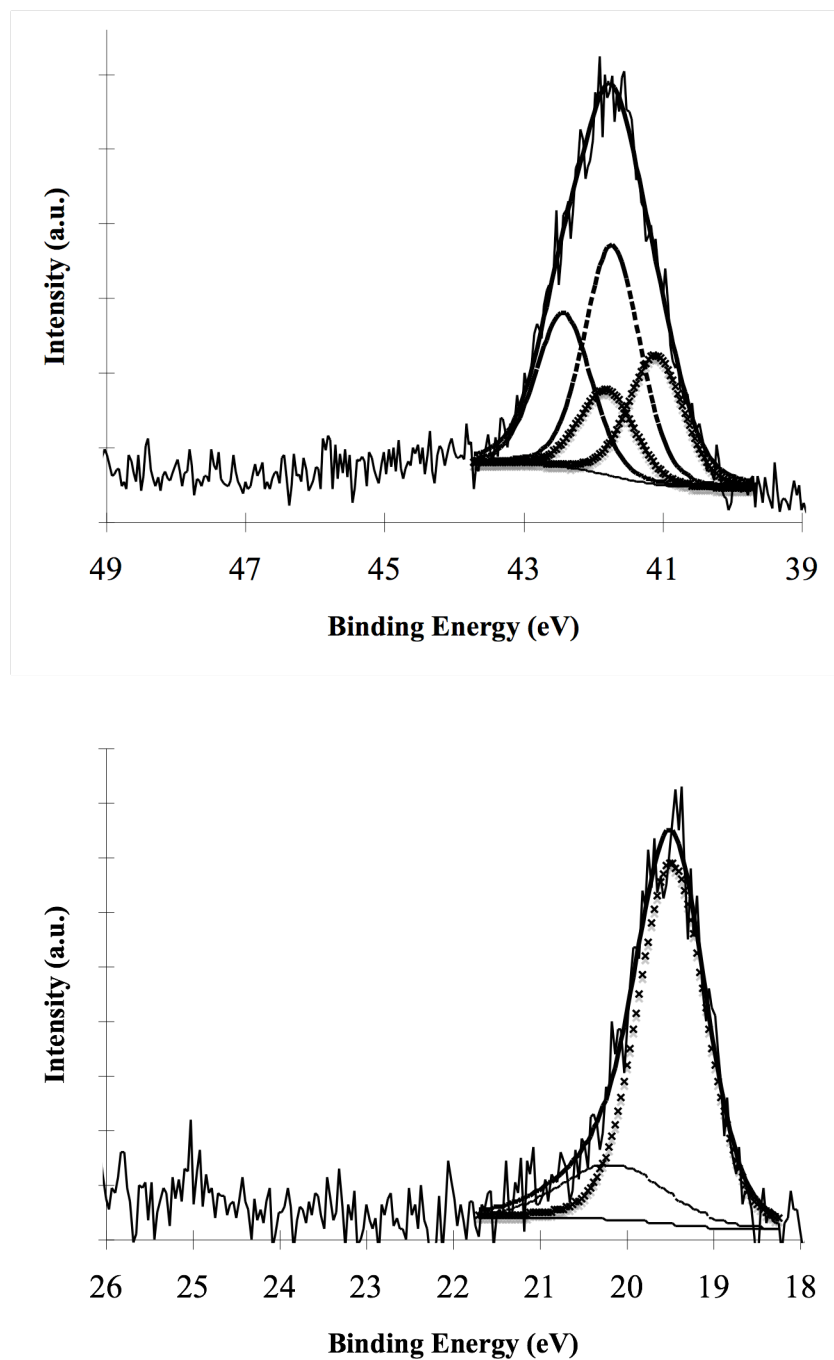


**Figure 4.7.** XPS spectra for  $\text{N}_2\text{H}_4$  functionalized GaAs nanocrystals. Above—As 3d region, fit to doublets representing bulk (Ga)As and  $\text{As}^0$ ; Below—Ga 3d region, fit to peaks representing bulk Ga(As) and  $\text{Ga}_2\text{O}_3$ .

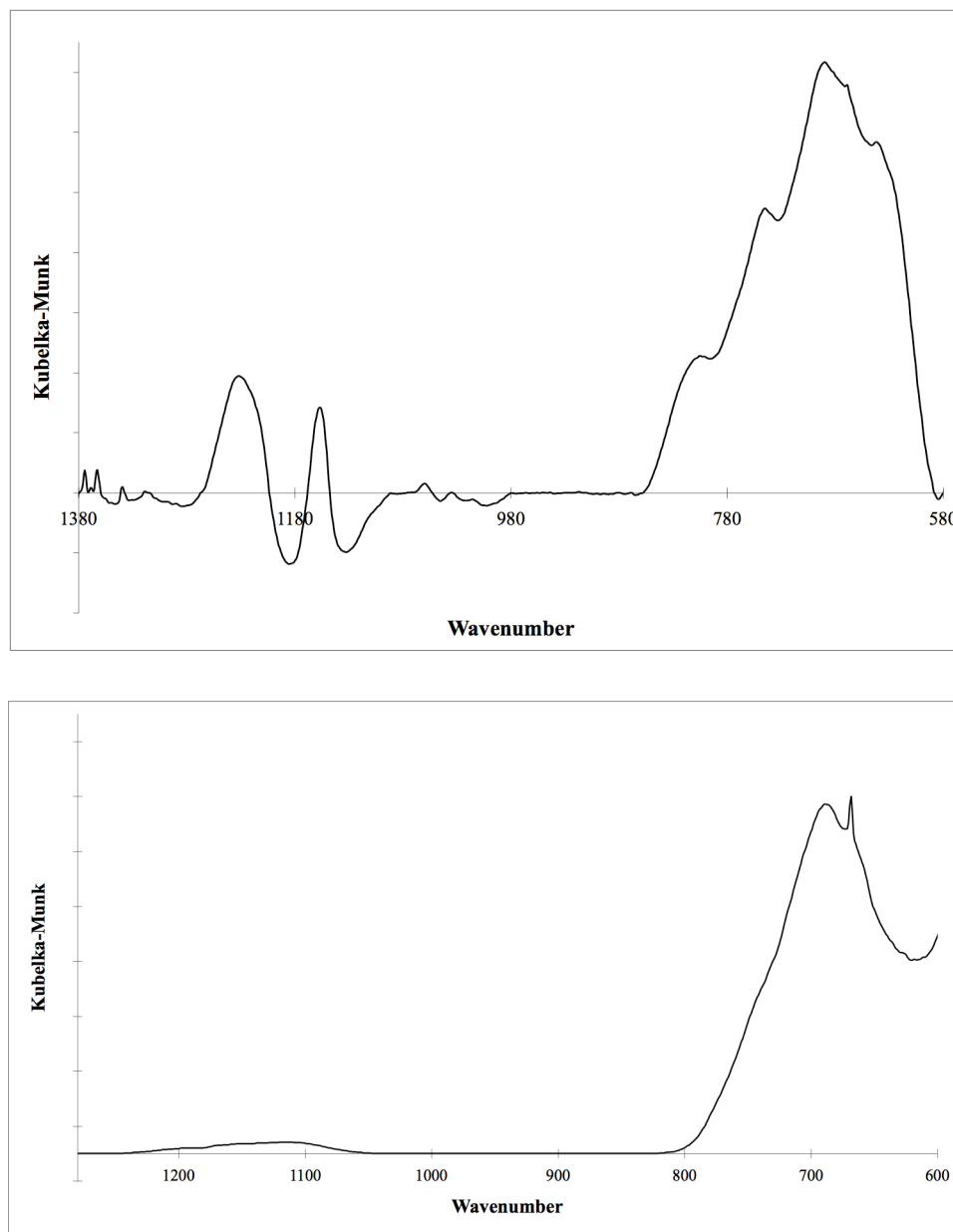


**Figure 4.8.** Diffuse reflectance infrared spectra of hydrazine functionalized GaAs nanocrystals before (above) and after (annealing). Peak assignments are discussed in the text.

of the hydrazine-exposed particles was even more As rich than the surface of the Cl-terminated nanoparticles.

The Ga 3d spectrum of the hydrazine-exposed nanoparticles displayed 2 peaks, a larger bulk emission at 19.5 eV and a smaller component shifted to 20.1 eV (figure 4.7). This latter binding energy is consistent with Ga<sub>2</sub>O, although a contribution from nitrogen-bonded surface Ga atoms is also possible. The bulk-to-surface species intensity ratio was 4.2:1.

#### b) Infrared Spectroscopy

The IR spectra of the hydrazine-capped nanoparticles showed a significant amount of adsorbed water, which obscured observation of N-H stretching bands in the region between ~3200-3300 cm<sup>-1</sup>. Reflectance bands of varying intensity were observed at 1225, 1155, 1090, 800, 737, 685 and 635 cm<sup>-1</sup> (figure 4.8). To help identify these peaks, the Cl-terminated GaAs nanoparticles were functionalized with a 35% wt solution N<sub>2</sub>D<sub>4</sub> in D<sub>2</sub>O. As with N<sub>2</sub>H<sub>4</sub> treated particles, the relative intensity of the peaks showed a fairly wide variance between samples. However, the energies of the peaks in the spectrum were unchanged, with the exception of a new peak that was observed at 1970 cm<sup>-1</sup>. This behavior suggests that these other peaks are due to either N bonded to surface species or are due to other oxide phases that could not be distinguished by XPS. Assignment of these bands is discussed below with the spectra of the annealed surfaces.

#### *4.3.3.2 NaSH-Treated Samples*

Treatment of the Cl-terminated GaAs nanoparticles with NaSH produced similar XPS behavior as that observed following treatment with hydrazine. Specifically, exposure to NaSH led to the disappearance of the Cl 2p peak and the appearance of a S

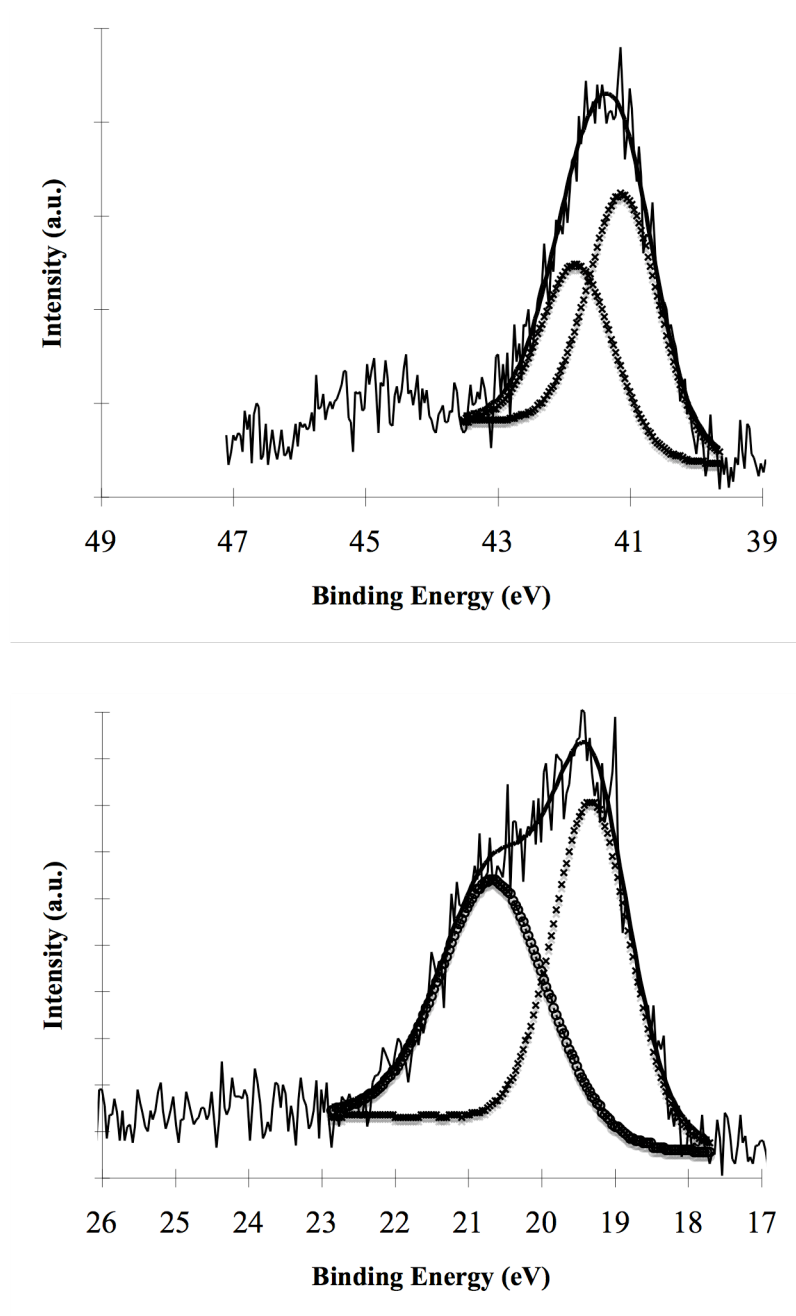


**Figure 4.9.** XPS spectra of  $\text{N}_2\text{H}_4$  functionalized GaAs nanocrystals after annealing under vacuum at  $350\text{ }^\circ\text{C}$ . The As 3d spectrum (above) has been fit to a single doublet corresponding to bulk (Ga)As. A small amount of As oxide is also visible at higher binding energy. The Ga 3d spectrum has been fit to 2 peaks, corresponding to bulk Ga(As) and  $\text{Ga}_2\text{O}_3$ .

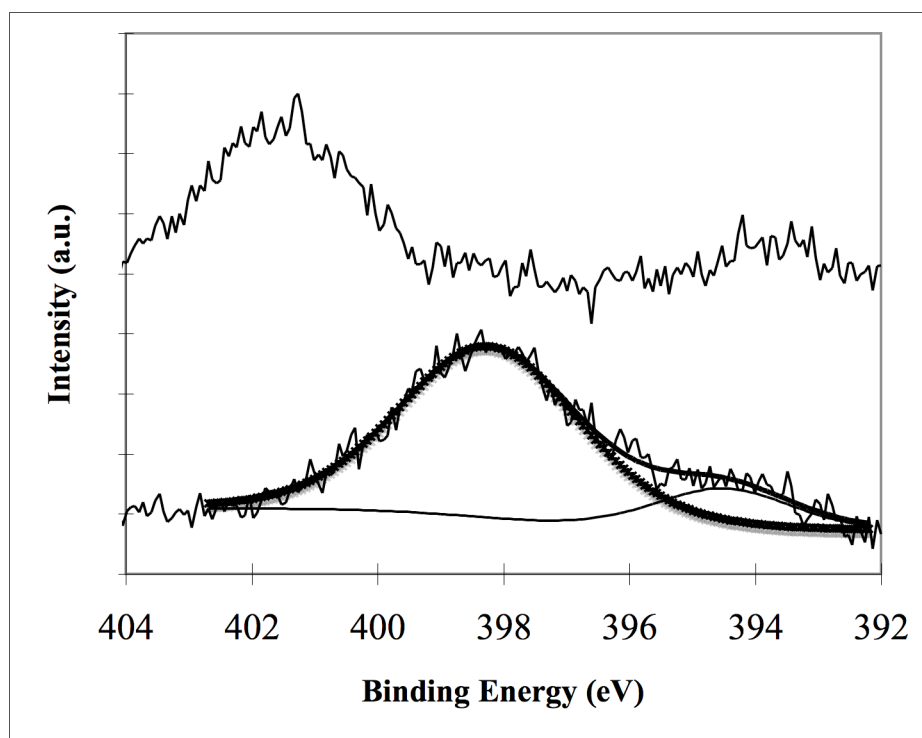


**Figure 4.10.** XPS data for the N 1s region of  $\text{N}_2\text{H}_4$  functionalized GaAs nanocrystals before (upper) and after (lower) annealing. The peak at 394 eV is a Ga Auger line.

2p doublet, with the S 2p<sub>3/2</sub> peak centered at 160 eV. Elemental As was still present in detectable amounts on the SH-exposed surfaces, although the contaminant-to-bulk ratio in the As 3d region was greatly reduced (1:5.3).

#### 4.3.3.3 *Annealed Surfaces*

To remove the elemental As and As-N species from the nanocrystal surfaces, some hydrazine-exposed samples were annealed at 350 °C under vacuum. During the annealing process, black and pale yellow solids collected on the cold finger of the sublimator.

The photoelectron spectra of these samples showed several significant changes that were effected by the annealing step. The As 3d region was well described by only a single doublet, corresponding to the bulk (Ga)As peak at 41.1 eV (figure 4.9). A signal at ~44.7 eV was also visible, but was too small and broad for a reliable fit to be obtained. However, this peak represents some As oxide contamination. The Ga 3d region still contained a bulk peak at 19.3 eV, but the peak at 20.1 eV was replaced by a signal at 20.7 eV. The change in the Ga 3d spectra was accompanied by a shift in the binding energy of the N 1s peak from 401.5 to 398.3 eV (figure 4.10), indicative of the reduction of surface-bound nitrogen. The observed N 1s peak energy is 1.2 eV higher in binding energy than the value of 397.1 eV reported for (Ga)N,<sup>31</sup> and is closer to the values of 398.5 eV for NH<sub>x</sub> (x = 1,2) on GaAs<sup>32</sup> or 397.7 eV for imide on Ru(0001).<sup>30</sup> The bulk Ga to bulk As ratio was observed to be ≈1:1, as expected for the core of the nanocrystals.

Immediately after annealing, the IR spectrum of the particles was dominated by a single, broad reflectance peak at 685 cm<sup>-1</sup>, with a shoulder at 735 cm<sup>-1</sup> (figure 4.8). A small, very broad reflectance centered at ~1100 cm<sup>-1</sup> was also observed. Assignment of

these bands is difficult due to disagreement on the energies of vibrational modes for both hydrazine and GaAs surfaces modified with nitrogen moieties. Previous reflectance IR studies of the nitridation of single-crystal GaAs surfaces with atomic nitrogen reported values of  $1200\text{ cm}^{-1}$  and  $1000\text{ cm}^{-1}$  for a Ga-N stretch and an As-N stretch, respectively.<sup>33</sup> A high resolution electron energy loss spectroscopy (HREELS) study of hydrazine on GaAs(100)-c(8x2) assigned a loss feature at  $1295\text{ cm}^{-1}$  to a Ga-NH<sub>2</sub> stretch,<sup>34</sup> while a similar study of ammonia on GaAs(100)-c(8x2) assigned loss features at 618 and  $985\text{ cm}^{-1}$  to Ga-N stretching and Ga-NH<sub>3</sub> rocking modes, respectively.<sup>35</sup> For NH<sub>3</sub><sup>32</sup> and dimethyl hydrazine<sup>29</sup> on GaAs(100) (4x6), White et al. assigned a HREELS peak at  $844\text{ cm}^{-1}$  to Ga-NH<sub>x</sub> stretching.

Based on the spectra of the oxide-terminated particles, the peak is assigned at  $1225\text{ cm}^{-1}$  to Ga<sub>2</sub>O, and the peaks at  $635$  and  $800\text{ cm}^{-1}$  to contamination from As<sub>2</sub>O<sub>3</sub> in either the Claudetite or amorphous phase. To confirm this assignment, IR spectra were taken of the particles after several weeks of air exposure. Consistent with the XPS results showing some oxide formation, the intensity of these peaks was greatly enhanced. Further, for unannealed samples with excess As at the surface, the spectra of air exposed particles was dominated by the peak at  $800\text{ cm}^{-1}$ , while for the annealed samples this peak was much weaker. The peak at  $737\text{ cm}^{-1}$  is near the value of  $760\text{ cm}^{-1}$  observed for a shoulder in the Ga<sub>2</sub>O<sub>3</sub> spectrum,<sup>21</sup> and is assigned to this species.

Because the peak at  $685\text{ cm}^{-1}$  is so dominant after annealing, it is unlikely to be related to surface As species. This peak is assigned to Ga<sub>2</sub>O<sub>3</sub>, which has previously been observed at  $680\text{ cm}^{-1}$ .<sup>21,22</sup> Peaks at  $1080$  and  $1151\text{ cm}^{-1}$  have been observed during surface IR studies of GaAs(100) modified with Na<sub>2</sub>S, and have been assigned to S-O

stretches,<sup>36</sup> although that assignment is clearly not applicable here. A broad peak at  $1100\text{ cm}^{-1}$  has been observed for Claudetite  $\text{As}_2\text{O}_3$ ,<sup>22</sup> and can be correlated to observed peaks at  $1090$  and  $1100\text{ cm}^{-1}$ . The peak at  $1150\text{ cm}^{-1}$  does not correspond to any known gallium or arsenic oxide modes.

To drive off hydrogen atoms and form a surface capping layer of either terminal nitrides or cubic GaN, the hydrazine-capped nanocrystals were annealed at  $500\text{ }^\circ\text{C}$ . After this higher temperature anneal, the nanocrystals were no longer sufficiently conductive to perform XPS experiments without charge compensation from the electron flood gun. Spectra collected using the flood gun revealed a N 1s peak centered at  $398.4\text{ eV}$ , i.e., virtually unchanged in energy from the peak observed following the lower temperature annealing step.

The annealed nanocrystals showed formation of both Ga and As oxides after 2 weeks in air. The N-capping layer was not stable in the original etching solution, and the photoelectron spectra of reetched nanocrystals showed the disappearance of the N 1s signal and the reappearance of  $\text{As}^0$ .

#### **4.3.4 Photoluminescence of Functionalized GaAs Nanocrystals**

As the size of a semiconductor nanocrystal decreases below its excitonic Bohr radius, the band structure undergoes quantum confinement and the band-gap of the nanocrystal increases.<sup>2</sup> Brus has calculated that GaAs ought to display bulk band-gap behavior down to diameters of  $\approx 19\text{ nm}$ .<sup>2</sup> Based on the size measurements described above, the large majority of our nanocrystals were larger than this size, so their band edge PL should be dominated by emission at the bulk band-gap energy, i.e.,  $1.43\text{ eV}$  ( $869\text{ nm}$ ).

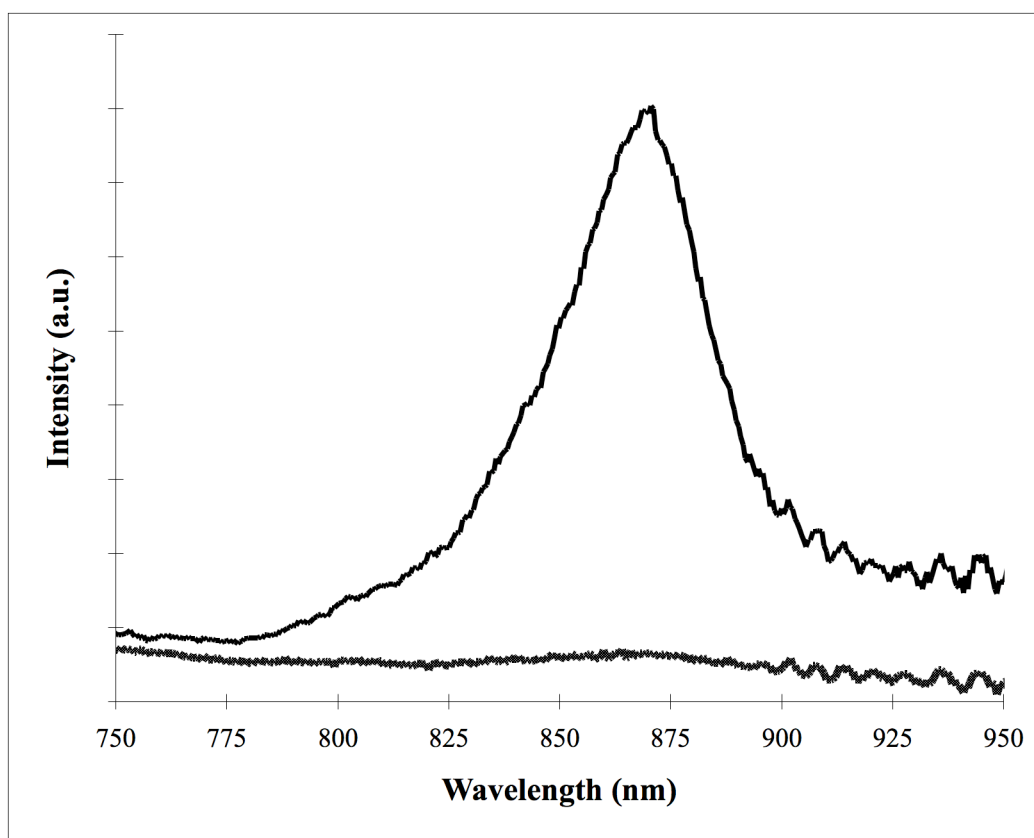


**Figure 4.11.** Steady-state photoluminescence intensity of  $N_2H_4$  functionalized samples before (light trace) and after (dark trace) annealing. No measurable signal was observed from oxide-terminated samples.

For particles dispersed on Si substrates, all of the samples examined displayed broad light scattering peaks centered between 650 and 700 nm. No photoluminescence was observed from the oxide-capped nanocrystals. For nanocrystals etched and treated with either  $\text{N}_2\text{H}_4$  or  $\text{NaSH}$ , a weak PL peak centered at 868 nm was observed. Nanocrystals that were capped and annealed displayed a peak at this wavelength that was more than 40 times more intense than the other samples, suggesting significant suppression of surface trap states (figure 4.11). The PL intensity of these particles did not degrade even after several weeks in air, despite the fact the XPS revealed the formation of some surface oxides.

For particles dispersed in  $\text{CH}_3\text{OH}$ , photoluminescence was observed only from particles that had been  $\text{N}_2\text{H}_4$  capped and annealed. However, when the GaAs nanoparticles were subsequently dispersed on Si, all but the as-prepared oxide capped particles photoluminesced to at least some extent. Therefore, this reduced PL signal is likely due to either increased scattering or to a solution quenching process rather than chemical degradation by  $\text{CH}_3\text{OH}$ . The fact that the  $\text{N}_2\text{H}_4$  treated and annealed particles still showed significant PL under these conditions makes them an especially promising candidate for photoelectrochemical applications.

#### **4.4 Conclusions**

Oxide-terminated GaAs nanocrystals have been chemically synthesized and etched to yield nanocrystals with Cl-terminated surfaces. These reactive surfaces have been used as platforms for further functionalization with hydrazine or sodium hydrosulfide. The surfaces of Cl, hydrazine and hydrosulfide capped nanocrystals all

contain significant amounts of As contaminants and only display very weak band edge PL. Annealing the functionalized nanocrystals under vacuum removes the excess As, and in the case of the hydrazine functionalized particles, leads to decomposition of  $N_2H_4$  into terminal  $NH_2$  or  $NH$  species. The band edge PL of these particles is strongly enhanced after this annealing step, confirming both that elemental As is an important electronic trap state for GaAs nanocrystals and that this functionalization chemistry effectively reduces the density of surface carrier traps.

**References**

- (1) Afzaal, M.; O'Brien, P. *Journal Of Materials Chemistry* **2006**, *16*, 1597.
- (2) Brus, L. E. *Journal of Chemical Physics* **1984**, *80*, 4403.
- (3) Shockley, W.; Queisser, H. J. *Journal of Applied Physics* **1961**, *32*, 510.
- (4) Esteves, A. C. C.; Trindade, T. *Current Opinion in Solid State & Materials Science* **2002**, *6*, 347.
- (5) Masala, O.; Seshadri, R. *Annual Review of Materials Research* **2004**, *34*, 41.
- (6) Salata, O. V.; Dobson, P. J.; Hull, P. J.; Hutchison, J. L. *Applied Physics Letters* **1994**, *65*, 189.
- (7) Sercel, P. C.; Saunders, W. A.; Atwater, H. A.; Vahala, K. J.; Flagan, R. *C. Applied Physics Letters* **1992**, *61*, 696.
- (8) Malik, M. A.; O'Brien, P.; Norager, S.; Smith, J. *Journal of Materials Chemistry* **2003**, *13*, 2591.
- (9) Uchida, H.; Curtis, C. J.; Nozik, A. J. *Journal of Physical Chemistry* **1991**, *95*, 5382.
- (10) Lu, Z. H.; Chatenoud, F.; Dion, M. M.; Graham, M. J.; Ruda, H. E.; Koutzarov, I.; Liu, Q.; Mitchell, C. E. J.; Hill, I. G.; McLean, A. B. *Applied Physics Letters* **1995**, *67*, 670.
- (11) Lu, Z. H.; Tyliczszak, T.; Hitchcock, A. P. *Physical Review B* **1998**, *58*, 13820.
- (12) Traub, M. C.; Biteen, J. S.; Michalak, D. J.; Webb, L. J.; Brunshwig, B. S.; Lewis, N. S. *Journal of Physical Chemistry B*. **2006**, *110*, 15641.

- (13) Tarui, Y.; Komiya, Y.; Harada, Y. *Journal of the Electrochemical Society* **1971**, *118*, 118.
- (14) Kher, S. S.; Wells, R. L. *Chemistry of Materials* **1994**, *6*, 2056.
- (15) Eisler, H. J.; Sundar, V. C.; Bawendi, M. G.; Walsh, M.; Smith, H. I.; Klimov, V. *Applied Physics Letters* **2002**, *80*, 4614.
- (16) Colvin, V. L.; Schlamp, M. C.; Alivisatos, A. P. *Nature* **1994**, *370*, 354.
- (17) Bansal, A.; Li, X. L.; Yi, S. I.; Weinberg, W. H.; Lewis, N. S. *Journal of Physical Chemistry B* **2001**, *105*, 10266.
- (18) Webb, L. J.; Lewis, N. S. *Journal of Physical Chemistry B* **2003**, *107*, 5404.
- (19) Klug, H. P.; Alexander, L. E. *X-ray Diffraction Procedures For Polycrystalline and Amorphous Materials*, 2nd ed.; John Wiley & Sons: New York, 1974.
- (20) Hagan, C. R. S.; Kher, S. S.; Halaoui, L. I.; Wells, R. L.; Coury, L. A. *Analytical Chemistry* **1995**, *67*, 528.
- (21) Vilar, M. R.; El Beghdadi, J.; Debontridder, F.; Artzi, R.; Naaman, R.; Ferraria, A. M.; do Rego, A. M. B. *Surface and Interface Analysis* **2005**, *37*, 673.
- (22) Palik, E. D.; Ginsburg, N.; Holm, R. T.; Gibson, J. W. *Journal of Vacuum Science & Technology* **1978**, *15*, 1488.
- (23) Flynn, E. J.; Solin, S. A.; Papatheodorou, G. N. *Physical Review B* **1976**, *13*, 1752.
- (24) Surdu-Bob, C. C.; Saied, S. O.; Sullivan, J. L. *Applied Surface Science* **2001**, *183*, 126.

- (25) Seah, M. P. Quantification of AES and XPS. In *Practical Surface Analysis*; 2nd ed.; Briggs, D., Seah, M. P., eds.; John Wiley & Sons: Chichester, 1990; vol. 1; pp 201.
- (26) Martin-Concepcion, A. I.; Yubero, F.; Espinos, J. P.; Tougaard, S. *Surface And Interface Analysis* **2004**, *36*, 788.
- (27) Sanchez-Lopez, J. C.; Fernandez, A. *Surface and Interface Analysis* **1998**, *26*, 1016.
- (28) Thurmond, C. D.; Schwartz, G. P.; Kammlott, G. W.; Schwartz, B. *Journal of the Electrochemical Society* **1980**, *127*, 1366.
- (29) Sun, Y. M.; Sloan, D. W.; McEllistrem, M.; Schwaner, A. L.; White, J. M. *Journal of Vacuum Science & Technology A—Vacuum Surfaces and Films* **1995**, *13*, 1455.
- (30) Truong, C. M.; Rodriguez, J. A.; Goodman, D. W. *Journal of Physical Chemistry* **1992**, *96*, 341.
- (31) Hedman, J.; Martensson, N. *Physica Scripta* **1980**, *22*, 176.
- (32) Zhu, X. Y.; Wolf, M.; Huett, T.; White, J. M. *Journal of Chemical Physics* **1992**, *97*, 5856.
- (33) Yamauchi, Y.; Uwai, K.; Kobayashi, N. *Japanese Journal of Applied Physics Part 2—Letters* **1996**, *35*, L80.
- (34) Apen, E.; Gland, J. L. *Surface Science* **1994**, *321*, 308.
- (35) Apen, E.; Gland, J. L. *Surface Science* **1994**, *321*, 301.
- (36) Yota, J.; Burrows, V. A. *Journal of Vacuum Science & Technology a-Vacuum Surfaces and Films* **1993**, *11*, 1083.

## Chapter 5

# Relationships Between Nonadiabatic Bridged Intramolecular, Electrochemical, and Electrical Electron-Transfer Processes

### 5.1 Introduction

Interest in “molecular electronics” has stimulated comparisons between various types of interfacial charge-transfer rate processes.<sup>1-7</sup> Specifically, it would be useful to readily relate the rate of an intramolecular electron-transfer process between a donor (D) and acceptor (A) linked by a bridging group (B) to the current density in a “molecular wire” system in which the same moiety B acts as a bridging group in a monomolecular layer between two metal electrodes. Additional rate processes of interest occur when the same molecular species B acts as a bridge between a scanning tunneling microscopy (STM) tip or a conductive atomic force microscopy (AFM) tip and a metal electrode, or when moiety B acts as a bridge between a metal electrode and a redox-active species in a self-assembled monolayer.

The formalism for evaluating rates of nonadiabatic intramolecular electron transfer between donors and acceptors linked by molecular bridges is well understood

within a semiclassical electronic coupling theory.<sup>8,9</sup> In contrast, the rates of electron transfer through tunneling barriers between two conductors are conventionally interpreted within a Landauer formalism.<sup>10</sup> In this chapter, a relatively simple method for semi-quantitatively relating these various rate constants is presented. This approach ought to be of use to experimentalists interested in formulating expectations for current densities through molecular wires, given measured rate constants and electronic coupling values for analogous bridging species in intramolecular electron-transfer processes.

## 5.2 Theoretical Approach

### 5.2.1 General Rate Expressions

Fermi's Golden Rule yields the probability for nonadiabatic electron transfer from an electronic state  $i$  of the reactant's precursor complex to an electronic state  $j$  of the product's successor complex:

$$W_{DA}(i, j) = \frac{4\pi^2}{h} H_{DA}^2(i, j) \sum_{\nu_r, \nu_p} f(\nu_{r,i}) FC_{\nu_r, i, \nu_p, j} \quad (5.1)$$

where  $\nu_r$  and  $\nu_p$  are the vibrational quantum numbers for the reactants and products, respectively,  $FC_{\nu_r, i, \nu_p, j}$  is the Franck-Condon factor representing the overlap integral of the vibrational wavefunctions of the  $i^{\text{th}}$  electronic state of the reactants,  $\nu_{r,i}$ , with the vibrational wavefunctions of the  $j^{\text{th}}$  electronic state of the products,  $\nu_{p,i}$ ,  $f(\nu_{r,i})$  is the probability that state  $\nu_{r,i}$  is occupied,  $H_{DA}(i, j)$  is the electronic coupling matrix element between the  $i^{\text{th}}$  donor and  $j^{\text{th}}$  acceptor sites, and  $h$  is Planck's constant.<sup>11-14</sup> The summation of the Franck-Condon factors can be viewed as a weighted density of vibrational states for the donor-acceptor pair when only one electronic state of the reactants and one of the

products contributes to the rate. Only those vibrational modes whose equilibrium nuclear configuration changes with electron transfer contribute to the sum.

When the energy spacing between electronic states of the donor and/or the acceptor is small, the total probability of electron transfer,  $W_{\text{DA}}$ , becomes the summation of the rates between all the specific states that contribute to the electron transfer. This is similar to the generalization of the rate constant for electron transfer when a number of vibration modes are important, except a Boltzmann weighting of the states is not assumed and different states can have a different electronic coupling matrix element.<sup>15</sup>

Generalizing eq 5.1 therefore produces:

$$W_{\text{DA}} = \frac{4\pi^2}{h} \sum_{i,j} H_{\text{DA}}^2(i,j) \sum_{\nu_r, \nu_p} f(i\nu_r) FC_{i\nu_r, j\nu_p} \quad (5.2)$$

When the spacing of the electronic levels can be treated as a continuum of states, the summation can be replaced by an integral with a density of states per energy function,  $\rho$ :

$$W_{\text{DA}} = \frac{4\pi^2}{h} \int_{-\infty}^{\infty} \int_{-\infty}^{\infty} \{H'_{\text{DA}}(\mathbf{E}_r, \mathbf{E}_p)\}^2 \rho_r(\mathbf{E}_r) f(\mathbf{E}_r) FC(\mathbf{E}_r, \mathbf{E}_p) \rho_p(\mathbf{E}_p) g(\mathbf{E}_p) d\mathbf{E}_r d\mathbf{E}_p \quad (5.3)$$

where  $\rho_r(\mathbf{E}_r)$  and  $\rho_p(\mathbf{E}_p)$  are the density of states (i.e., the states per unit energy) of the reactants and products at energy  $\mathbf{E}_r$  and  $\mathbf{E}_p$  respectively,  $f(\mathbf{E}_r)$  is the probability that a reactant in state  $\nu_{r,i}$  (or energy  $\mathbf{E}_r$ ) is occupied, and  $g(\mathbf{E}_p)$  is the probability that a product in state of  $\nu_{p,j}$  (or energy  $\mathbf{E}_p$ ) is unoccupied. The probability  $g(\mathbf{E}_p)$  of a product state being unoccupied has been introduced because the integral is over all of the levels of the product but only unoccupied product states contribute to the electron transfer process.

When only the donor has closely spaced electronic levels then only the lowest unoccupied level of the acceptor is important, and eq (5.3) reduces to:

$$W_{DA} = \frac{4\pi^2}{h} \int_{-\infty}^{\infty} \rho_r(\mathbf{E}_r) f(\mathbf{E}_r) \{H'_{DA}(\mathbf{E}_r, \mathbf{E}_p)\}^2 FC(\mathbf{E}_r, \mathbf{E}_p) d\mathbf{E}_r \quad (5.4)$$

If the vibrational modes can be treated classically, the probability ( $s^{-1}$ ) of electron transfer between states  $i$  and  $j$  can be written as

$$W_{DA}(i, j) = \frac{4\pi^2}{h} H_{DA}^2(i, j) \left( \frac{1}{4\pi k_B T \lambda_{DA}} \right)^{1/2} e^{-\left[ \frac{(\Delta G_{ij}^0 + \lambda_{DA})^2}{4\lambda_{DA} k_B T} \right]} \quad (5.5)$$

where  $H_{DA}(i, j)$  is the overall matrix element that couples each individual donor and acceptor,  $\lambda_{DA}$  is the nuclear reorganization energy for the donor-acceptor system,  $k_B$  is Boltzmann's constant,  $\Delta G^0$  is the standard free-energy change for the electron-transfer process from the donor species to the acceptor species and  $T$  is the temperature in K.

Alternatively when both the donor or acceptor have closely spaced electronic levels, but neither has vibrational levels that are active in the electron transfer (i.e. levels that have a change their equilibrium nuclear configuration between the reactants and products) then the Franck-Condon factor reduces to a delta function,

$FC(\mathbf{E}_r, \mathbf{E}_p) = \delta(\mathbf{E}_r - \mathbf{E}_p)$ , insuring energy conservation during the electron transfer.<sup>15</sup> The probability of electron transfer is then given by:

$$\begin{aligned} W_{DA} &= \frac{4\pi^2}{h} \int_{-\infty}^{\infty} \int_{-\infty}^{\infty} \{H'_{DA}(\mathbf{E}_r, \mathbf{E}_p)\}^2 \rho_r(\mathbf{E}_r) f(\mathbf{E}_r) \delta(\mathbf{E}_r - \mathbf{E}_p) \rho_p(\mathbf{E}_p) g(\mathbf{E}_p) d\mathbf{E}_r d\mathbf{E}_p \\ &= \frac{4\pi^2}{h} \int_{-\infty}^{\infty} \{H'_{DA}(\mathbf{E})\}^2 \rho_r(\mathbf{E}) f(\mathbf{E}) \rho_p(\mathbf{E}) g(\mathbf{E}) d\mathbf{E} \end{aligned} \quad (5.6)$$

The experimentally observed rate for a collection of donors and acceptors in a macroscopic system of interest is obtained by summing the individual microscopic

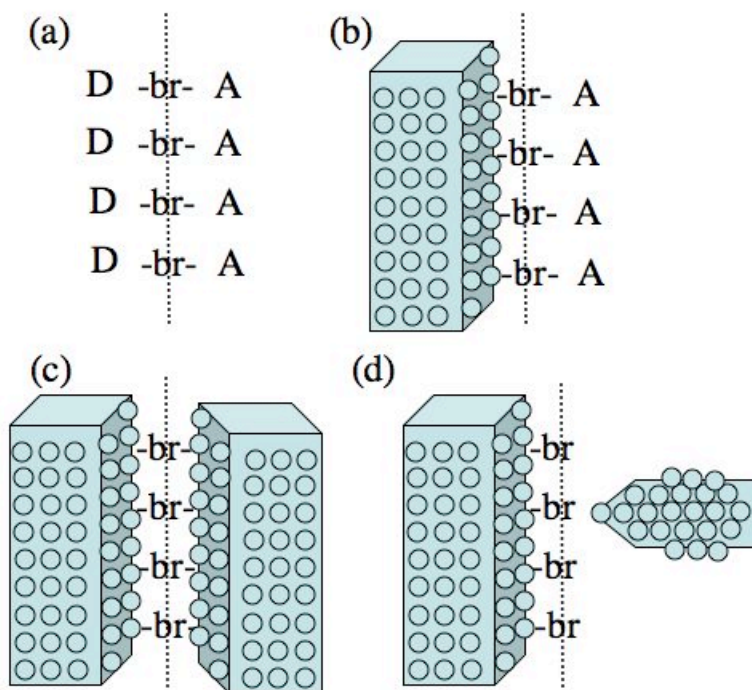
electron-transfer probabilities for all the donors and acceptors in the active volume of the experimental system:

$$\begin{aligned} \text{rate}_{\text{DA}} &= \frac{4\pi^2}{h} \int_{\mathcal{V}_A} \int_{\mathcal{V}_D} \int_{\mathbf{E}_r} \int_{\mathbf{E}_p} G_{\mathcal{V}_A} G_{\mathcal{V}_D} W_{\text{DA}} \mathcal{V}_D d\mathcal{V}_A \\ &= \frac{4\pi^2}{h} \int_{\mathcal{V}_A} \int_{\mathcal{V}_D} \int_{\mathbf{E}_r} \int_{\mathbf{E}_p} G_{\mathcal{V}_A} G_{\mathcal{V}_D} \{H'_{\text{DA}}(\mathbf{E}_r, \mathbf{E}_p)\}^2 \rho_r(\mathbf{E}_r) f(\mathbf{E}_r) FC(\mathbf{E}_r, \mathbf{E}_p) \rho_p(\mathbf{E}_p) g(\mathbf{E}_p) d\mathbf{E}_r d\mathbf{E}_p d\mathcal{V}_D d\mathcal{V}_A \end{aligned} \quad (5.7)$$

where  $G_{\mathcal{V}_A}$  and  $G_{\mathcal{V}_D}$  are the distribution functions of donors and acceptors, respectively, in the volumes of interest (donors or acceptors per unit volume).

The experimentally observed rate is a sum of the forward (from D to A) and reverse (from A to D) rates. When the reaction is between a donor and acceptor that have a net free-energy change ( $\Delta G < 0$ ), the forward direction (D to A) will dominate the observed rate. Hence, for these cases we only consider the rate in one direction (see sections 5.2.2 and 5.2.3). However, when the reaction is near equilibrium ( $\Delta G \approx 0$ ), both directions need to be considered, as described in the situation discussed in sections 5.2.4 and 5.2.5.

In this work, the rate of electron transfer will be evaluated across an imaginary boundary plane of area,  $\mathcal{A}$ , positioned midway along the molecular bridging species B (Scheme 5.1). The donor volume integral is over the region  $\mathcal{V}_D$ , to the left of the boundary plane, while the acceptor integral is over the region  $\mathcal{V}_A$ , to the right side of the boundary plane (Scheme 5.1). Both regions have a cross-sectional area of  $\mathcal{A}$ . In each system of interest, evaluation of the net electron-transfer rate therefore involves integrations over all of the occupied states of the reactants and unoccupied electronic states of the product that participate in the electron-transfer process.



**Scheme 5.1.** a—Intramolecular electron transfer from a collection of donor-bridge-acceptor units comprised of donors (D) linked covalently to acceptors (A) by a bridging molecular unit (br). The volume occupied by donors,  $\mathcal{V}_D$ , is on the left side of the bridge while the volume occupied by acceptors,  $\mathcal{V}_A$ , is on the right side of the bridge. The number density of molecules is  $\Gamma_{DA}$  over the cross-sectional area  $\mathcal{A}$ . b—Electron transfer from a metal to a monolayer of acceptors (A) at a fixed distance from the electrode, established by a bridging molecular unit (br) covalently attached to the electrode. The effective density of states in the metal is evaluated on left side of the bridge, while the volume occupied by acceptors is evaluated on the right side of the bridge. The number density of molecules is  $\Gamma_A$  over the cross-sectional area  $\mathcal{A}$ . c—Electron transfer through a monomolecular bridge layer from a metal on the left side of the bridge to a second metal on the right side of the bridge. The effective density of states of one metal is evaluated in

the volume  $\mathcal{V}_A$ , to the left of the bridge, while the effective density of states of the other metal is evaluated in the volume,  $\mathcal{V}_A$ , to the right side of the bridge. The number density of bridge units is  $\Gamma_B$  over the cross-sectional area  $\mathcal{A}$ . d—Electron transfer to a metallic STM tip or to a metal-coated AFM tip from a metal covered by a monolayer of a bridging molecular species (br). The effective density of states of the metal is evaluated on the left side of the bridge, while the effective density of states in the tip is evaluated to the right side of the bridge.

When the donors and acceptors are connected by a bridge of length  $l$ , assuming that bridged pairs have coordinates that differ only in  $z$ , then the functions take on the form:

$$G_{\varphi_A} G_{\varphi_D} = \Gamma_{DA} \delta(x_A - x_D) \delta(y_A - y_D) \delta(z_A + l - z_D) \delta(z_A - l/2) \quad (5.8)$$

where  $\Gamma_{DA}$  is the number density of donor/acceptor pairs per unit area, and the spatial functions,  $\delta(x)$ ,  $\delta(y)$ , and  $\delta(z)$ , are delta functions.

### 5.2.2 Intramolecular Donor-Bridge-Acceptor Electron Transfer

For a system composed of two molecular species joined by a bridge, in general, the large energy spacing between molecular electronic states of the donor and acceptor implies that only one reactant and one product electronic state per D-A pair contributes to the rate of electron transfer. The double integration over energy of eq (5.1) thus yields a single value for the total electronic coupling between the reactant and product,  $H_{DBA}$ . Following the approach of eq (5.7), the net macroscopic rate of electron transfer for a collection of such bridged D-A pairs can therefore be written as:

$$rate_{DBA} = \frac{4\pi^2}{h} \left( \frac{1}{4\pi k_B T \lambda_{DBA}} \right)^{1/2} e^{-\left\{ \frac{(\Delta G_{DBA}^o + \lambda_{DBA})^2}{4\lambda_{DBA} k_B T} \right\}} \iint_{\varphi_D, \varphi_A} H_{DBA}^2 G_{\varphi_A} G_{\varphi_D} d\varphi_A d\varphi_D \quad (5.9)$$

where the subscripts “DBA” have been used to specifically denote the situation for electron transfer between D and A through the bridging moiety B.

Because the electron transfer only occurs between a donor and acceptor connected by a bridge, the volume integration counts the number of bridged pairs. Thus, using eq (5.8) produces:

$$\begin{aligned}
& \iint G_{\varphi_D} G_{\varphi_A} d\mathcal{V}_A d\mathcal{V}_D \\
&= \iint G_{\varphi_D}(z_D) G_{\varphi_A}(z_A) \delta(x_D - x_A) \delta(y_D - y_A) \delta(z_D + \ell - z_A) \delta(z_A + \ell/2) d\mathcal{V}_A d\mathcal{V}_D \quad (5.10) \\
&= \Gamma_{DA} \mathcal{A}
\end{aligned}$$

The value of  $H_{DBA}$  is a function of the distance between the donor and acceptor. However, for a bridged system, the donor/acceptor distance is fixed and the coupling element can thus be removed from the volume integrals. The integration of eq (5.9) over volume therefore yields:

$$rate_{DBA} = \frac{4\pi^2}{h} \left( \frac{I}{4\pi k_B T \lambda_{DBA}} \right)^{1/2} \{H_{DBA}^b\}^2 e^{-\left\{ \frac{(\Delta G_{DBA}^o + \lambda_{DBA})^2}{4\lambda_{DBA} k_B T} \right\}} \Gamma_{DA} \mathcal{A} \quad (5.11)$$

where the notation  $H_{DBA}^b$  indicates that the coupling must be evaluated at the distance of the bridge.

The rate law for this intramolecular process is given by  $rate_{DBA} = k_{DBA} \Gamma_{DA} \mathcal{A}$ , with  $k_{DBA}$  the rate constant for the reaction. The expression for  $k_{DBA}$  is thus:

$$k_{DBA} = \frac{4\pi^2}{h} \left( \frac{I}{4\pi k_B T \lambda_{DBA}} \right)^{1/2} \{H_{DBA}^b\}^2 e^{-\left\{ \frac{(\Delta G_{DBA}^o + \lambda_{DBA})^2}{4\lambda_{DBA} k_B T} \right\}} \quad (5.12)$$

Rearranging eq 5.12 to solve for  $\{H_{DBA}^b\}^2$  yields:

$$\{H_{DBA}^b\}^2 = \frac{h}{4\pi^2} (4\pi k_B T \lambda_{DBA})^{1/2} e^{\left\{ \frac{(\Delta G_{DBA}^o + \lambda_{DBA})^2}{4\lambda_{DBA} k_B T} \right\}} k_{DBA} \quad (5.13)$$

### 5.2.3 Metal Electrode-Bridge-Molecular Acceptor Electron Transfer

The rate of electron transfer from a metal electrode through a bridge to an attached electron acceptor (Scheme 5.1b) can be expressed similarly. The initial states of the electron are the donor states in the continuum of the metal electrode, and the Frank-

Condon overlap now only has contributions from the acceptor species. Hence, the probability of an electron transfer is given by eq (5.4), with the Franck-Condon terms being treated as described in eq (5.5). The rate is a function of the potential,  $E$ , of the electrode relative to a reference potential, and is given by:<sup>16-19</sup>

$$rate_{MBA}(E) = \frac{4\pi^2}{h} \left( \frac{1}{4\pi k_B T \lambda_{MBA}} \right)^{1/2} \iint_{\vartheta_m \vartheta_A} \int_{-\infty}^{\infty} G_{\vartheta_A} G_{\vartheta_m} \{H_{MBA}(\mathbf{E})\}^2 \cdot \rho_A(\mathbf{E}) F(\mathbf{E}, E) \rho_m(\mathbf{E}) e^{\left\{ \frac{-[(\mathbf{E}+qE^{o'})+\lambda_{MBA}]^2}{4\lambda_{MBA}k_B T} \right\}} d\mathbf{E} d\vartheta_A d\vartheta_m \quad (5.14)$$

where  $E^{o'}(A/A^-)$  (abbreviated generally herein as  $E^{o'}$ ) is the formal potential of the  $A/A^-$  redox couple,  $q$  is the unsigned charge on an electron, and  $F(\mathbf{E}, E)$  is the Fermi occupation probability for the metal at energy  $\mathbf{E}$  as a function of the electrode potential,  $E$ :<sup>16-19</sup>

$$F(\mathbf{E}, E) = \frac{1}{1 + e^{\frac{(\mathbf{E}+qE)}{k_B T}}} \quad (5.15)$$

The quantity  $\{H_{MBA}(\mathbf{E})\}^2$  in eq (5.14) represents the square of the matrix element that couples reactant and product states at  $\mathbf{E}$ , averaged over all degenerate states in the metal having an energy  $\mathbf{E}$  in a plane parallel to the solid/liquid interface. The value of  $H_{MBA}^2(\mathbf{E})$  has units of  $\text{eV}^2 \text{state}^{-1}$ . Note that the electrode potentials and system energies are measured relative to the same reference level, with the relationship between the energy and the potential of a given redox couple represented as  $\mathbf{E}(A/A^-) = -qE(A/A^-)$ , with  $q$  unsigned.

To evaluate the distribution functions, we note that the integration over volume to the right side of the boundary,  $\vartheta_A$ , must account for the number of acceptor molecules attached to the bridge. The distance from the reference plane to the acceptors is fixed, so

the electronic coupling can be taken out of the integral. Realizing that each acceptor only contributes one electronic state per molecule,  $\rho_A = 1$ , to the electron-transfer process

yields  $\int_{\mathcal{V}_A} H_{MBA}^2 G_A \rho_A d\mathcal{V}_A = H_{MBA}^2 \Gamma_A \mathcal{A}$  where  $\Gamma_A$  is the number density of acceptors per unit

area. The expression for the electron-transfer rate then becomes:

$$\begin{aligned} \text{rate}_{MBA}(E) = \frac{4\pi^2}{h} \left( \frac{1}{4\pi k_B T \lambda_{MBA}} \right)^{1/2} \Gamma_A \mathcal{A} \int_{\mathcal{V}_M} \int_{E=-\infty}^{\infty} \{H_{MBA}(\mathbf{E})\}^2 \cdot \\ F(\mathbf{E}, E) \{G_{\mathcal{V}_m} \rho_m\} e^{\left\{ \frac{-[-(\mathbf{E}+qE^o) + \lambda_{MBA}]^2}{4\lambda_{MBA} k_B T} \right\}} d\mathbf{E} d\mathcal{V}_m \end{aligned} \quad (5.16)$$

The integration over the volume of the metal electrode,  $\mathcal{V}_m$ , gives:

$$\rho_{m,\text{eff}}(\mathbf{E}) = \int G_{\mathcal{V}_m} \rho_m(\mathbf{E}) d\mathcal{V}_m \quad (5.17)$$

where  $\rho_{m,\text{eff}}(\mathbf{E})$  is the effective number of states in the metal that contribute to the electron transfer (states  $\text{eV}^{-1}$ ).

For most metals, the state density,  $\eta_m$  (in states  $\text{cm}^{-3}$ ), at the Fermi level of the metal can readily be estimated by application of the Drude free electron gas model.<sup>20</sup>

Taking the state density  $\eta_m$  at the Fermi level of the metal and dividing by the Fermi energy,  $\mathbf{E}_f$ , yields:

$$D_m = \frac{3}{2} \left( \frac{\eta_m(\mathbf{E}_f)}{\mathbf{E}_f} \right) \quad (5.18)$$

Here  $D_m$  (states  $\text{eV}^{-1} \text{cm}^{-1}$ ) is assumed to be approximately independent of energy.<sup>20</sup> The number of states per atom per eV in the metal is obtained by dividing the density of states of a metal,  $D_m$  by the atomic density of the solid,  $d_m$  (atoms  $\text{cm}^{-3}$ ).

However, only a certain fraction of these states will be effective in facilitating the interfacial charge-transfer event. This fraction is  $l_m/\delta_m$ , where  $l_m$  (in cm) is the effective

coupling length of the bridge wavefunction into the metal, and  $\delta_m$  is the average diameter of an atom in the metal lattice (in units of cm atom<sup>-1</sup>). Hence, for the charge-transfer process, the effective density of states per unit energy of the metal,  $\rho_{m,\text{eff}}$ , is:

$$\rho_{m,\text{eff}} = \frac{D_m}{d_m} \frac{l_m}{\delta_m} \approx D_m l_m \left( \frac{\pi}{6d_m^2} \right)^{1/3} = D_m l_m \delta_m^2 \frac{\pi}{6} \quad (5.19)$$

For gold,  $\delta_m \approx 3 \text{ \AA}$ . Assuming that the effective coupling length is comparable to  $\delta_m$  yields  $\rho_{m,\text{eff}} \approx 0.27 \text{ states eV}^{-1}$ .<sup>18</sup>

Substituting eq (5.17) into eq (5.16) yields:

$$\text{rate}_{\text{MBA}}(E) = \frac{4\pi^2}{h} \left( \frac{1}{4\pi k_B T \lambda_{\text{MBA}}} \right)^{1/2} \Gamma_A \mathcal{A} \int_{E=-\infty}^{\infty} \left\{ H_{\text{MBA}}^b(\mathbf{E}) \right\}^2 \cdot \rho_{m,\text{eff}}(\mathbf{E}) F(\mathbf{E}, E) e^{\left\{ \frac{-[(\mathbf{E}+qE^{o'})+\lambda_{\text{MBA}}]^2}{4\lambda_{\text{MBA}} k_B T} \right\}} d\mathbf{E} \quad (5.20)$$

Because the rate across the surface  $\mathcal{A}$  is given by  $k_{\text{MBA}} \Gamma_A \mathcal{A}$ , where  $k_{\text{MBA}}$  is the rate constant at an applied potential of  $E$ , one obtains the expression for  $k_{\text{MBA}}(E)$ :

$$k_{\text{MBA}}(E) = \frac{4\pi^2}{h} \left( \frac{1}{4\pi k_B T \lambda_{\text{MBA}}} \right)^{1/2} \int_{-\infty}^{\infty} \left\{ H_{\text{MBA}}^b(\mathbf{E}) \right\}^2 \cdot \rho_{m,\text{eff}}(\mathbf{E}) F(\mathbf{E}, E) e^{\left\{ \frac{-[(\mathbf{E}+qE^{o'})+\lambda_{\text{MBA}}]^2}{4\lambda_{\text{MBA}} k_B T} \right\}} d\mathbf{E} \quad (5.21)$$

The electronic coupling,  $H_{\text{MBA}}$ , is assumed to decrease exponentially with the distance.

The coupling at the nominal distance from the acceptor through the bridge to the electrode surface is denoted as  $H_{\text{MBA}}^b$ .

Assuming that  $H_{\text{MBA}}^b$  and  $D_m$  (or  $\rho_{m,\text{eff}}$ ) are independent of energy allows the rewriting of eq (5.21) as:

$$k_{\text{MBA}}(E) = \frac{4\pi^2}{h} \rho_{m,\text{eff}} \left\{ H_{\text{MBA}}^b(E) \right\}^2 I(\lambda_{\text{MBA}}, E) \quad (5.22)$$

with the integral  $I(\lambda_{\text{MBA}}, E)$  defined as:

$$I(\lambda_{\text{MBA}}, E) = \left( \frac{I}{4\pi k_B T \lambda_{\text{MBA}}} \right)^{1/2} \int_{-\infty}^{\infty} F(\mathbf{E}, E) e^{\left\{ \frac{-[(\mathbf{E} + qE^{o'}) + \lambda_{\text{MBA}}]^2}{4\lambda_{\text{MBA}} k_B T} \right\}} d\mathbf{E} \quad (5.23)$$

The integral  $I(\lambda_{\text{MBA}}, E)$  represents the overlap between the Fermi distribution function and the Gaussian function that contains the free-energy dependence of the Franck-Condon-weighted density of vibrational states for the electron transfer. As the potential of the electrode is made more negative, the Fermi level of the electrode shifts closer to the vacuum level, and the overlap increases and  $I(\lambda_{\text{MBA}}, E)$  approaches 1. When the potential of the electrode becomes more positive the overlap decreases and  $I(\lambda_{\text{MBA}}, E)$  approaches 0. The value of  $I(\lambda_{\text{MBA}}, E)$  at any electrode potential is generally known from independent measurements of  $\lambda$  or from a fit of the experimentally measured dependence of the interfacial charge-transfer rate constant on  $E$ .<sup>16</sup> Hence, the expressions for  $k_{\text{MBA}}(E)$  (eq (5.21) or (5.22)) and  $k_{\text{DBA}}$  (eq 5.12) can be compared:

$$\begin{aligned} \frac{k_{\text{MBA}}}{k_{\text{DBA}}} &= (4\pi k_B T \lambda_{\text{DBA}})^{1/2} \frac{\{H_{\text{MBA}}^b(\mathbf{E})\}^2}{\{H_{\text{DBA}}^b\}^2} \left[ \left( \frac{\pi}{6} \right)^{1/3} \frac{D_m l_m}{d_m^{2/3}} \right] \frac{I(\lambda_{\text{MBA}}, E)}{e^{\left\{ \frac{(\Delta G_{\text{DBA}}^o + \lambda_{\text{DBA}})^2}{4\lambda_{\text{DBA}} k_B T} \right\}}} \\ &= \left( \frac{\lambda_{\text{DBA}}}{\lambda_{\text{MBA}}} \right)^{1/2} \frac{\{H_{\text{MBA}}^b(\mathbf{E})\}^2}{\{H_{\text{DBA}}^b\}^2} \left[ \left( \frac{\pi}{6} \right)^{1/3} \frac{D_m l_m}{d_m^{2/3}} \right] \times \\ &\quad \frac{\int_{-\infty}^{\infty} F(\mathbf{E}, E) e^{\left\{ \frac{-[(\mathbf{E} + qE^{o'}) + \lambda_{\text{MBA}}]^2}{4\lambda_{\text{MBA}} k_B T} \right\}} d\mathbf{E}}{e^{\left\{ \frac{(\Delta G_{\text{DBA}}^o + \lambda_{\text{DBA}})^2}{4\lambda_{\text{DBA}} k_B T} \right\}}} \end{aligned} \quad (5.24)$$

For the MBA system, when  $E < E^{o'}$ , the observed rate is dominated by the rate of reduction of the acceptor, with negligible contribution from the reverse rate of oxidation of the donor by the electrode. Extrapolation of the rate constant measured at these

potentials to the value at equilibrium yields an expression for the rate constant at zero driving force. Extrapolation of the rate constant measured at these potentials to the value at equilibrium yields an expression for the rate constant at zero driving force. The value at  $E = E^{0'}$  ( $A/A'$ ) yields an expression for the standard rate constant at zero driving force,  $k_{MBA}^0$ :

$$k_{MBA}^0 = \frac{4\pi^2}{h} \rho_{m,eff} \{H_{MBA}^b(\mathbf{E})\}^2 I(\lambda_{MBA}, E^{0'}) \quad (5.25)$$

$$\begin{aligned} I(\lambda_{MBA}, E^{0'}) &= \left( \frac{I}{4\pi k_B T \lambda_{MBA}} \right)^{1/2} \int_{-\infty}^{\infty} \frac{e^{\left\{ \frac{[-(\mathbf{E} + qE^{0'}) + \lambda_{MBA}]^2}{4\lambda_{MBA} k_B T} \right\}}}{1 + e^{\frac{(\mathbf{E} + qE^{0'})}{k_B T}}} d\mathbf{E} \\ &= \left( \frac{I}{4\pi k_B T \lambda_{MBA}} \right)^{1/2} \int_{-\infty}^{\infty} \frac{e^{\left\{ \frac{[\lambda_{MBA} - \varepsilon]^2}{4\lambda_{MBA} k_B T} \right\}}}{1 + e^{\varepsilon/k_B T}} d\varepsilon \end{aligned} \quad (5.26)$$

where  $\varepsilon = (\mathbf{E} + qE^{0'})$ . In the integral, the Fermi function goes to zero for

$\varepsilon \gg 0$ , ( $\mathbf{E} \gg -qE^{0'}$ ), and the Gaussian is a maximum at  $\varepsilon = \lambda_{MBA}$ . Significant overlap only occurs for values of  $\varepsilon$  close to 0. Expanding the exponential and dropping the quadratic term then yields:

$$I(\lambda_{MBA}, E^{0'}) \approx \left( \frac{I}{4\pi k_B T \lambda_{MBA}} \right)^{1/2} e^{\left[ \frac{\lambda_{MBA}}{4k_B T} \right]} \int_{-\infty}^{\infty} \frac{d\varepsilon}{e^{(-\varepsilon/2k_B T)} + e^{(\varepsilon/2k_B T)}} \quad (5.27)$$

The integral in eq (5.27) is equal to  $\approx \pi k_B T$ ,<sup>21</sup> thus yielding:

$$I(\lambda_{MBA}, E^{0'}) \approx \left( \frac{\pi k_B T}{4\lambda_{MBA}} \right)^{1/2} e^{\left[ \frac{\lambda_{MBA}}{4k_B T} \right]} \quad (5.28)$$

Hence the approximate value of the standard rate constant when  $E = E^{0'}$  is:

$$k_{MBA}^0 = \frac{2\pi^2}{h} \{H_{MBA}^b(\mathbf{E})\}^2 \left( \frac{\pi k_B T}{\lambda_{MBA}} \right)^{1/2} \rho_{m,eff} e^{\left[ \frac{\lambda_{MBA}}{4k_B T} \right]} \quad (5.29)$$

Solving for  $H_{\text{MBA}}^2$  yields:

$$\{H_{\text{MBA}}^{\text{b}}(\mathbf{E})\}^2 = \frac{h}{2\pi^2} \left( \frac{\lambda_{\text{MBA}}}{\pi k_{\text{B}} T} \right)^{1/2} \rho_{\text{m,eff}} e^{\left[ \frac{\lambda_{\text{MBA}}}{4 k_{\text{B}} T} \right]} k_{\text{MBA}}^0 \quad (5.30)$$

#### 5.2.4 Metal Electrode-Bridge-Metal Electrode Electron Transfer

A parallel methodology can be applied to evaluate the current density between two metal electrodes linked by a monomolecular layer of bridging moieties (Scheme 5.1c). Starting with eq (5.6) for the probability of electron transfer, the forward rate is given by:

$$\text{rate}_{\text{MBM}}(V) = \frac{4\pi^2}{h} \iint_{\varphi_{\text{L}}, \varphi_{\text{R}}} G_{\varphi_{\text{L}}} G_{\varphi_{\text{R}}} \left\{ \int_{-\infty}^{\infty} \{H_{\text{MBM}}(\mathbf{E})\}^2 F(\mathbf{E}, E_{\text{L}}) \rho_{\text{r}}(\mathbf{E}) [1 - F(\mathbf{E}, E_{\text{R}})] \rho_{\text{p}}(\mathbf{E}) d\mathbf{E} \right\} d\varphi_{\text{L}} d\varphi_{\text{R}} \quad (5.31)$$

The probability that an acceptor state is unoccupied is given by  $1 - F(\mathbf{E}, E_{\text{R}})$ , the applied voltage,  $V$ , is equal to the potential difference between the two metals (i.e.,  $V = E_{\text{R}} - E_{\text{L}}$ ), and the density of states for the reactants (products) is simply the value for the metal on the left (right),  $\rho_{\text{r}} = \rho_{\text{m,L}}$  ( $\rho_{\text{p}} = \rho_{\text{m,R}}$ ).

Proceeding as previously, we define  $\rho_{\text{m,eff},i}(\mathbf{E}) \propto \int G_{\varphi_i} \rho_{\text{m},i} d\varphi_i$ , where  $i$  denotes the case for either  $i = \text{L}$  or  $i = \text{R}$ , that is, the metal on the left or the metal on the right side of the boundary plane,  $\mathcal{A}$ . The expression for evaluation of  $\rho_{\text{m,eff}}$  presented in eq (5.19) is appropriate for describing  $\rho_{\text{m,eff}}$  for each metal involved in the electron-transfer process. The metals are held apart at a fixed distance by the bridges and the rate is dependent on the number of bridges in the volume,  $\Gamma_{\text{B}} \mathcal{A}$ , with  $\Gamma_{\text{B}}$  being the number density of the bridges of interest. Hence:

$$\Gamma_B \mathcal{A} \rho_{m,eff,R} \rho_{m,eff,L} = \int_{\mathcal{E}_L} G_{\mathcal{E}_L} \rho_{mr} d\mathcal{H}_L \int_{\mathcal{E}_R} G_{\mathcal{E}_R} \rho_{mp} d\mathcal{H}_R \quad (5.32)$$

yielding a rate of:

$$rate_{MBM}(V) = \frac{4\pi^2}{h} \{H_{MBM}^b\}^2 \rho_{m,eff,R} \rho_{m,eff,L} \Gamma_B \mathcal{A} \int_{-\infty}^{\infty} F(\mathbf{E}, E_L) [1 - F(\mathbf{E}, E_R)] d\mathbf{E} \quad (5.33)$$

where  $H_{MBM}^b$  has been averaged over all energies that contribute to the rate.

The integral is the overlap between the probability that the states in the left electrode are occupied and the probability that the states in the right electrode are unoccupied. When  $E_L$  is more positive than  $E_R$  ( $V_L < V_R$ ) the overlap is large, because both functions have values of 1 for energies between  $E_L$  and  $E_R$ . As  $E_L$  becomes more negative (or  $E_R$  more positive), the overlap increases linearly. Alternatively, when  $E_L$  is more negative than  $E_R$ , the overlap is small. Integrating over energy, and expressing the Fermi functions in terms of the potential difference,  $V$ , between the two electrodes yields:

$$rate_{MBM}(V) = \frac{4\pi^2}{h} \{H_{MBM}^b\}^2 \rho_{mL,eff} \rho_{mR,eff} \frac{qV}{1 - e^{-qV/k_B T}} \Gamma_B \mathcal{A} \quad (5.34)$$

At positive values of  $qV$  (positive driving force) the rate for driving forces of  $>2k_B T$  is linear in  $qV$ . In contrast, for negative values of  $qV$ , the rate becomes exponential in  $qV$ :

$$rate_{MBM}(V) = \frac{4\pi^2}{h} \{H_{MBM}^b\}^2 \rho_{mL,eff} \rho_{mR,eff} qV e^{qV/k_B T} \Gamma_B \mathcal{A} \quad (\text{for } V < 0) \quad (5.35)$$

The forward current density per bridge,  $J_{B,f}$ , at the electrode is defined as:

$$J_{B,f} = q \frac{rate_{MBM}(V)}{\Gamma_B \mathcal{A}} \quad (5.36)$$

The back current density,  $J_{B,b}$ , is given by the same expression except that the sign of  $V$  is reversed. Thus the total current density per bridge,  $J_B$ , is given by:

$$J_B = J_{B,f} - J_{B,b} = \frac{q}{\Gamma_B} (\text{rate}_{\text{MBM}}(V) - \text{rate}_{\text{MBM}}(-V)) \quad (5.37)$$

The low-bias charge-transfer resistance per bridge,  $R_{\text{MBM}}$ , is the inverse of the slope of the current density,  $J_B$ , vs.  $V$  plot near  $V = 0$ , i.e.,  $(dJ_B/dV|_{\Delta V=0})^{-1}$ . Taking the derivative of eq (5.37)<sup>22</sup> yields:

$$R_{\text{MBM}} = \left( \frac{4\pi^2}{h} q^2 \{H_{\text{MBM}}^b\}^2 \rho_{\text{mL,eff}} \rho_{\text{mR,eff}} \right)^{-1} \quad (5.38)$$

Solving for  $H_{\text{MBM}}^b$  yields:

$$\{H_{\text{MBM}}^b\}^2 = \frac{h}{4\pi^2 q^2} \frac{1}{\rho_{\text{mL,eff}} \rho_{\text{mR,eff}}} \cdot R_{\text{MBM}}^{-1} \quad (5.39)$$

## 5.2.5 Electron Transfer Between a STM Tip and a Molecularly Coated Metal

### Electrode

The formalism can also be used to evaluate the current density through a single molecule bridging between a metal electrode and either a STM tip or a conductive AFM tip (Scheme 5.1d), upon application of a voltage difference,  $V$ , between the metal and the tip. In a completely parallel fashion to eq (5.31), one obtains:

$$\text{rate}_{\text{MBT}}(V) = \frac{4\pi^2}{h} \iint_{\mathcal{V}_m, \mathcal{V}_t} G_{\mathcal{V}_m} G_{\mathcal{V}_t} \left\{ \int_{-\infty}^{\infty} \{H_{\text{MBT}}(\mathbf{E})\}^2 F(\mathbf{E}, E_m) \rho_t(\mathbf{E}) [1 - F(\mathbf{E}, E_t)] \rho_p(\mathbf{E}) d\mathbf{E} \right\} d\mathcal{V}_m d\mathcal{V}_t \quad (5.40)$$

where the subscripts  $m$  and  $t$  refer to the metal electrode and the metal tunneling tip, respectively, with the metal assumed to be on the left-hand side and the tip on the right-hand side of the boundary (Scheme 5.1d). The volume integrals are evaluated as above (eq (5.32)); however, the integration volume in this equation only includes a single bridge., so  $\Gamma_B = 1$ . Defining

$$\rho_{i,\text{eff}} = \int G_{\varphi_i} \rho_i d\mathcal{H}_i \quad (5.41)$$

for the metal and the tip, assuming that the densities of states are independent of energy and assuming that there is only one bridge in the volume of interest, yields the integral over energy as in eq (5.34), which in turn produces:

$$\text{rate}_{\text{MBT}}(V) = \frac{4\pi^2}{h} \{H_{\text{MBT}}^b\}^2 \left\{ \frac{qV}{1 - e^{-\frac{qV}{k_B T}}} \right\} \rho_{\text{m,eff}} \rho_{\text{t,eff}} \quad (5.42)$$

Accounting for the forward and reverse rates yields:

$$J_B = J_{B,f} - J_{B,b} = \frac{q}{\Gamma_B \mathcal{A}} (\text{rate}_{\text{MBM}}(V) - \text{rate}_{\text{MBM}}(-V)) \quad (5.43)$$

We then obtain:

$$R_{\text{MBM}} = \left( \frac{4\pi^2}{h} q^2 \{H_{\text{MBM}}^b\}^2 \rho_{\text{mL,eff}} \rho_{\text{mR,eff}} \right)^{-1} \quad (5.44)$$

$$\{H_{\text{MBM}}^b\}^2 = \frac{h}{4\pi^2 q^2} \frac{1}{\rho_{\text{mL,eff}} \rho_{\text{mR,eff}}} \cdot R_{\text{MBM}}^{-1} \quad (5.45)$$

The coupling into the tip is to a single atom. Because the coupling to the surface only includes a single atom, the expression developed earlier for the effective density of states, eq (5.19), can be used to evaluate  $\rho_{\text{m,eff}}$ . It should be noted that the use of the density of states term implies that this is a single atom of bulk material, not a single isolated atom.

### 5.2.6 Rate Relationships Derived from the Above Expressions

To derive the desired relationships between the various processes of interest, we will assume that the electronic coupling per state,  $H^2$ , is the same for each system having a common bridge. Thus, using eq (5.19) for the effective density of states, eqs (5.13), (5.30), (5.39), and (5.45), which all yield expressions for  $H^2$ , can be set to be equal to

each other, producing the following relatively simple relationships between the rate constants and charge-transfer resistances of interest. Significant deviations from these relationships can be taken as an indication of a significant difference between the electronic coupling through the bridge in an intramolecular system relative to the other types of systems being evaluated, presumably due to coupling between the bridge and the metal contacts. The key expressions are given below, with terms in braces related to the nuclear factors in the molecular-based electron-transfer processes, and with the terms in brackets related to the differences in the effective densities of states involved in the various electron-transfer systems:

$$\begin{aligned}
 k_{\text{DBA}} \frac{h}{4\pi^2} \left\{ (4\pi k_{\text{B}} T \lambda_{\text{DBA}})^{1/2} e^{\left[ \frac{(\Delta G^\circ + \lambda_{\text{DBA}})^2}{4\lambda_{\text{DBA}} k_{\text{B}} T} \right]} \right\} &= \\
 k_{\text{MBA}}^0 \left\{ \frac{h}{2\pi^2} \left( \frac{\lambda_{\text{MBA}}}{\pi k_{\text{B}} T} \right)^{1/2} e^{\left[ \frac{\lambda_{\text{MBA}}}{4k_{\text{B}} T} \right]} \right\} \left[ \left( \frac{6}{\pi D_{\text{m}} l_{\text{m}} \delta_{\text{m}}^2} \right) \right] &= \quad (5.46) \\
 R_{\text{MBM}}^{-1} \frac{h}{4\pi^2 q^2} \left[ \left( \frac{36}{\pi^2} \right) \frac{1}{D_{\text{m}1} l_{\text{m}1} \delta_{\text{m}1}^2 D_{\text{m}2} l_{\text{m}2} \delta_{\text{m}2}^2} \right] &= \\
 R_{\text{MBT}}^{-1} \left( \frac{h}{4\pi^2 q^2} \right) \left[ \left( \frac{36}{\pi^2} \right) (D_{\text{m}} D_{\text{t}} l_{\text{m}} l_{\text{t}} \delta_{\text{m}}^2 \delta_{\text{t}}^2)^{-1} \right] &=
 \end{aligned}$$

These equations and terms are summarized in Table 5.1.

**Table 5.1:** Rate constants and electronic coupling matrix elements for systems considered

System	Rate Constant (standard)	$H_{AB}^2$
DBA <sup>11-14</sup>	$k_{DBA} = \frac{4\pi^2}{h} \left( \frac{I}{4\pi k_B T \lambda_{DBA}} \right)^{1/2} \{H_{DBA}^b\}^2 e^{-\left[ \frac{(\Delta G_{DBA}^0 + \lambda_{DBA})^2}{4\lambda_{DBA} k_B T} \right]}$	$\frac{h}{4\pi^2} (4\pi k_B T \lambda_{DBA})^{1/2} e^{-\left[ \frac{(\Delta G_{DBA}^0 + \lambda_{DBA})^2}{4\lambda_{DBA} k_B T} \right]} k_{DBA}$
MBA	$k_{MBA}(E) = \frac{4\pi^2}{h} \rho_{m,eff} \{H_{MBA}^b(\mathbf{E})\}^2 I(\lambda_{MBA}, E)$	$\frac{h}{4\pi^2} k_{MBA}(E) (\rho_{m,eff} I(\lambda_{MBA}, E))^{-1}$
	$I(\lambda_{MBA}, E) = \left( \frac{I}{4\pi k_B T \lambda_{MBA}} \right)^{1/2} \int_{-\infty}^{\infty} F(\mathbf{E}, E) e^{-\left[ \frac{-I(\mathbf{E} + qE^0) + \lambda_{MBA}}{4\lambda_{MBA} k_B T} \right]^2} d\mathbf{E}$	
MBA (standard)	$k_{MBA}^0 = \frac{2\pi^2}{h} \{H_{MBA}^b(\mathbf{E})\}^2 \left( \frac{\pi k_B T}{\lambda_{MBA}} \right)^{1/2} \rho_{m,eff} e^{-\left[ \frac{\lambda_{MBA}}{4k_B T} \right]}$	$\frac{h}{2\pi^2} \left( \frac{\lambda_{MBA}}{\pi k_B T} \right)^{1/2} \frac{1}{\rho_{m,eff}} e^{-\left[ \frac{\lambda_{MBA}}{4k_B T} \right]} k_{MBA}^0$
MBM	$R_{MBM} = \left( \frac{4\pi^2 q^2}{h} \{H_{MBM}^b\}^2 \rho_{mL,eff} \rho_{mR,eff} \right)^{-1}$	$\frac{h}{4\pi^2 q^2} \frac{1}{\rho_{mL,eff} \rho_{mR,eff}} \cdot R_{MBM}^{-1}$
MBT	$R_{MBT} = \left( \frac{4\pi^2 q^2}{h} \{H_{MBT}^b\}^2 \rho_{m,eff} \rho_{t,eff} \right)^{-1}$	$\frac{h}{4\pi^2 q^2} \frac{1}{\rho_{m,eff} \rho_{t,eff}} \cdot R_{MBT}^{-1}$

### 5.3. Application to Experimental Systems of Interest

#### 5.3.1 Tunneling Through Alkane Linkers

The expressions above can be used to relate, on a consistent basis, numerous electron-transfer processes that have been reported to date. We first consider tunneling through multimethylene chains, which have been investigated as bridges in several different types of electron-transfer processes. The value of  $k_{MBA}^0$  has been measured as  $3.4 \times 10^4 \text{ s}^{-1}$  for a carboxylatoferrrocenium acceptor linked through a  $-(\text{CH}_2)_8\text{-S-}$  bridge to a Au electrode.<sup>23</sup> The reorganization energy of this M-B-A system, deduced from Arrhenius plots in the temperature range 15-55 °C, was reported to be  $\lambda = 0.96 \text{ eV}$ . For gold,  $D_m = 1.6 \times 10^{22} \text{ states cm}^{-3} \text{ eV}^{-1}$ , and hence  $\rho_m = 0.27 \text{ states atom}^{-1} \text{ eV}^{-1}$ . With  $l_m \approx 3 \times 10^{-8} \text{ cm}$ , approximately one atom of depth into the metal is effective in the coupling process, yielding a total effective density of states of approximately  $0.27 \text{ states eV}^{-1}$ . Using these values in eq (5.30) produces  $H_{MBA}^2 = 1 \times 10^{-6} \text{ eV}^2 \text{ state}^{-1}$  for this system. For a ferrocenium acceptor directly attached to the same  $(\text{CH})_2\text{-S-}$  bridge, the reported values of  $k_{MBA}^0 = 4.4 \times 10^5 \text{ s}^{-1}$  and  $\lambda = 1.00 \text{ eV}^{24}$  yield a predicted  $H_{MBA}^2$  of  $2 \times 10^{-5} \text{ eV}^2 \text{ state}^{-1}$ .

For a bridge having the same electronic coupling per state as that of the Au-S(CH<sub>2</sub>)<sub>8</sub>-linked carboxylatoferrrocene M-B-A system, eq (5.38) predicts a value of  $R_{MBM} = 9 \times 10^9 \text{ } \Omega$  for tunneling between two Au electrodes, while eq (5.44) predicts the same zero-bias resistance between a Au electrode and STM tip. The predicted resistance for this same bridge derived from the directly linked ferrocene acceptor is  $4 \times 10^8 \text{ } \Omega$ . Poirier and Tarlov have reported a resistance of  $R_{MBT} \sim 1 \times 10^{11} \text{ } \Omega$  for tunneling between a STM tip and a Au electrode coated with a self-assembled monolayer of  $-\text{S}(\text{CH}_2)_7\text{CH}_3$ .<sup>25</sup>

The  $k_{MBA}^0$  ( $1 \times 10^4 \text{ s}^{-1}$ ) and  $\lambda$  (0.91 eV) values measured for the carboxylatoferrocenium acceptor bridged by  $-\text{S}(\text{CH}_2)_9-$  to a Au electrode<sup>23</sup> leads, from eq (5.44), to a predicted Au-bridge-tip low-bias resistance of  $R_{\text{MBT}} = 5 \times 10^{10} \Omega$ , while those measured for a ferrocenium acceptor directly linked to the same bridge<sup>24</sup> predict  $R_{\text{MBT}} = 2 \times 10^9 \Omega$ . These values are significantly larger than the resistance of  $R_{\text{MBT}} \approx 5 \times 10^8 \Omega$  that has been measured between a Au conductive AFM tip and a Au electrode coated with a self-assembled monolayer of  $-\text{S}(\text{CH}_2)_8\text{CH}_3$ .<sup>26</sup> These discrepancies indicate differences between the coupling at the bridge-Fc interfaces and the bridge-tip interfaces. Consistently, first principles calculations of transport through molecular bridges have shown changes of several orders of magnitude in currents due to relatively small changes in interface contacts.<sup>27</sup> It should also be noted that the reported resistances for  $-\text{S}(\text{CH}_2)_8\text{S}-$  moieties acting as *covalently* bound bridges between a Au electrode and a Au STM tip range from  $R_{\text{MBT}} = 5 \times 10^7 \Omega$  to  $R_{\text{MBT}} = 9 \times 10^8 \Omega$ .<sup>28,29</sup> In addition, a value of  $R = 5 \times 10^7 \Omega$  has been measured for 1,8-octanedithiol acting as a bridge across a Au break junction.<sup>30</sup>

### 5.3.2 Tunneling Through Oligonucleotides

Electron transfer through oligonucleotides has been investigated by numerous groups.<sup>31-33</sup> Lewis and co-workers have probed the quenching of excited states of dyes linked to DNA hairpins.<sup>33,34</sup> The electrons in the excited dye are thought to tunnel through A-T base pairs, while single G-C pairs are believed to act as charge acceptor sites. For electron transfer across two A-T base pairs from a stilbene donor to a G-C acceptor, values of  $I = 1.03 \text{ eV}$ ,  $\Delta G^0 = -0.20 \text{ eV}$ , and  $k_{\text{DBA}} = 8.3 \times 10^9 \text{ s}^{-1}$  have been

reported.<sup>34</sup> From these values, eq (5.13) predicts a value of  $H_{DBA}^2 = 3 \times 10^{-4} \text{ eV}^2 \text{ state}^{-1}$ . For this same bridge of two A-T base pairs, eq 5.46 predicts a resistance of  $R_{MBM} = 3 \times 10^7 \Omega$  across two Au leads or between a Au substrate and a Au STM tip. Resistance measurements have not been reported, to our knowledge, on DNA chains of this length.

For electron transfer between a 7-deazaguanine modified base and an intercalated ethidium, electron-transfer times of 5 ps, 75 ps and  $\sim 2$  ns have been reported through a series of oligonucleotides of differing lengths.<sup>35</sup> As the electron transfer occurred over 5, 6, or 7 base pairs (i.e., distances of  $\sim 10$ - $17 \text{ \AA}$ ), the observed transfer times were unchanged. These data were interpreted to indicate a variation in the relative fractions of electron transfer that proceeded with each transfer time. In the model used, none of the observed quenching rates were taken to be limited by electronic coupling through the bridge. These reported transfer times can thus be used to calculate a lower bound on the electronic coupling, and therefore a corresponding upper bound on the expected resistance, for conduction between a Au electrode and a Au AFM tip that would proceed through the same assumed mechanism, through the same 7 base-pair oligonucleotide sequence of DNA. Using the 5 ps value ( $k_{DBA} = 2 \times 10^{11} \text{ s}^{-1}$ ),  $\Delta G^0 = -0.3 \text{ eV}$ , and the authors' estimated value of  $\lambda = 0.1 - 0.2 \text{ eV}$ , eq (5.13) yields  $H_{DBA}^2 = 2 \times 10^{-4} - 9 \times 10^{-6} \text{ eV}^2 \text{ state}^{-1}$ . Use of eq (5.44) then yields a corresponding electrode-bridge-tip resistance of  $R_{MBT} = 5 \times 10^7 - 1 \times 10^9 \Omega$ . Electron-transfer rates have also been reported for Ru-based redox couples bound to the termini of 8 base pairs of DNA,<sup>31</sup> with  $k_{DBA} \approx 2.5 \times 10^6 \text{ s}^{-1}$ . Use of  $\Delta G^0 = -0.7 \text{ eV}$  and  $\lambda = 0.9 \text{ eV}$  in eq (5.13) yields  $H_{DBA}^2 = 2 \times 10^{-10} \text{ eV}^2 \text{ state}^{-1}$ , and eq (5.44) yields a corresponding electrode-bridge-tip resistance of  $R_{MBT} = 4 \times 10^{13} \Omega$ .

There is a wide variation in the reported conductance of DNA,<sup>36-38</sup> with measured values depending strongly on the experimental conditions. The most meaningful comparisons to the rates predicted above should come from experiments performed under similar conditions. For repeated measurements in an aqueous buffer solution from a STM tip to a 7 base-pair poly-GC sequence coupled by a thiol linker to a Au electrode, Tao and coworkers measured single-molecule resistances of  $R_{\text{MBT}} \sim 3 \times 10^7 \Omega$ .<sup>39</sup> This resistance, which fell off inversely with distance as the chain length was reduced to 6, 5 or 4 base pairs, is well below the maximum resistance expected for such a linker as predicted using the 5 ps transfer time reported for intercalated ethidium systems, if all of the population were to undergo electron transfer at the rate presumed from the interpretation of the excited-state decay data.<sup>35</sup> The 75 ps and 2 ns decay times yield even larger maximum resistances. Experiments by other groups have however yielded higher resistances for longer DNA chains.<sup>40</sup> Because of the lack of kinetics data on excited-state tunneling-based electron transfer through these longer chains, these higher resistances cannot be directly compared using our formulation to reports of extremely long distance ( $\sim 200 \text{ \AA}$ ) oxidative damage through DNA.<sup>41</sup> The rate constant and resistance relationships embodied in eq (5.46), however, provide a simple method for performing such comparisons and for assessing the self-consistency between conductance measurements and electron-transfer rate constant measurements through bridges of interest.

### 5.3.3 Tunneling Through Conjugated Molecular Wires

Various conjugated organic molecules have been proposed as components for facilitating electron transfer in nanoscale devices.<sup>1</sup> Resistance measurements have been

made on some of these conjugated organic bridges,<sup>42-44</sup> including bridges that can act under certain conditions as antennas for rapid electron transfer.<sup>45</sup> However, without rate measurements for these molecules as donor-acceptor or electrode-acceptor bridges, our formulation cannot be used to calculate an expected electronic resistance.

Smalley et al. have measured rates of electron transfer on Au electrodes bridged by oligophenyleneethylenes to ferrocene-based redox couples.<sup>19</sup> Based on their reported values of  $\lambda = 1.06$  eV and  $k_{MBA}^0 = 6.4 \times 10^4$  s<sup>-1</sup>, a value of  $H_{MBA}^2 = 6 \times 10^{-6}$  eV<sup>2</sup> state<sup>-1</sup> is obtained from eq (5.30) for a phenyleneethylene bridge having 3 repeat units (3-OPE). Use of this coupling per state value in eq (5.38) yields a calculated resistance of  $R_{MBM} = 2 \times 10^9$   $\Omega$  for tunneling through this molecule between two Au electrodes. Similarly, the values of  $\lambda = 1.09$  eV and  $k_{MBA}^0 = 3.3 \times 10^6$  s<sup>-1</sup> reported for a 2-OPE bridge lead to predicted coupling value of  $H_{MBA}^2 = 4 \times 10^{-4}$  eV<sup>2</sup> state<sup>-1</sup> and a corresponding resistance of  $R_{MBM} = 2 \times 10^7$   $\Omega$ . Blum et al. have measured a tunneling resistance of  $R_{MBT} = 1.7 \times 10^9$   $\Omega$  between a STM tip and a Au nanoparticle that was covalently linked to a Au substrate by a S-2-OPE-phenyl-S- bridge (i.e. a bridge one phenyl group longer than 2-OPE and one ethynyl group shorter than 3-OPE).<sup>46</sup> Although the measurement convoluted the resistance of the gap between the tip and the Au nanoparticle with the resistance across the molecular bridge between the Au nanoparticle and the Au electrode, the observed resistance can be taken as an upper limit on the molecular resistance for the 3-OPE bridge coupled between the Au nanoparticle and the Au electrode. The measured resistance falls near the upper limit of the range predicted for the 2-OPE and 3-OPE bridges using eq (5.38).

## 5.4 Conclusions

Relationships between electron-transfer rates in donor-bridge-acceptor and electrode-bridge-acceptor systems, and molecular resistances in metal-bridge-metal and STM or AFM tip-bridge-metal systems have been calculated using the Fermi Golden Rule nonadiabatic treatment of electron tunneling processes. These relationships have been used to predict zero-bias resistances for alkanethiolate, DNA, and conjugated oligophenyleneethylene bridge systems, using measurements on electron-transfer rates through these molecules. For alkanethiolate bridges, the calculated resistances fall within the range of measured resistances. Resistances are also lower than predicted for oligophenyleneethylene bridges, indicating that such species couple more strongly to Au than to bound redox couples. The formalism and analytical equations presented herein provide a simple method for experimentalists to assess consistency between the various rate constant and resistance measurements through molecular bridges in a variety of electron-transfer situations.

## 5.5 Acknowledgements

Support for this work was provided by the Department of Energy, Office of Basic Energy Sciences, and the Beckman Institute.

**References:**

- (1) Adams, D. M.; Brus, L.; Chidsey, C. E. D.; Creager, S.; Creutz, C.; Kagan, C. R.; Kamat, P. V.; Lieberman, M.; Lindsay, S.; Marcus, R. A.; Metzger, R. M.; Michel-Beyerle, M. E.; Miller, J. R.; Newton, M. D.; Rolison, D. R.; Sankey, O.; Schanze, K. S.; Yardley, J.; Zhu, X. Y. *Journal of Physical Chemistry B* **2003**, *107*, 6668.
- (2) Weiss, E. A.; Wasielewski, M. R.; Ratner, M. A. Molecules as wires: Molecule-assisted movement of charge and energy. In *Molecular Wires: From Design to Properties*, 2005; Vol. 257; pp 103.
- (3) Kornyshev, A. A.; Kuznetsov, A. M. *Chemphyschem* **2006**, *7*, 1036.
- (4) Kornyshev, A. A.; Kuznetsov, A. M. *Chemical Physics* **2006**, *324*, 276.
- (5) Kornyshev, A. A.; Kuznetsov, A. M.; Ulstrup, J. *Proceedings of the National Academy of Sciences of the United States of America* **2006**, *103*, 6799.
- (6) Nitzan, A. *Annual Review of Physical Chemistry* **2001**, *52*, 681.
- (7) Nitzan, A. *Journal of Physical Chemistry A* **2001**, *105*, 2677.
- (8) Marcus, R. A. *Annual Review of Physical Chemistry* **1964**, *15*, 155.
- (9) Marcus, R. A. *Journal of Chemical Physics* **1965**, *43*, 679.
- (10) Landauer, R. *IBM Journal of Research and Development* **1957**, *1*, 223.
- (11) Marcus, R. A.; Sutin, N. *Biochimica Biophysica Acta* **1985**, *811*, 265.
- (12) Newton, M. D. *Chemical Reviews* **1991**, *91*, 767.
- (13) Ulstrup, J.; Jortner, J. *Journal of Chemical Physics* **1975**, *63*, 4358.
- (14) Kestner, N. R.; Logan, J.; Jortner, J. *Journal of Physical Chemistry* **1974**, *78*, 2148.
- (15) Brunshwig, B.; Sutin, N. *Comments in Inorganic Chemistry* **1987**, *6*, 209.

- (16) Chidsey, C. E. D. *Science* **1991**, *251*, 919.
- (17) Levich, V. G. In *Advances in Electrochemistry and Electrochemical Engineering*; Delahay, P., Tobias, C. W., ed.; Interscience: New York, 1966; vol. 4.
- (18) Royea, W. J.; Fajardo, A. M.; Lewis, N. S. *Journal of Physical Chemistry B* **1997**, *101*, 11152.
- (19) Smalley, J. F.; Sachs, S. B.; Chidsey, C. E. D.; Dudek, S. P.; Sikes, H. D.; Creager, S. E.; Yu, C. J.; Feldberg, S. W.; Newton, M. D. *Journal of the American Chemical Society* **2004**, *126*, 14620.
- (20) Kittel, C. *Introduction to Solid State Physics*, 6th ed.; Wiley: New York, 1986.
- (21) Gosavi, S.; Marcus, R. A. *Journal of Physical Chemistry B* **2000**, *104*, 2067.
- (22) The derivative of  $J_T$  with respect to  $V$  is independent of  $V$  and is given by  

$$\partial J_T / \partial V|_{V \rightarrow 0} = (4\pi^2 q^2 / 2h) \{H_{\text{MBM}}^b\}^2 \rho_{\text{mL,eff}} \rho_{\text{mR,eff}}$$
- (23) Smalley, J. F.; Feldberg, S. W.; Chidsey, C. E. D.; Linford, M. R.; Newton, M. D.; Liu, Y. P. *Journal of Physical Chemistry* **1995**, *99*, 13141.
- (24) Smalley, J. F.; Finklea, H. O.; Chidsey, C. E. D.; Linford, M. R.; Creager, S. E.; Ferraris, J. P.; Chalfant, K.; Zawodzinsk, T.; Feldberg, S. W.; Newton, M. D. *Journal of the American Chemical Society* **2003**, *125*, 2004.
- (25) Poirier, G. E.; Tarlov, M. J. *Langmuir* **1994**, *10*, 2853.
- (26) Wold, D. J.; Frisbie, C. D. *Journal of the American Chemical Society* **2001**, *123*, 5549.

- (27) Di Ventra, M.; Pantelides, S. T.; Lang, N. D. *Physical Review Letters* **2000**, *84*, 979.
- (28) Xu, B. Q.; Tao, N. J. *Science* **2003**, *301*, 1221.
- (29) Cui, X. D.; Primak, A.; Zarate, X.; Tomfohr, J.; Sankey, O. F.; Moore, A. L.; Moore, T. A.; Gust, D.; Harris, G.; Lindsay, S. M. *Science* **2001**, *294*, 571.
- (30) He, J.; Sankey, O.; Lee, M.; Tao, N. J.; Li, X. L.; Lindsay, S. *Faraday Discussions* **2006**, *131*, 145.
- (31) Meade, T. J.; Kayyem, J. F. *Angewandte Chemie—International Edition in English* **1995**, *34*, 352.
- (32) Arkin, M. R.; Stemp, E. D. A.; Holmlin, R. E.; Barton, J. K.; Hormann, A.; Olson, E. J. C.; Barbara, P. F. *Science* **1996**, *273*, 475.
- (33) Lewis, F. D.; Wu, T. F.; Liu, X. Y.; Letsinger, R. L.; Greenfield, S. R.; Miller, S. E.; Wasielewski, M. R. *Journal of the American Chemical Society* **2000**, *122*, 2889.
- (34) Lewis, F. D.; Kalgutkar, R. S.; Wu, Y. S.; Liu, X. Y.; Liu, J. Q.; Hayes, R. T.; Miller, S. E.; Wasielewski, M. R. *Journal of the American Chemical Society* **2000**, *122*, 12346.
- (35) Wan, C. Z.; Fiebig, T.; Kelley, S. O.; Treadway, C. R.; Barton, J. K.; Zewail, A. H. *Proceedings of the National Academy of Sciences of the United States of America* **1999**, *96*, 6014.
- (36) Porath, D.; Bezryadin, A.; de Vries, S.; Dekker, C. *Nature* **2000**, *403*, 635.
- (37) Kasumov, A. Y.; Kociak, M.; Gueron, S.; Reulet, B.; Volkov, V. T.; Klinov, D. V.; Bouchiat, H. *Science* **2001**, *291*, 280.

- (38) Fink, H. W.; Schonenberger, C. *Nature* **1999**, 398, 407.
- (39) Xu, B. Q.; Zhang, P. M.; Li, X. L.; Tao, N. J. *Nano Letters* **2004**, 4, 1105.
- (40) van Zalinge, H.; Schiffrin, D. J.; Bates, A. D.; Haiss, W.; Ulstrup, J.; Nichols, R. J. *Chemphyschem* **2006**, 7, 94.
- (41) Nunez, M. E.; Hall, D. B.; Barton, J. K. *Chemistry & Biology* **1999**, 6, 85.
- (42) Reed, M. A.; Zhou, C.; Muller, C. J.; Burgin, T. P.; Tour, J. M. *Science* **1997**, 278, 252.
- (43) Leatherman, G.; Durantini, E. N.; Gust, D.; Moore, T. A.; Moore, A. L.; Stone, S.; Zhou, Z.; Rez, P.; Liu, Y. Z.; Lindsay, S. M. *Journal of Physical Chemistry B* **1999**, 103, 4006.
- (44) He, J.; Chen, F.; Li, J.; Sankey, O. F.; Terazono, Y.; Herrero, C.; Gust, D.; Moore, T. A.; Moore, A. L.; Lindsay, S. M. *Journal of the American Chemical Society* **2005**, 127, 1384.
- (45) Gould, S. L.; Kodis, G.; Liddell, P. A.; Palacios, R. E.; Brune, A.; Gust, D.; Moore, T. A.; Moore, A. L. *Tetrahedron* **2006**, 62, 2074.
- (46) Blum, A. S.; Yang, J. C.; Shashidhar, R.; Ratna, B. *Applied Physics Letters* **2003**, 82, 3322.